Université de Montréal

Photophysical Investigations of

Thiophene Azomethine Derivatives

Par

Alex N. Bourque

Départment de Chimie
Faculté des arts et sciences

Mémoire présenté à la Faculté des études supérieures
en vue de l'obtention du grade de Magister Scientiæ (M. Sc.)
en chimie

August 2009

Université de Montréal
Faculté des études supérieures et postdoctorales

Ce mémoire intitulé :

Photophysical Investigations of Thiophene Azomethine Derivatives

présenté par :

Alex N. Bourque

A été évalué par un jury composé des personnes suivantes :

Prof. Garry Hanan, président-rapporteur
Prof. Will Skene, directeur de recherche
Prof. Antonella Badia, membre du jury

Abstract

A series of sterically hindered thiophene-aniline azomethine dyads were prepared. The decay pathways that deactivate the singlet excited state were studied using UV-vis fluorescence and phosphorescence, laser flash photolysis and quantum calculations. Stern-Volmer relationships, derived from singlet and triplet state quenching experiments, showed that azomethines efficiently deactivate the singlet and triplet excited states of fluorophores with bimolecular kinetics. AM1 Semi-empirical quantum calculations examining the effect of bulky substituents on the bond rotational barriers demonstrate that bulky *tert*-butyl groups attached to the aniline moiety have less influence on the N-aryl bond rotation barrier than alkyl substitutions do on the thiophene-CH bond rotation barrier. Rehm-Weller calculations based on electrochemical potentials demonstrate that azomethines self-quench their excited states via fast and efficient intramolecular photoinduced electron transfer leading to complete fluorescence suppression.

Metal complexes containing an azomethine ligand were also prepared. The ligand contains a hydroxyquinoline moiety linked with a thiophene ring. Photophysical investigations of the resulting metal complexes demonstrated significant bathochromic shifts in the absorbance and fluorescence spectra. Metal-ion sensing devices for water solutions were prepared by spin casting the ligand onto glass slides. The metal-ion sensor detected copper in water solutions through a bathochromic shift in the absorbance maximum.

Key words: photophysical properties, azomethine, thiophene, Stern-Volmer quenching, Rehm-Weller equation, steric hindrance, bond rotation, metal complexes, metal sensor.

Résumé

Une série de dimères composés de thiophène-aniline encombrée stériquement a été synthétisée. Les différents processus de désactivation de l'état singulet excité ont été étudiés par UV-visible, fluorescence, phosphorescence, photolyse par impulsion laser et calculs théoriques. Les graphiques de Stern-Volmer obtenus à partir des expériences de désactivation des états singulet et triplet ont démontré l'efficacité de l'azométhine à désactiver les fluorophores. Les calculs semi-empiriques AM1 examinant l'effet des substituants encombrés ont démontrés que les groupements *tert*-butyls sur l'aniline ont moins d'influence sur la barrière de rotation N-aryl que les substitutions alkyles en ont sur la rotation de thiophène-C. Les calculs Rehm-Weller basés sur les potentiels d'oxydation et de réduction ont montré que l'autodésactivation de l'état excité des azométhines se fait par transfert d'électron photoinduit menant à une éradication complète de la fluorescence.

Des complexes métalliques contenant des ligands azométhines ont aussi été préparés. Le ligand est composé d'une unité hydroxyquinoline lié à un cycle thiophène. Les données photophysiques de ces complexes indiquent un déplacement bathochromique aussi bien en absorbance qu'en fluorescence. Des dispositifs de détection d'ion métallique ont été préparés et un exemple à partir d'une solution de cuivre a montré un déplacement bathochromique.

Mots-clés: propriétés photophysiques, azométhine, thiophène, Stern-Volmer, équation Rehm-Weller, encombrement stérique, rotation, complexes métalliques, capteurs métalliques.

Table of Contents

Abstract ..... **iii**

Résumé ..... **iv**

List of Tables ..... **vii**

List of Figures viii

List of Acronyms and Abbreviations ..... **x**

General Introduction 1

Photophysics **3**

Decay Pathways **5**
1. Radiative Decay 5
2. Non-Radiative Decay 8
3. Triplet Manifold 9
4. Photoisomerization: 16
5. Photoinduced Electron Transfer 16

Chapter 1: Thiophene-Phenyl Azomethines with Varying Rotational Barriers – Model Compounds for Examining Imine Fluorescence Deactivation 234

1.1 Introduction **27**

1.2 Experimental Section **30**
1.2.1 General Procedures 30
1.2.2 Spectroscopic Measurements 30
1.2.3 Electrochemical Measurements 31
1.2.4 Bond Rotation Calculations... 32
1.2.5 Synthesis 31

1.3 Results & Discussion **36**
1.3.1 Synthesis 36
1.3.2 Crystallographic Study 37
1.3.3 Bond Rotation Barriers 40
1.3.4 Spectroscopic Studies 43
1.3.5 Singlet Manifold 45
1.3.6 Triplet manifold 51

1.4 Conclusions **54**

1.5 Acknowledgements **55**

Chapter 2: Synthesis and Characterization of Thiophene Azomethine Metal Complexes…..…..……..…..…..……..…….……..56

2.1 Introduction 57
2.1.1 Azomethine Ligands and Polythiophenes 59
2.1.2 Hydroxyquinoline Ligands 60

2.2 Experimental Section 62
2.2.1 General Procedures 62
2.2.2 Spectroscopic Measurements 63
2.2.3 Electrochemical Measurements 63
2.2.4 Ligand Synthesis 63
Synthesis of Ligands L_4 and L_5 67
2.2.5 Metal Complex Synthesis 69
Synthesis of complexes based on the ligands L_{1-3} 69
General procedure for metal complexation reactions with ligand L_4 69

2.3 Results and Discussions 72
2.3.1 Metal Complex Synthesis 72
2.3.2 Structural Characterization 73
2.3.3 Spectroscopic Properties 79
2.3.4 Metal Ion Sensing Devices 84

2.4 Conclusions and Future Work 85

Chapter 3: Unsuccessful Syntheses 88

3.1 Background 89

3.2 Synthetic Approaches 91

3.3 Experimental Section 99
3.3.1 General Procedures 99
3.3.2 Synthetic Protocols 99

3.4 Conclusions and Future Work 105

General Conclusions 106

References 109

Appendix A: Chapter 1 Supporting Information I

Appendix B: Chapter 2 Supporting Information XXII

Appendix C: Chapter 3 Supporting Information XXXII

List of Tables

Table 1-1. Details of crystal structure determination for **3**. 39
Table 1-2. Rotational barriers for various azomethine dyads semi-empirically calculated using AM1 starting from the X-ray crystal structure data. 42
Table 1-3. Spectroscopic data for compounds **1-9**, **10**, **11** and **14**. Values listed were recorded in acetonitrile solutions. Phosphorescence measurements were recorded in methylcyclohexane. 44
Table 1- 4. Oxidation and reduction potentials for **1-9**, **13**, and the model compound bithiophene from cyclic voltammetry measurements in anhydrous and deaerated acetonitrile and calculated energetic of electron transfer. 49

Table 2-1. A summary of the photophysical data for ligand $\mathbf{L_4}$ and its corresponding metal complexes. Data listed here were recorded in dimethylformamide solutions. 84

List of Figures

Figure I-1. Excited state decay routes available to a molecule in solution. 4
Figure I-2. A simplified Jablonski diagram. 6
Figure I-3. A Jablonski diagram demonstrating intersystem crossing to the triplet state.. 9
Figure I-4. A Jablonski diagram demonstrating the promotion of a triplet state electron by UV-vis excitation during an LFP experiment. 12
Figure I-5. A schematic of the equation-based approach for defining the quantum yield of ISC for an unknown sample. 15
Figure I-6. An example of intramolecular photoinduced electron transfer. 17
Figure I-7. Quenching of an excited state donor, D*, by an acceptor [Q]. 19

Figure 1-1. Azomethines prepared and investigated in addition to analogues. 36
Figure 1-2. Crystallographic structure of **3** as shown along the a axis (top) and b axis (bottom). 40
Figure 1-3. A representative rotational barrier energy diagram for 3 semi-empirically calculated for =N–aryl (●) and =CH–thiophene (■) bond rotation. 41
Figure 1-4. Normalized absorbance (■), fluorescence (●), and phosphorescence (▼) spectra of 3 in methylcyclohexane. Inset: Fluorescence spectrum of **3** at room temperature magnified ten times (■) and at 77 K (●)measured in a 4:1 ethanol:methanol matrix. 44
Figure 1-5. Fluorescence quenching of bithiophene in acetonitrile as a function of [**13**]: (0 mM (■) through 3.3 mM (●), 6.6 mM (▲), 12.8 mM (□) and 18.6 mM (○)). Inset: Stern-Volmer relationship of describing bithiophene fluorescence changing with [**13**]. . 47
Figure 1-6. Cyclic voltammogram of **3** measured in acetonitrile. Inset: Cyclic voltammogram of bithiophene, anodic (■)scans and **13** cathodic (●) scans as measured in acetonitrile at sweeprate of 100 mV/sec. 49
Figure 1-7. Normazlied absorbance (■) and fluorescence (●) spectra of bithiophene measured in anhydrous and deaerated acetonitrile 50
Figure 1-8. Change in the first order rate constant of triplet decay of bithiophene as a function of [13] in anhydrous and deaerated acetonitrile. Inset: Triplet decay of bithiophene as a function of [**13**] (0 mM (■) through 0.8 mM (●), 2.2 mM (▲), 4.0 mM (□) and 7.7 mM (○)) in deaerated and anhydrous acetonitrile excited at 266 nm and monitored at 380 nm. 53

Figure 2-1. Structure and bidentate chelation site of 8-hydroxyquinoline (8-HQ). 61
Figure 2-2. An example of the possible chelation modes of ligand $\mathbf{L_4}$ (left). An example of a coordination polymer, a supramolecular structure formed by metal coordination with a multi-dentate ligand (right). 62
Figure 2-3. The general synthetic route for the preparation of ligands (shown at bottom) 64
Figure 2-4. ^{1}H NMR spectrum of the metal complex of $Pb(L_4)_2$ in deuterated dimethylsulfoxide. 74
Figure 2-5. ^{1}H NMR spectrum of the ligand $\mathbf{L_4}$ in deuterated dimethylsulfoxide. 74
Figure 2-6. ESI mass spectrum of the lead complex of $\mathbf{L_4}$ recorded from DMSO solution. 77

Figure 2-7. ESI mass spectrum of the copper complex of **L_4** recorded from DMSO solution..... 78
Figure 2-8. Solvatochromism of ligand **L_4**. Measurements were made in dichloromethane (■), ethanol (●), acetonitrile (▲) and dimethylformamide (▼)..... 79
Figure 2-9. A comparison of the absorption spectra of the free ligand **L_4** (■) and its corresponding copper (●), iron (▲), manganese (▼) and lead (◀) complexes..... 81
Figure 2-10. A comparison of the fluorescence spectra of the free ligand **L_4** (■) and its corresponding copper (●), iron (▲), manganese (▼) and lead (◀) complexes..... 82
Figure 2-11. The crossover of the normalized absorbance and fluorescence scans of the free ligand **L_4** (■ and ●) and its corresponding lead complex (▲and ▼)..... 83
Figure 2-12. Changes in absorbance spectra of ligand **L_4** immobilized on a glass slide before (■) and after (●) treatment with a copper (II) solution. The other curve (▲) demonstrates the absorption of the copper complex in DMF solution..... 85

Figure 3-1. Synthesis of brominating agents **B1** and **B2** and synthesis of bromopinacolone **3-1**..... 91
Figure 3-2. Synthesis of brominating agent **B3** and synthesis of bromopinacolone **3-1**. 92
Figure 3-3. Synthesis of diketosulfide **3-2** and subsequent ring-closing reaction to form 3,4-di-*tert*-butylthiophene 3-3..... 93
Figure 3-4. Synthesis of 3,4-di-*tert*-butylthiophene **3-3** using the Grignard reagent tert-butyl magnesium chloride..... 94
Figure 3-5. Synthesis of 2,5-thiophene-(di-*tert*-butyl)-ketone 3-4. 95
Figure 3-6. Synthesis of thiophene-2,5-dicarboxylic acid methyl ester , **3-5**, 1-[5-(1-Hydroxy-heptyl)-thiophen-2-yl]-heptan-1-ol, **3-5a**, by non-oxidative Grignard reaction and subsequent oxidation to 2,5-thiophene-di(hexylketone) **3-6**..... 97
Figure 3-7. Synthesis of 2,5-thiophene-di(hexylketone) **3-6** from thiophene-2,5-dicarboxylic acid methyl ester **3-5** by oxidative Grignard reaction in the prescence of CuCN. 98

List of Acronyms and Abbreviations

5A8HQ: 5-amino-8-hydroxyquinoline
8HQ: 8-hydroxyquinoline
A: area under the curve
Abs: absorbance
AcOEt: ethyl acetate
AlQ_3 : tris(8-hydroxyquinoline) aluminum
AM1: Austin model 1; semi-empirical quantum calculations
br: broad
Cat: catalytic
cif: crystallographic information file
IC: internal conversion
ISC: intersystem crossing
d: doublet
DABCO: 1,4-diazabicyclo[2.2.2]octane
DAT: 2,5-diamino-thiophene-3,4-dicarboxyl diethyl ester
DCM: dichloromethane
DMF: N,N-dimethylformamide
DMSO: dimethylsulfoxide

δ: chemical shift

Δ: denotes a change in the value
$\Delta E_{0,0}$: intersection of normalized absorbance and fluorescence spectra, also, ground state-singlet excited state energy gap
$\Delta G°_{ET}$: Gibbs' free energy of electron transfer
ΔH_f: heat of formation

ε: molar absorption coefficient

η: refractive index
E_g^{echem}: electrochemically determined band-gap
$E_g^{spectro}$: spectroscopically determined band-gap
E_{pa}: anodic (oxidation) potential
E_{pc}: cathodic (reduction) potential
eq.: equivalent
ESI-MS: electrospray ionization – mass spectrometry
EtOH : ethanol
Fluo and fl: fluorescence
HOMO: highest occupied molecular orbital
IPA: isopropanol
J: NMR coupling constant
k_q: rate constant of quenching
k_τ rate constant of triplet state decay

λ: wavelength

LED: light-emitting diode
LFP: laser flash photolysis

LUMO: lowest unoccupied molecular orbital
m: multiplet
m/z: mass/charge
M.p.: melting point
Me: methyl
MeOH: methanol
MS: mass spectrometry
Nd-YAG: neodymium yttrium aluminum garnet laser
NLO: non-linear optical devices
NMR: nuclear magnetic resonance
OFET: organic field effect transistor/transducer
OLED: organic light emitting diode
Φ: quantum yield
PEDOT: poly(3,4-ethylenedioxythiophene)
PET: photoinduced electron transfer
Phos: phosphorescence
PI: photoisomerization
ppm: parts per million
λ_{RO}: solvent reorganization energy
RT: room temperature
s: singlet
sh: shoulder
t: triplet
τ: lifetime
TBA PF_6: tetrabutylammonium hexafluorophosphate
TEMPO: 2,2,6,6-Tetramethylpiperidine-1-oxyl
TFA: trifluoroacetic acid
THF: tetrahydrofuran
$TiCl_4$: titanium (IV) chloride
TLC: thin layer chromatography
UV-vis: Ultraviolet-visible spectroscopy

General Introduction

The work carried out in this research project was aimed at the investigation of the photophysics of conjugated thiophene azomethines by studying structure-property relationships. Thiophene azomethines are a class of conjugated thiophenes which draw structural similarities with their carbon containing analogues. The main similarity is that the azomethine linkage (C=N) is isoelectronic with the alkene (C=C) linkage.[1] As a result of this fact, thiophene azomethines demonstrate photophysical and electrochemical properties that are very similar to their carbon-containing counterparts.

Conjugated materials, and more importantly conjugated thiophenes, have found applications throughout the industrial sector in electronic devices including organic field effect transistors (OFETs), organic light emitting diodes (OLEDs) and other photovoltaic devices.[2,3,4] This is a result of their low oxidation potentials and their resistance to reductive decomposition. In addition to this, polymerized thiophenes have excellent charge carrying properties and can be used as p-type materials for charge transport layers.

The properties of such high-performance materials must be tuneable for a specific application. This can be done with conjugated thiophenes by carrying out suitable substitutions. Substitutions include the addition of electronic groups directly onto the thiophene rings, homopolymerization of varying degrees as well as copolymerization with other heterocycles. These variations can significantly change the resulting physical properties of the conjugated materials.

The largest issue that confronts the use of conjugated thiophenes in electronic applications is their synthesis and subsequent purifications. The most common method of producing homo- and heteropolymerized oligo- and polythiophenes is through

electrochemical polymerizations. Conjugated thiophenes can also be prepared chemically with common coupling methods that include the Suzuki, Negishi, and Kumada coupling protocols, as well as coupling by chemical oxidation.[5,6,7,8] However, these coupling methods are prone to producing side-products that can negatively affect the performance of the materials in a device.

Azomethines are therefore an interesting class of compounds to study since their preparation produces only water as a side-product, and purification of the desired product is very straightforward. This, combined with their similarities to widely used polythiophene and arylvinylene compounds, makes thiophene azomethines a suitable choice for new materials. In addition to this, azomethines can be more robust to chemical and electrochemical degradation than their carbon analogues depending on the substitutions used in their preparation.

The major difference between vinylene and azomethine analogues can be found in their photophysical properties. Conjugated arylvinylenes are often fluorescent[9,10,11] while conjugated azomethines demonstrate no fluorescence. Fluorescence in thiophene azomethines has been shown to be nonexistent regardless of the number of thiophene units or azomethine bonds present in the molecule. This is in contrast to oligothiophenes[12,13,14] which demonstrate an increase in fluorescence with increasing number of thiophene rings.

The absence of fluorescence as a result of the azomethine bond will be discussed in this work. Multiple methods of examining the change in photophysics as a function of azomethine structure were employed in an effort to increase the amount of fluorescence observed in thiophene azomethines. The methods employed were designed to deactivate

one of the excited state decay routes in an effort to isolate the most important excited state deactivation pathways. Thiophene azomethine model compounds were investigated by various experimental and synthetic strategies. These include the formation of metal complexes composed of thiophene azomethine ligands and their photophysical characterization, and the synthesis of a series of sterically hindered thiophene azomethines followed by photophysical characterization through a set of excited state quenching experiments designed to study the mechanisms of excited state deactivation.

Photophysics

When an organic molecule absorbs a photon, an electron is promoted from its ground state to an excited state. The core electrons and lower energy valence electrons are not usually excited by this route. In fact, it is usually the electrons contained in the higher energy frontier molecular orbitals that have energies that correspond to the energy of visible and ultraviolet light. In this way, valence electrons situated in the HOMO are most frequently excited by an incident light source.[15] The promotion of higher energy electrons into previously unpopulated electron shells produces an electronic state which is much more reactive than the ground state. The reactive promoted electrons cannot remain indefinitely in their excited state and undergo decay processes that return them to the ground state.

The method of excited state deactivation employed by the system depends strongly on the molecules present. Figure I-1 demonstrates the variety of photochemical pathways that are available for excited state decay. The three broad categories are 1) excited state decay pathways, 2) unimolecular photochemical reactions and 3) bimolecular photochemical reactions. The decay pathways are subdivided into

nonradiative and radiative decay processes. Of interest in this work are the variety of excited state decay pathways and the uni- and bimolecular electron transfer reactions.

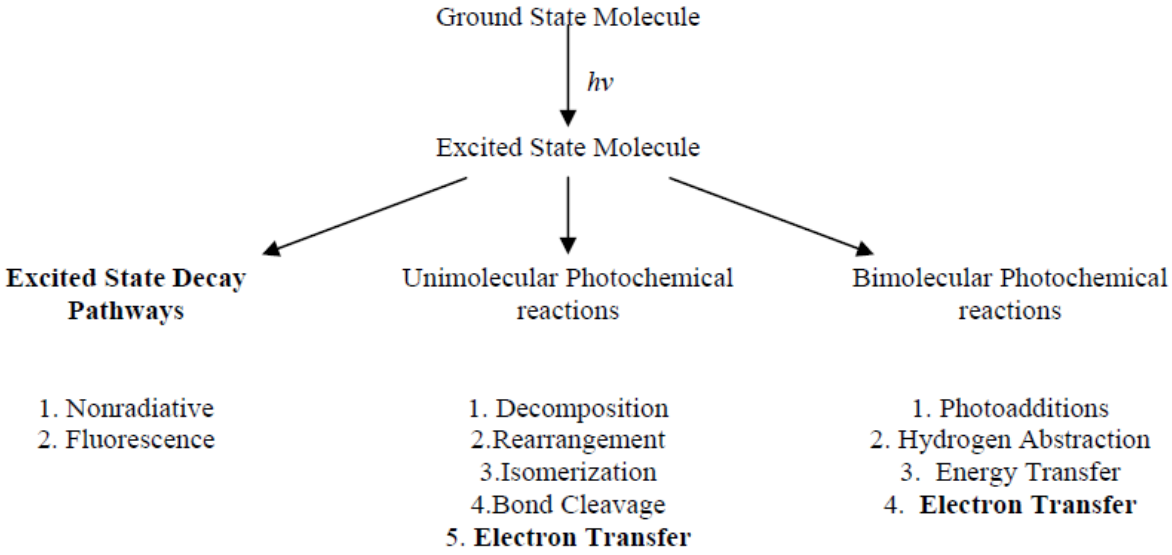

Figure I-1. Excited state decay routes available to a molecule in solution.[15]

The excited state decay pathways listed in Figure I-1 above, in addition to photoinduced electron transfers, are needed to fully characterize the equation

$$1 = \sum_{x} \Phi_{x} = \Phi_{fluo} + \Phi_{IC} + \Phi_{ISC} + \Phi_{isomerization} + \Phi_{PET} \qquad \textbf{E-1}$$

which demonstrates that the quantum yields, Φ, of all of the deactivation processes available to the singlet excited state must sum to unity. The ISC term can be broken down further to include both radiative and non-radiative decay from the triplet state, as seen in **E-6** (*vide infra*).

From left to right in equation **E-1** are the quantum yields of fluorescence, internal conversion, intersystem crossing, photoisomerization, and photoinduced electron transfer. There are various experimental techniques available to scientists for quantifying these quantum yields. The experimental techniques available and the theory behind them will be discussed in the following sections.

Decay Pathways

1. Radiative Decay

A simplified Jablonski diagram, shown below in Figure I-2, is used to describe the excited state decay pathways schematically. An electron in the S_0 ground state is excited by absorption of a photon to the first or second singlet excited state, S_1 and S_2, respectively, at which point the electron will begin to decay back to the ground state. One of the fastest and most commonly observed excited state decay pathways is the radiative decay process, fluorescence.

Fluorescence is the process by which an excited state molecule decays back to its ground state by emitting a photon of lower energy than the photon used to excite it. The fluorescence maximum is red-shifted from the absorbance maximum by an amount called the Stokes shift. The Stokes shift relates the amount of energy that is lost by non-radiative decay of the singlet excited state before fluorescence can occur. The point of intersection of the normalized absorbance and fluorescence spectra for a molecule leads to a wavelength value, λ_{AF}, which can be converted to an energy value by

$$\Delta E = \frac{hc}{\lambda} \qquad \textbf{E-2}$$

where h is Planck's constant, c is the speed of light and λ is the aforementioned λ_{AF}.[16] The value of ΔE is an approximation of the energy gap between the singlet excited state and the ground state of the molecule. It is a direct method for obtaining the relative energies of the HOMO and LUMO levels since the HOMO is normally the ground state and the LUMO is usually the lowest excited.

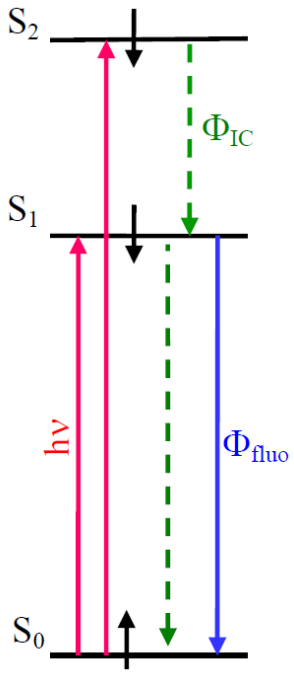

Figure I-2. A simplified Jablonski diagram.

The magnitude of the observed fluorescence can be determined experimentally by measuring the fluorescence quantum yield, Φ_{fl}. The fluorescence quantum yield is defined as the number of photons emitted by a sample divided by the number of photons absorbed by the sample

$$\Phi_{fl} = \frac{nb\ of\ \ photons\ emitted}{nb\ of\ \ photons\ absorbed}. \qquad \textbf{E-3}$$

The fluorescence quantum yield can be determined in two ways. The traditional method applies reference molecules of known fluorescence quantum yield called actinometers. The reference molecule is excited at a specific wavelength, and its fluorescence spectrum is recorded. A sample molecule is excited at the same wavelength and its spectrum is recorded as well. The crucial factor is that the absorbances of both molecules must be identical at the wavelength of excitation, within +/- 5 %. This ensures that each molecule absorbs the same number of photons, and hence produces the same

number of excited states. The ratio of the integrals of the fluorescence spectra gives the relative amount of fluorescence observed for the sample compared to the standard

$$\Phi_{fl,x} = \Phi_{fl,ref} \frac{Abs_{ref} \times A_x \times n_x^2}{Abs_x \times A_{ref} \times n_{ref}^2} \qquad \textbf{E-4}$$

where the values Φ represent the fluorescence quantum yields, *Abs* indicates the absorbance value at the wavelength of excitation, *A* indicates the area under the fluorescence curve (i.e. the integral), and η indicates the refractive index of the solvents used, if multiple solvents are needed. The terms *ref* and *x* refer to the actinometer and sample, respectively.

Historically, this method has been the most common way of measuring the fluorescence quantum yield. It does, however, suffer from a few drawbacks. To measure a quantum yield, one needs a reference molecule that absorbs near the sample molecule, emits in the same region as the sample and also has a very similar quantum yield. Changing solvents can also have solvatochromic effects and can significantly change the observed quantum yield, even if refractive index is taken into consideration.

In recent years, integrating spheres have attracted much attention for measuring fluorescence quantum yields. The integrating sphere is an addition to a fluorescence detection system that measures accurately the intensity of light entering the sphere. The sphere contains an entrance and an exit hole allowing for the movement of light. The interior of the sphere is coated with a highly reflective material ($BaSO_4$) which reflects all of the light that enters the sphere towards the fluorescence detector.

The technique is applied experimentally by taking a fluorescence measurement of a solvent blank in which the solvent is excited at the wavelength of excitation of the molecule. The fluorescence spectrum is recorded over a region +/- 10 nm from the

excitation wavelength. The term used by the equipment during measurement is “scatter”. The scatter term used here is meant to relate the size of the excitation window. If the excitation slit is set to 10 nm, then there will be “scatter” of the excitation peak +/- 5 nm from the excitation maximum. The cuvette containing only solvent is replaced by a cuvette containing the sample. The first measurement is repeated. This measurement relates the amount of light that is absorbed by the sample molecule (since the solvent alone does not absorb). Then a standard fluorescence spectrum of the sample is recorded. The integrals of the three spectra are calculated and

$$\Phi_{fl,x} = \frac{\int Sample \quad Emission}{\int Blank \quad Scatter - \int Sample \quad Scatter} \qquad \textbf{E-5}$$

is used to relate the amount of light absorbed by the sample (blank scatter – sample scatter) to the amount of light emitted by the sample (sample emission). This is a more direct, efficient and absolute method of determining the quantum yield of fluorescence. However, this method is not as sensitive as the actinometer method and can only be used when the fluorescence quantum yield exceeds 0.05. Very weak fluorescence is often too weak to be accurately detected exiting the integrating sphere.

2. Non-Radiative Decay

The excited state is also capable of decaying non-radiatively from the singlet manifold to the ground state through a variety of vibrational, bending and stretching processes that are collectively known as internal conversion processes, Φ_{IC}. When internal conversion plays a predominant role in the decay of the excited state, little to no fluorescence is observed. Molecules with a high degree of rigidity and planarity are often highly fluorescent as the bending and stretching vibrational modes are effectively

dampened by rigidity in the structure. Molecules such as fluorene and anthracene show high degrees of structural rigidity, as well as high quantum yields. One of the main goals of this work is to restrict the available stretching, bending and twisting modes in thiophene azomethines with the focus of increasing the fluorescence quantum yields.

3. Triplet Manifold

From the singlet excited state, the promoted electron can also decay non-radiatively through a process called intersystem crossing (ISC) in which the electron changes spin causing a shift in the multiplicity of the excited state from one (singlet state) to three (triplet state). This process is shown schematically in Figure I-3 with the aid of a Jablonski diagram. Once in the triplet state, the molecule can relax back to the ground state by radiative and non-radiative decay processes, as was the case in the singlet state. The radiative decay process is called phosphorescence and is observed on time scales much longer than that for fluorescence. Triplet states can also decay to the singlet ground state through internal conversions via intersystem crossing.

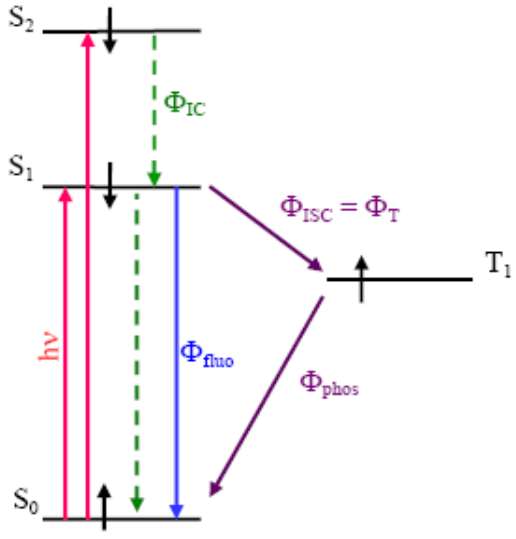

Figure I-3. A Jablonski diagram demonstrating intersystem crossing to the triplet state.

The triplet state quantum yield is a measurable quantity. It relates the amount of singlet excited states that are converted to triplet excited states after a molecule is photoexcited. The triplet state quantum yield is often denoted by the term Φ_{ISC} as intersystem crossing is the process by which the triplet state is formed from the singlet excited state. Phosphorescence measurements and laser flash photolysis measurements are often used in conjunction to quantitatively describe Φ_{ISC}. Triplet excited states can also decay back to the singlet ground state through non-radiative internal conversion processes, e.g. bond vibration and collisions with solvent molecules, so it is important to use phosphorescence and laser flash photolysis measurements together to accurately define triplet state formation.

Phosphorescence measurements can be used to characterize the formation of a triplet manifold. The long-lived triplet state is formed by a quantum mechanically forbidden spin-flipping mechanism which produces an electronic transition that is in violation of the conservation of molecular spin moment rules. As a result of this, the triplet state cannot return to a singlet excited state with ease and will decay directly back to the lower energy singlet ground state. Radiative decay, called phosphorescence, has a much longer lifetime than fluorescence owing to the fact that the system must change spin states upon returning to the ground state. Phosphorescence is often used in nature by insects and aquatic life as a form of protection and also for offering light in very dark places, like the deep ocean. The fact that the lifetimes of phosphorescence can extend into the second range give phosphorescent materials many potential applications, in ‘glow sticks’ and airplane floor lighting, for example.

The triplet manifold can also be studied by a technique called laser flash photolysis. In this technique, a molecule is excited with high intensity light produced by a laser. In this work, samples were excited at either 266 nm or 355 nm using an Nd-YAG laser. If a triplet state exists for the molecule studied, the laser excitation will pump the sample into its singlet excited state, at which point it undergoes ISC to its triplet state. The triplet state, which is longer lived than the singlet state, is referred to at this point as a transient species because it exists only briefly while being excited by the laser.

The transient species produced by laser excitation can then be excited a second time by UV-vis light, promoting the triplet level electron to a second, higher energy triplet excited state. This is demonstrated schematically in Figure I-4. Once the molecule is in the triplet state T_1, it is able to absorb light corresponding to the energy gap between the two triplet states, $T_1 \rightarrow T_2$. In practice, the LFP instrument measures the amount of light absorbed by the triplet state as it is in the process of decaying. As the state begins to decay, the absorbance values recorded by the LFP instrument will begin to decay with an exponential decay profile. The lifetime of the triplet state can thus be calculated by fitting the triplet decay to an exponential decay function.

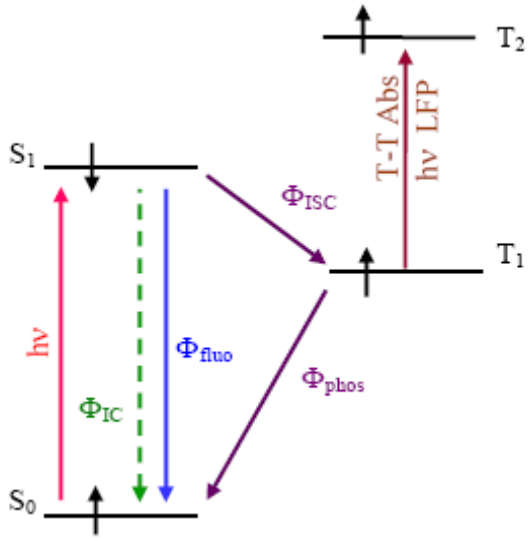

Figure I-4. A Jablonski diagram demonstrating the promotion of a triplet state electron by UV-vis excitation during an LFP experiment.

Phosphorescence studies are useful in examining the energetics of the photoinduced triplet state. The phosphorescence maximum, λ_{phos}, can be used to relate the energy of the triplet excited state from which a promoted electron decayed back to its ground state. The molecule of interest is excited at its absorbance maximum which corresponds to its LUMO energy, or in other words, the singlet excited state. The wavelength at which the phosphorescence maximum is observed is at a slightly lower energy than the triplet excited state, T_1. The crossover of the normalized absorbance and phosphorescence spectra is effectively the energy gap separating the singlet ground state and the excited triplet state. This process is also used to relate the energy difference between the singlet ground state and singlet excited state (HOMO-LUMO gap) when studying fluorescence data instead of phosphorescence data.

The phosphorescence quantum yield can be determined using the same actinometer method employed for fluorescence measurements. However, Φ_{ISC} cannot be accurately determined by this method as it is known that triplet states can decay by means

other than phosphorescence alone. The triplet excited state, much like the singlet excited state, can also undergo internal conversion process like bond vibration and rotation that decrease the amount of phosphorescence observed. In other words, the phosphorescence quantum yield does not take into account internal conversion from the triplet state and therefore

$$\Phi_{ISC} = \Phi_{Phos} + \Phi_{IC} \qquad \textbf{E-6}$$

To accurately quantify triplet state formation, Φ_{ISC}, it is important to complement phosphorescence measurements with laser flash photolysis quantum yield measurements.

The quantum yield of triplet formation, Φ_{ISC}, can be measured accurately by laser flash photolysis. Triplet state quantum yield measurements are possible by relating the amount of triplets formed by a sample molecule to those of a standard material known to have a triplet quantum yield of unity. A frequently used standard material is xanthone.[17]

Significant difficulties present themselves when attempting to carry out triplet quantum yield measurements. If the molecule of interest has a measurable ground state absorbance in the region where the triplet state absorbs, an effect called “ground state photobleaching” is observed. To observe the formation of a transient species, the absorbance of the non-excited molecule (ground state) is compared with that of the excited species at a specific wavelength. The difference between the two absorbance measurements is the value recorded by the measurement system and can indicate the presence of a triplet excited state. If the ground state absorbs more strongly than the excited state at a given wavelength, the detection system will record that the absorbance has decreased upon laser excitation and will record a negative signal. It is therefore

important to ensure that any measurements examining triplet state formation are made at a wavelength in which the ground state does not absorb.

The process of defining the triplet quantum yield can also be troublesome. The molar absorptivity, ε, and the quantum yield, Φ_{ISC}, of the triplet state of a reference must be known. The quantum yield of the unknown sample can be determined from

$$\varepsilon_{Tx} \times \Phi_{Tx} = \varepsilon_{Tref} \times \Phi_{Tref} \qquad \textbf{E-7}$$

where ε_{Tx} and ε_{Tref} are the molar absorptivity coefficients of the triplet state for the unknown and reference, respectively; and where Φ_{Tx} and Φ_{Tref} are the triplet quantum yields. The molar absorptivity of the unknown sample is determined first by applying this equation

$$\varepsilon_{Tx} = \varepsilon_{Tref} \frac{\Delta\, Abs_x}{\Delta\, Abs_{ref}}. \qquad \textbf{E-8}$$

Here the $\Delta\, Abs$ values are the change in absorbance recorded by the laser flash photolysis system before and after excitation. To employ this equation experimentally, a standard of known quantum yield and molar absorptivity is studied. The reference material used is frequently xanthone since it has a Φ_{ISC} of unity.[17] Xanthone and the molecule of interest have their ground state absorbance at the wavelength of excitation (266 or 355 nm for the instrument used) tuned to be nearly identical. Both compounds are excited and then quenched using a known amount of quencher, for example, naphthalene.

The process of measuring the quantum yield is best described through an equation-based approach as shown in Figure I-5. The xanthone standard, Xn is excited via LFP to its singlet state (Xn^1) which then undergoes ISC to its triplet state (Xn^3). The triplet state is quenched with a known concentration of quencher (naphthalene, Np). The

quencher is excited to its triplet state (Np^3) via energy transfer from the excited xanthone. The triplet of naphthalene is then analyzed using the LFP UV-vis absorbance system in the same way triplet states are normally observed, yielding the value ΔAbs_{ref} which is needed in **E-8**.

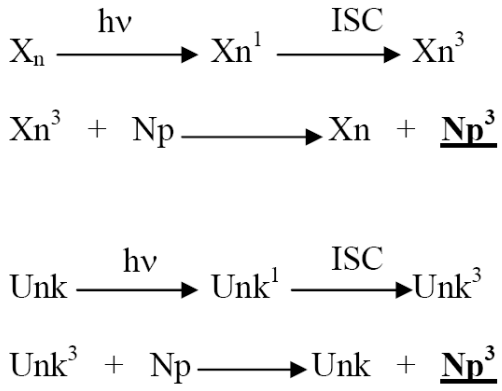

Figure I-5. A schematic of the equation-based approach for defining the quantum yield of ISC for an unknown sample.

The unknown sample molecule is treated in the same way. The ground state (Unk) is pumped to the singlet excited state (Unk^1) via laser excitation, the triplet state (Unk^3) forms via ISC and is subsequently quenched with the same concentration of quencher (Np) that was used to quench the xanthone standard. Once again, the signal produced by the triplet state quencher ΔAbs_x (Np^3) is recorded by the LFP system. The Δabs_{ref} and ΔAbs_x values are recorded for the naphthalene triplets in both cases, so the molar absorptivity terms, ε_τ, fall out of **E-8**. Combining and simplifying **E-7** and **E-8** yields the equation **E-9** which is used to experimentally determine the quantum yield of ISC for sample molecules when Φ_τ for the standard is already known.

$$\Phi_{T\,x} = \Phi_{T\,ref}\,\frac{\Delta\, Abs_x}{\Delta\, Abs_{ref}} \qquad \textbf{E-9}$$

In conjunction with phosphorescence measurements, laser flash photolysis measurements can be used to characterize both the lowest energy triplet state as well as some of its higher energy states. Lifetimes of decay for both processes can be determined which give additional information about the energies of the excited state species.

4. Photoisomerization

Photoisomerization is the process by which an excited state molecule undergoes a chemical transition to another isomeric form as a way of returning itself to its ground state. Common forms of photoisomerization include *cis-trans* isomerization and ring opening and closing transformations. Although photoisomerization can play a role in excited state decay, the thiophene azomethines prepared and studied herein do not undergo PI and therefore PI will not be treated in more detail.

5. Photoinduced Electron Transfer

Photoinduced electron transfer occurs when a molecule is excited by light, promoting a ground state electron into an excited state orbital. The promotion of this electron leaves a positively charged vacancy in the ground state, which is commonly referred to as a hole. Holes can act as electron acceptors as the positively charged vacancy makes the ground state electronic levels electrophilic. Furthermore, the promoted electron is now at a higher energy than before and can be attracted by an electron acceptor. In this way, excited states can act as both electron donors and electron acceptors. Photoinduced electron transfer can therefore be defined as the movement of the electrons through a molecular system initiated by the photo-produced excited state.

There are two types of PET mechanisms commonly observed in photochemistry. The distinction between the two is based on the location of the donor and acceptor molecules. In a one molecule, or intramolecular process, the donor and acceptor are attached covalently and the electron that is transferred moves between two regions of the same molecule. In a two molecule, or intermolecular process, the donor and acceptor exist separately on two different molecules.

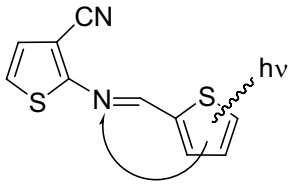

Figure I-6. An example of intramolecular photoinduced electron transfer.

An example of an intramolecular electron transfer process is seen with the molecules of interest in this report; thiophene azomethines. Shown in Figure I-6, the thiophene azomethine can be excited through the absorption of a photon by the thiophene moiety at which point the electron-accepting azomethine linkage can quench the excited state. This rapid deactivation by the azomethine linkage is a main reason why thiophene azomethines consistently show little fluorescence.[18] An example of an intermolecular electron transfer is taken from the world of biology. The processes which help to move energy around during photosynthesis are nearly all bimolecular electron transfer processes. Light absorbed in the stroma initiates a water photolysis reaction that produces molecular oxygen, protons and electrons. The electrons are carried throughout the photosynthetic cell through a series of bimolecular electron transfer mechanisms which collectively make up an "electron transport chain".[19,20]

Electron transfer processes can be studied experimentally by employing such techniques as excited state quenching experiments. The two sets of quenching experiments studied herein are fluorescence and triplet state (via LFP) quenching. In these methods, a donor molecule is excited by visible or UV irradiation which promotes an electron to an excited state. The excited state of the donor molecule is then "quenched" by the introduction of an acceptor molecule which removes the electron from the high energy orbital of the donor. For this reason, molecules which act as electron acceptors are often called "quenchers".

The excited state quenching mechanism can be studied by measuring the quenching rate constants and by examining the energetics of the quenching process. The two studies are closely related, but rely on different experimental techniques and different mathematical treatments. The study of quenching rates constants, either from fluorescence quenching or triplet state (LFP) quenching, is carried out using the Stern-Volmer relationship. The study of the energetics of the quenching process focuses on the oxidation and reduction potentials of the donor and acceptor molecules, respectively. The Rehm-Weller equation is then used to relate the electrochemical potentials with the free energy of quenching.

The reaction equations presented in Figure I-7 demonstrate the processes that occur when an excited donor molecule is being quenched by an acceptor. The excited state donor molecule encounters a quencher molecule that acts as a strong electron acceptor. Through a bimolecular electron transfer process, the excited state of the donor is transferred to the quencher.

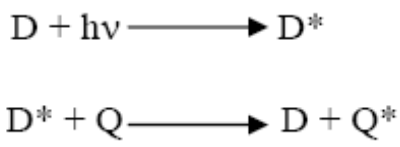

Figure I-7. Quenching of an excited state donor, D*, by an acceptor [Q].

The Stern-Volmer relationship for dynamic fluorescence quenching can be used to describe the rate at which the quencher molecule is able to deactivate the excited state of the donor, D. The rate constant of bimolecular quenching can be determined experimentally from the Stern-Volmer relationship

$$\Phi_0/\Phi = 1 + k_q \bullet \tau_0 \bullet [Q] \qquad \textbf{E-10}$$

where Φ_0 is the fluorescence intensity without quencher and Φ is the fluorescence intensity after quencher has been added, k_q is the bimolecular quenching rate constant, τ_0 is the fluorescence lifetime of the fluorophore and [Q] is the concentration of quencher added.[21] A straight line plot of this relationship will yield the dynamic quenching rate constant as the slope of the line. In cases when the rate of quenching is very fast, the quenching process is limited by the rate at which the quencher molecule can collide with the excited state donor molecule. This limiting factor is the rate of diffusion of the quencher, so k_q is often defined as the diffusion-limited rate constant of quenching (2 x 10^{10} $m^{-1}s^{-1}$ in acetonitrile, *vide infra*).

The quenching rate constant for the quenching of triplet states can also be studied experimentally. Instead of making fluorescence measurements and observing how the intensity of fluorescence decreases, it is also possible to follow the decrease in the lifetime of the photo-produced triplet state. The measurement system used in this case is the laser flash photolysis system. As before, a donor molecule is excited by light (here a

laser) and a quencher molecule in solution deactivates the excited state by electron transfer. The difference in this case is that instead of looking at the decrease in signal intensity, the decrease in the triplet state lifetime is examined. The inverse of the triplet state decay lifetime is the rate constant of triplet state decay, k_τ, which is in fact is experimental value used in the Stern-Volmer relationship. To determine the rate constant of triplet state quenching, the following equation is applied experimentally:

$$k_\tau = k_0 + k_q [Q] \qquad \textbf{E-11}$$

where k_τ is the rate constant of triplet state decay, k_0 is the triplet state decay rate constant in the absence of quencher, k_q is the rate constant of quenching and [Q] is the concentration of quencher added. Once again, the dynamic rate constant is limited by diffusion.[18]

The preceding discussion about the rates at which quenching occurs is only useful when the excited state molecule can be deactivated through a bimolecular process. It is important that quenching be exergonic, that is, energetically favourable. To this end, the Rehm-Weller equation can be used to determine theoretically whether a quencher can dynamically quench an excited donor. The Rehm-Weller equation can be described thusly,

$$\Delta G^\circ_{ET} = E_{pa}\,(\text{fluorophore}) - E_{pc}\,(\text{quencher}) - \Delta E_{0,0} - \lambda_{RO}. \qquad \textbf{E-12}$$

where ΔG°_{ET} is the Gibbs' free energy of electron transfer, E_{pa} is the oxidation potential of the fluorophore (donor), is the reduction potential of the quencher, $\Delta E_{0,0}$ is the energy gap between the ground and excited state of the fluorophore and λ_{RO} is the solvent reorganization energy.[22,23]

The oxidation and reduction potentials are easily measureable by cyclic voltammetry methods and the energy gap between the excited and ground states can be derived from the intersection of the normalized absorbance and fluorescence spectra. The solvent reorganization energy is usually quite small when the measurements are recorded in polar solvents such as acetonitrile (ACN) and is therefore often neglected.

The Stern-Volmer (**E-10**) and Rehm-Weller (**E-12**) equations are applicable to intermolecular processes. The case that makes thiophene azomethines very interesting is that not only is the donor fluorophore located within the molecule, but so is the quenching acceptor moiety. The azomethine linkage (C=N) is extremely efficient at quenching excited states, so much so that neither fluorescence nor a triplet state (via LFP at room temperature) are observable. In general, azomethines are excellent quenchers and can be used in a variety of ways to quench fluorescence within an inherently fluorescent molecule. It is for this reason that in-depth studies of the kinetics and energetics of bimolecular quenching processes using azomethines have been carried out and reported herein.

This work has been divided into three chapters each focussing on a different area of azomethine chemistry. Chapter 1 contains the manuscript of a submitted article detailing the study of the electrochemical and photophysical properties of a series of sterically hindered azomethine dyads. These dyads were studied via singlet and triplet excited-state quenching experiments yielding quenching rate constants after determining the Stern-Volmer and Rehm-Weller relations.

Chapter 2 discusses the study of azomethine-metal ion complexes via UV-visible spectroscopy and cyclic voltammetry. The work presented in Chapter 2 was aimed at

further understanding the role of the azomethine linkage in deactivation processes as well as furthering the study of the photophysical and electrochemical properties of azomethines. Chapter 3 explores different reaction conditions used to form dyads which are more sterically hindered than those discussed in Chapter 1. The reactions presented in Chapter 3 did not produce the desired products; however, they did provide insight into the difficulties that arise during the synthesis of sterically hindered compounds.

In summary, the work carried out in this research project was aimed at the investigation of the photophysics of conjugated thiophene azomethines by studying structure-property relationships. The decay pathways that deactivate the singlet excited state were studied using UV-vis fluorescence and phosphorescence, laser flash photolysis and quantum calculations. Stern-Volmer relationships, derived from singlet and triplet state quenching experiments, showed that azomethines efficiently deactivate the singlet and triplet excited states of fluorophores with bimolecular kinetics. Rehm-Weller calculations based on electrochemical potentials demonstrate that azomethines self-quench their excited states via fast and efficient intramolecular photoinduced electron transfer leading to complete fluorescence suppression.

Preface

My contributions to the article presented herein include the vast majority of the experimental work. I synthesized, purified and characterized the series of thiophene-phenyl dyads described in the work. I carried out the photophysical and electrochemical investigations of the molecules of interest. These investigations included the use of UV-vis absorbance, fluorescence and phosphorescence techniques, including measurements carried out at 77 K. I also carried out the cyclic voltammetry analysis for the electrochemical properties. I prepared samples for X-ray, mass spectrometry and elemental anaylsis, however the actual analyses were carried out by a third party (S. Dufresne carried out the X-ray crystal structure resolution).

For the preparation of the manuscript, I reviewed the literature to provide an in-depth background of what was presented in the article. I produced the figures and tables that are shown in the manuscript. I prepared drafts of the introduction and results sections which were later improved upon by Prof. Skene. The quantum calculations were also carried out by Prof. Skene. The other contributing authors, Prof. Skene and Mr. Dufresne, have agreed to allow the use of the publication as a chapter in this report.

Chapter 1: Thiophene-Phenyl Azomethines with Varying Rotational Barriers – Model Compounds for Examining Imine Fluorescence Deactivation

Article 1

Alex N. Bourque, Stéphane Dufresne, W. G. Skene

Centre for Self-Assembled Chemical Structures, Department of Chemistry

Université de Montréal, Pavillon J.A. Bombardier, C.P. 6128, succ. Centre-Ville, Montreal QC, H3C3J7, Canada

Published:

Journal of Physical Chemistry C, **2009**, 113, 19677-19685

Abstract

Alkylated derivatives of 2, 4, 6-aniline and 3-thiophene carbaldehydes were used for preparing aldol and ketal imines (**1**-**9**). The effect of substitution on the photophysical properties of alkylated azomethines was examined in order to understand the origins of complete fluorescence suppression exhibited by all azomethines. Introducing steric elements for increasing the barrier of rotation around the N–aryl and CH–thiophene bonds did not result in increased fluorescence. This confirmed that azomethine fluorescence quenching is not by non-radiative energy dissipation by bond rotation.

Stern-Volmer fluorescence measurements of both fluorene and bithiophene lead to diffusion controlled quenching rates ($k_q \approx 10^{10}$ M^{-1} s^{-1}) when quenched by both an aliphatic aldolimine (**13**) and a conjugated azomethine (**3** and **15**). Photoinduced electron transfer (PET) from the fluorophore to the imine is the major mode of deactivation of the singlet excited state. This deactivation mode was corroborated by the Rehm-Weller equation using the measured cyclic voltammetry and spectroscopic data. Exergonic values for PET were calculated for bithiophene quenching with **13** ($\Delta G°$ = -120 kJ/mol). The PET deactivation mode can be suppressed by protonating the azomethine resulting in increased fluorescence.

Although PET deactivates the singlet excited state, intersystem crossing to the triplet manifold also occurs, confirmed by steady-state phosphorescence measurements. The absence of detectable triplet by laser flash photolysis confirms that the triplet formed is rapidly quenched by energy transfer. This was kinetically corraborated by quenching both fluorene and bithiophene triplets with **13** leading to bimolecular quenching rate constants of 3 x 10^9 M^{-1} s^{-1} and 2 x 10^7 M^{-1} s^{-1}, respectively, in acetonitrile. These data

confirm that the heteroatomic azomethine bond efficiently quenches both the singlet excited and triplet states by intramolecular photoinduced electron transfer.

1.1 Introduction

Conjugated thiophenes have been the focus of much research owing to their interesting properties that are well suited for organic electronic applications including field effect transducers (OFET), light emitting diodes (OLED), photovoltaics (OVD), and nonlinear optical devices (NLO).[2,3,4] This is in part due to their low oxidation potential relative to their homoaryl analogues. Subsequently, they can be chemically doped resulting in stable p-type materials with high conductivities and charge mobilities.[24,25] Furthermore, property tuning to match a specific electronic application is possible by incorporating electronic groups along the conjugated framework in addition to copolymerizing with other heterocyclic monomers. Copolymerization and homopolymerization are typically done electrochemically. Alternatively, chemical polymerization is possible via Suzuki, Negishi, and Kumada coupling protocols.[5,6,7,8]

As requirements for materials performance increase, new materials with tunable properties requiring alternate methods for their preparation are needed. For example, nickel-catalyzed Kumada coupling was recently used for controlling polymer molecular weight and regioregularity, while Wittig coupling and thermal elimination methods, to name but a few, afford polyvinylenes with optoelectronic properties suitable for electronic applications.[26,27,28] Even though functional materials can be successfully obtained using these protocols, the by-products produced affect the optoelectronic properties of produced materials. Materials prepared via these coupling methods must therefore be extensively purified for removing residual catalysts, unreacted monomers and other by-products.

Azomethines are interesting alternatives to conventional coupling methods. This is in part a result of their isoelectronic character to their vinylene analogues.[1] Furthermore, water is the only by-product produced requiring little to no purification, unlike their carbon analogues. Similar to their carbon analogues, azomethines are thermally, chemically, and anodically robust when the appropriate aryl monomers are selected for their preparation.[29,30,31,32,33,34] Although azomethines have synthetic advantages over their carbon analogues and exhibit similar thermal and chemical properties to their vinylene homologues, their photophysical properties are different. For example, arylvinylenes[9,10,11] and oligothiophenes[12,13,14] are highly fluorescent while their azomethine analogues exhibit no fluorescence. In fact, the fluorescence of thiophene azomethine derivatives is consistently nonexistent regardless of the number of thiophenes or the number of azomethine bonds. This is in stark contrast to oligothiophenes whose fluorescence increases with the number of thiophenes.[35,36,37]

Even though it is known that azomethines do not fluoresce irrespective of their degree of conjugation or whether inherently fluorescent precursors are used in their preparation, very little effort has been devoted to understanding the reasons for this suppressed fluorescence.[38,39] Previous investigations attempted to assign the cause of azomethine suppressed fluorescence by examining a series of thiophene azomethines such as **14** and **15** and their temperature dependent fluorescence.[30,32,33,34] Qualitative evidence led to the belief that efficient nonradiative excited state deactivation was a result of rotation of the aryl groups fixed to the azomethine. Unfortunately, this deactivation mode could not unequivocally be confirmed with the azomethines investigated.

Assigning the deactivation modes responsible for efficient azomethine fluorescence suppression is possible only with structure-property studies. Specifically, the contribution of singlet excited state deactivation by rotation around the N-aryl and CH-thiophene bonds can be isolated from other deactivation modes such as internal conversion (IC) and intersystem crossing (ISC) by examining the photophysics of azomethines having inherent rotation constraints around these bonds. This is of importance because new highly fluorescent azomethines can then be designed and prepared using this information.

Such fluorescent azomethines having similar spectroscopic and electronic properties to their carbon analogues would make azomethines viable alternatives to current materials given their ease of synthesis, absence of by-products and appealing green-chemistry. A series of thiophene azomethine dyads consisting of varying steric elements was therefore prepared for investigating the origin of azomethine fluorescence deactivation. The photophysical study of these novel dyads and the structural effects of these properties are herein presented in order to fully understand the azomethine fluorescence quenching mechanism. This is pivotal for designing future generations of fluorescent azomethines.

1.2 Experimental Section

1.2.1 General Procedures

All reagents were commercially available and were used as received unless otherwise stated. Anhydrous and deaerated solvents were obtained with a Glass Contour solvent purification system. ^{1}H NMR and ^{13}C NMR spectra were recorded on a Bruker 400 MHz spectrometer with the appropriate deuterated solvents.

1.2.2 Spectroscopic Measurements

The absorption measurements were done on a Cary-500 spectrometer while the fluorescence studies were performed on an Edinburgh Instruments FLS-920 fluorimeter after deaerating the samples thoroughly with nitrogen for 20 minutes.

Fluorescence quantum yields were measured at 10^{-5} M by exciting the compounds of study (**1** to **9**) at 303 nm in spectroscopic grade acetonitrile at room temperature and the resulting fluorescence was compared to bithiophene (Φ_{fl} = 0.013 in ethanol).[37]

Fluorescence quantum yields at 77 K were determined by preparing glass matrices of the compounds of study (**1** to **9**) in spectroscopic grade methylcyclohexane and in a 4:1 mixture of ethanol and methanol and by exciting the corresponding compound at its absorption maximum. The resulting emission at 77 K was compared to that obtained at room temperature under identical experimental conditions.

The phosphorescence measurements done at 77 K were carried out on a Cary Eclipse fluorimeter. Solutions of the compound of interest were prepared in spectroscopic

grade methylcyclohexane and excited at multiple local absorption maxima for each compound.

Laser flash photolysis measurements were carried out using an Nd-YAG laser system. Solutions of the compounds of interest were prepared in deaerated and anhydrous spectroscopic grade acetonitrile. The concentrations of the compounds of interest were made to yield absorbances in the range of 0.3-0.4 at the laser excitation wavelength of 266 nm.

1.2.3 Electrochemical Measurements

Cyclic voltammetric measurements were performed on a Bio Analytical Systems EC Epsilon potentiostat. Compounds were dissolved in anhydrous and deaerated acetonitrile containing a concentration of 0.1 M NBu_4PF_6 electrolyte. A platinum electrode and a saturated Ag/AgCl electrode were employed as auxiliary and reference electrodes, respectively.

1.2.4 Bond Rotation Barrier Calculations

Bond rotation barriers were calculated semi-empirically using AM1 calculation methods available in Spartan 06. The bond angles, distances, torsions, and other parameters were experimentally derived from the X-ray data from the corresponding structures.

1.2.5 Synthesis

Phenyl-thiophen-2-ylmethylene-amine (1). In a round-bottomed flask (50 mL) was added 2-thiophenecarboxaldehyde (1.29 g, 1.05 mL) in ethanol (10 mL) to which was added aniline (1.07 g, 1.05 mL) and a catalytic amount of trifluoroacetic acid (TFA). The mixture was refluxed for four hours, and stirred at room temperature for an

additional 15 hours. Complete removal of solvent affords a viscous orange oil which was purified by distillation at reduced pressure (0.8 Torr) yielding the product as an orange oil (75%). M.p.: < 20 ºC. ^{1}H NMR (400 MHz, [D] acetone-d_6); δ = 8.73 (s, 1H), 7.70 (d, 1H, ^{3}J = 5.0 Hz), 7.4 (dd, 1H, ^{3}J = 3.6 Hz, ^{4}J = 1.0 Hz), 7.40 (dt, 2H, ^{3}J = 7.0 Hz, ^{4}J = 1.8 Hz), 7.25-7.18 (m, 4H).

(2-*tert*-butyl-phenyl)-thiophen-2-ylmethylene-amine (2). In an oven-dried, three-necked round-bottomed flask (100 mL) was added 2-*tert*-butylaniline (1.48 g, 1.55 mL) dissolved in anhydrous toluene (30 mL). To this was added 1,4-diazobicyclo-[2.2.2]octane (DABCO, 2.8 g), titanium(IV) chloride, 1.0 M solution in toluene (14 mL), followed by 2-thiophenecarboxaldehyde (1.2 g, 1.0 mL). The mixture was heated at reflux for one hour and the solvent removed. Purification by flash chromatography (SiO_2, 1:99 EtOAc:Hexanes as eluent, 1% Et_3N) yielded the titled product as a yellow solid (50%). M.p.: 74 - 77 ºC. ^{1}H NMR (400 MHz, [D] acetone-d_6): δ = 8.58 (s, 1H), 7.73 (d, 1H, ^{3}J = 5.0 Hz), 7.65 (d, 1H, ^{3}J = 2.8 Hz), 7.39 (dd, 1H, ^{3}J = 7.8 Hz, ^{4}J = 1.3 Hz), 7.23 (m, 2H), 7.15 (dt, 1H, ^{3}J = 7.6 Hz, ^{4}J = 1.4 Hz), 1.44 (s, 9H). ^{13}C NMR (400 MHz [D] acetone-d_6): δ = 153.1, 152.5, 145.6, 144.7, 133.9, 132.3, 129.9, 128.9, 127.7, 127.6, 120.9, 37.1, 31.8. MS: *m/*z 244.11557 $[M + H]^+$ (calculated 244.11545).

Thiophen-2-ylmethylene-(2,4,6-tri-*tert*-butyl-phenyl)-amine (3). In a round-bottomed flask (50 mL) was added 2,4,6-tri-*tert*-butylaniline (100 mg) dissolved in ethanol (15 mL). To this was added a catalytic amount of *para*-toluenesulfonic acid and 2-thiophenecarboxaldehyde (122 mg, 0.1 mL). The mixture was refluxed for 22 hours and the solvent removed. Purification by flash chromatography (SiO_2, 2:98 EtOAc:Hexanes, 1% Et_3N) yielded the product as a pale yellow solid (82%). M.p.: 137 -

139 ºC. ^{1}H NMR (400 MHz, [D] acetone-d_6): δ = 8.27 (ds, 1H, ^{4}J = 0.7 Hz), 7.78 (dt, 1H, ^{3}J = 5.0 Hz, ^{4}J = 1.0 Hz), 7.62 (dd, 1H, ^{3}J = 3.6 Hz, ^{4}J = 1.0 Hz), 7.36 (s, 1H), 7.25 (t, 1H, ^{3}J = 5.0 Hz, ^{4}J = 1.4 Hz), 1.33 (s, 9H), 1.32 (s, 18H). ^{13}C NMR (400 MHz [D] acetone-d_6): δ = 157.9, 151.8, 145.9, 144.5, 140.3, 133.7, 132.9, 129.9, 123.3, 37.4, 36.2, 33.0. MS: *m/*z 356.24164 $[M + H]^{+}$ (calculated 356.24065).

Phenyl-(1-thiophen-2-yl-ethylidene)-amine (4). In an oven-dried, three-necked round-bottomed flask (25 mL) was added aniline (406 mg, 0.40 mL) dissolved in anhydrous toluene (30 mL). To this was added 1,4-diazobicyclo[2.2.2]octane (DABCO, 1.8 g), titanium(IV) chloride, 1.0 M solution in toluene (4.75 mL), followed by 2-acetylthiophene (0.50 g, 0.43 mL). The mixture was heated at reflux for three hours and the solvent removed. Purification by flash chromatography (SiO_2) yielded the titled product as a yellow solid (66%). M.p.: 64 º - 66 ºC. ^{1}H NMR (400 MHz, [D] acetone-d_6): δ = 7.56 (m, 2H), 7.36 (t, 2H, ^{3}J = 7.6 Hz), 7.13-7.08 (m, 2H), 6.85 (dd, 2H, ^{3}J = 8.4 Hz, ^{4}J = 1.0 Hz), 2.22 (s, 3H). ^{13}C NMR (400 MHz [D] acetone-d_6): δ = 160.5, 151.3, 147.1, 130.5, 129.4, 129.3, 128.0, 123.7, 120.2, 16.9. MS: *m/*z 202.06926 $[M + H]^{+}$ (calculated 202.06849).

(2-tert-Butyl-phenyl)-(1-thiophen-2-yl-ethylidene)-amine (5). In a round-bottomed flask (50 mL) was added 2-*tert*-butylaniline (1.38 g, 1.44 mL) dissolved in ethanol (25 mL). To this was added a catalytic amount of *para*-toluenesulfonic acid and 2-acetylthiophene (1.2 g, 1.0 mL). The mixture was refluxed for 22 hours and the solvent removed. Purification by flash chromatography (SiO_2) yielded the product (34%). M.p.: 80 º - 82 ºC. ^{1}H NMR (400 MHz, [D] acetone-d_6): δ = 7.63 (dd, 1H, ^{3}J = 5.0 Hz, ^{4}J = 1.0 Hz), 7.60 (dd, 1H, ^{3}J = 3.7 Hz, ^{4}J = 1.0 Hz), 7.390 (dd, 1H, ^{3}J = 7.9 Hz, ^{4}J = 1.2 Hz),

7.18-7.14 (m, 2H), 7.04 (dt, 1H, ^3J = 7.2 Hz, ^4J = 1.2 Hz), 6.57 (dd, 1H, ^3J = 7.6 Hz, ^4J = 1.3 Hz), 2.25 (s, 3H), 1.34 (s, 9H). ^{13}C NMR (400MHz [D] acetone-d_6): δ = 160.3, 150.8, 148.9, 141.8, 132.1, 130.3, 129.5, 128.1, 127.9, 125.4, 122.3, 36.6, 30.9, 18.8. MS: *m/*z 258.13110 $[M + H]^+$ (calculated 258.1316).

Phenyl-(1-thiophen-2-yl-propylidene)-amine (6). In a round-bottomed flask (5 mL) was added aniline (175 mg, 0.17 mL), 1-(2-thienyl)-1-propanone (261 mg, 0.23 mL) and a catalytic amount of trifluoroacetic acid (TFA). The mixture was stirred under vacuum (0.8 Torr) at room temperature for 20 minutes. Purification by flash chromatography (SiO_2, 4:96 EtOAc:Hexanes, 1% Et_3N) yielded the titled product as an orange oil that turned to brown after one week storage at room temperature (18%). M.p.: < 20 ºC. ^{1}H NMR (400 MHz, [D] acetone-d_6): δ = 7.65-7.62 (m, 2H), 7.35 (t, 2H, ^3J = 7.5 Hz), 7.15 (dd, 1H, ^3J = 4.5 Hz, ^4J = 1.3 Hz), 7.07 (dt, 1H, ^3J = 7.5 Hz, ^4J = 1.0 Hz), 6.80 (dd, 2H, ^3J = 8.4 Hz, ^4J =1.0 Hz), 2.65 (q, 2H, ^3J = 7.6 Hz), 1.15 (t, 3H, ^3J = 7.6 Hz). ^{13}C NMR (400 MHz [D] acetone-d_6): δ = 167.1, 152.7, 147.2, 132.0, 130.8, 130.7, 129.5, 124.9, 121.1, 25.5, 14.8. MS: *m/*z 216.08508 $[M + H]^+$ (calculated 216.08415).

(2-tert-Butyl-phenyl)-(1-thiophen-2-yl-propylidene)-amine (7). In a round-bottomed flask (50 mL) was added 1-(2-thienyl)-1-propanone (270 mg, 0.24 mL), 2-tert-butylaniline (288 mg, 0.30 mL) and a catalytic amount of trifluoroacetic acid. To this was added ethanol (20 mL) and the mixture was refluxed for 25 hours. The solvent was removed and the mixture purified by flash chromatography (SiO_2, 15:85 EtOAc:Hexanes, 1% Et_3N) affording the product as a yellow solid (29%). M.p.: 70 º - 72 ºC. ^{1}H NMR (400 MHz, [D] acetone-d_6): δ = 7.64 (dt, 2H, ^3J = 4.0 Hz, ^4J = 1.0 Hz), 7.39 (dd, 1H, ^3J = 7.9 Hz, ^4J = 1.2 Hz), 7.19-7.15 (m, 2H), 7.04, (dt, 1H, ^3J = 7.6 Hz, ^4J = 1.4 Hz), 6.60 (dd,

1H, ^{3}J = 7.7 Hz, ^{4}J = 1.4 Hz), 2.66 (q, 2H, ^{3}J = 7.6 Hz), 1.33 (s, 9H), 1.24 (t, 3H, ^{3}J = 7.6 Hz). ^{13}C NMR (400 MHz [D] acetone-d_6): δ =164.9, 150.5, 147.8, 141.7, 132.0, 130.2, 129.6, 128.1, 128.0, 125.4, 122.0, 36.8, 31.0, 14.5. MS: *m/*z 272.14643 $[M + H]^{+}$ (calculated 272.14675).

(3-Methyl-thiophen-2-ylmethylene)-phenyl-amine (8). In a round-bottomed flask (10 mL) was added 3-methyl-2-thiophenecarboxaldehyde (240 mg, 0.20 mL), aniline (175 mg, 0.17 mL) and a catalytic amount of trifluoroacetic acid (TFA). To this mixture was added anhydrous ethanol (5 mL). The mixture was heated at reflux 20 hours and the solvent removed. Purification by flash chromatography (SiO_2, 2:98 EtOAc:Hex, 1% Et_3N) afforded the product as a yellow solid (7%). M.p.: 77 º - 79 ºC. ^{1}H NMR (400MHz, [D] acetone-d_6): δ = 8.76 (s, 1H), 7.59 (d, 1H, ^{3}J = 5.0 Hz), 7.39 (m, 2H, ^{3}J = 7.8 Hz, ^{4}J = 2.0 Hz), 7.26-7.19 (m, 3H), 7.05 (d, 1H, ^{3}J = 5.0 Hz), 2.51 (s, 3H). ^{13}C NMR (400 MHz [D] acetone-d_6): δ = 153.8, 144.5, 138.5, 133.0, 131.5, 130.9, 127.5, 122.9, 15.0. MS: *m/*z 202.06921 $[M + H]^{+}$ (calculated 202.06849).

(2-tert-Butyl-phenyl)-(3-methyl-thiophen-2-ylmethylene)-amine (9). In a round-bottomed flask (10 mL) was added 3-methyl-2-thiophenecarboxaldehyde (167 mg, 0.14 mL) and 2-tert-butylaniline (201 mg, 0.21 mL). The mixture was heated at 65 °C and stirred for four hours. Water produced by the reaction was removed *in vacuo* and the residue was purified by flash chromatography (SiO_2, 5:95 EtOAc:Hex, 1% Et_3N) affording the product as a viscous yellow oil (74%). M.p.: < 20 ºC. ^{1}H NMR (400 MHz, [D] acetone-d_6): δ = 8.61 (s, 1H), 7.56 (d, 1H, ^{3}J = 5.0 Hz), 7.38 (dd, 1H, ^{3}J = 7.8 Hz, ^{4}J = 1.4 Hz), 7.22 (td, 1H, ^{3}J = 7.5 Hz, ^{4}J = 1.5 Hz), 7.14 (td, 1H, ^{3}J = 7.5 Hz, ^{4}J = 1.5 Hz), 7.01-6.97 (m, 2H), 2.51 (s, 3H), 1.46 (s, 9H). ^{13}C NMR (400 MHz [D] acetone-d_6): δ =

152.9, 151.7, 144.7, 143.7, 139.1, 133.1, 131.6, 128.9, 127.7, 127.4, 121.1, 37.1, 31.9, 15.0. MS: *m/*z 258.13160 $[M + H]^+$ (calculated 258.13109).

Thieno[2,3-*c*]pyridine (10). The title compound was synthesized according to known methods[40] using the Hendrickson modification of the Pomeranz-Fritsch reaction.

1.3 Results & Discussion

1.3.1 Synthesis

The azomethine compounds reported in Figure 1-1 were chosen as they provide the means for assigning the nonradiative deactivation mode of the singlet excited state of the heteroatomic conjugated bond. The *tert*-butyl groups of the first 3 entries (**1-3**) introduce a steric element enabling a study of the rotation around the N–phenyl bond. Similarly, the 3-methyl substituent on thiophene for **8-9** provides information about hindered rotation around the CH–thiophene bond. Constrained rotation around these two bonds can further be investigated with the ketyl imine derivatives **4-7**.

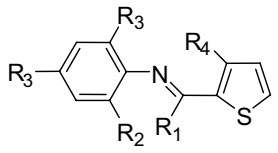

1 R_1=H; R_2=H; R_3=H; R_4=H
2 R_1=H; R_2=^{t}Bu; R_3=H; R_4=H
3 R_1=H; R_2=^{t}Bu; R_3=^{t}Bu; R_4=H
4 R_1=CH_3; R_2=H; R_3=H; R_4=H
5 R_1=CH_3; R_2=^{t}Bu; R_3=H; R_4=H
6 R_1=CH_2CH_3; R_2=H; R_3=H; R_4=H
7 R_1=CH_2CH_3; R_2=^{t}Bu; R_3=H; R_4=H
8 R_1=H; R_2=H; R_3=H; R_4=CH_3
9 R_1=H; R_2=^{t}Bu; R_3=H; R_4=CH_3

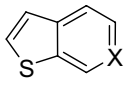

10 X=N
11 X=CH

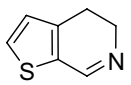

12

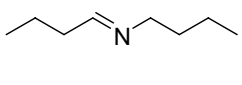

13

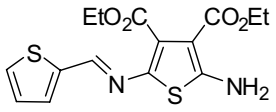

14

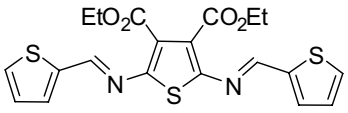

15

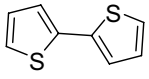

Bithiophene

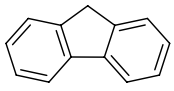

Fluorene

Figure 1-1. Azomethines prepared and investigated in addition to analogues.

The preparation of the azomethine dyads reported in Figure 1-1 was initially attempted by Lewis Acid activation of the aldehyde with $TiCl_4$ under anhydrous conditions. However, McMurray coupled products and other by-products were formed in majority with **3**, rather than the desired products. The desired compounds were subsequently prepared via simple dehydration by refluxing the corresponding reagents in anhydrous alcoholic solvents with a catalytic amount of organic acid.

Alternatively, the azomethines could be prepared in bulk by heating the appropriate reagents to 50 °C along with a catalytic amount of an organic acid such as trifluoroacetic acid. This method accelerated the reaction process to 30 minutes compared to 36 hours of refluxing with the alcohol solvents. In all the cases, the compounds could be isolated in high yields and were all stable to additional purification by column chromatography on silica without additional precautions. This, concomitant with no apparent decomposition over time, confirms that azomethines are robust. Given that the majority of the compounds could be prepared by straightforward condensation methods with little by-products, the preparation of azomethines is a green-route to functional materials.

1.3.2 Crystallographic Study

Single crystal X-ray diffraction studies were carried out to determine the solid state structures. The data generated from these studies were also required for correct optimized geometry input for the semi-empirical calculations. The details of the crystal structure determination of **3** are presented in Table 1-1.

X-ray quality crystals were obtained for **2**, **3** and **5**. As can be seen in Figure 1-2, the planes described by the two aromatic groups are twisted from coplanarity. This is in

contrast to **14** and **15** which are coplanar and highly conjugated.[29,30] The dyads **1**-**9** have a lower degree of conjugation than their all-thiophene analogues as result of the reduced coplanarity. This is supported by the hypsochromic shifts in both the absorption and fluorescence of the dyads relative to **14** and **15**.

Upon the introduction of bulkier species, the dihedral angle between the two aromatic rings increases. The dihedral angles for compounds **2**, **3** and **5** are 44°, 86° and 68°, respectively. The aromatic rings of **3** are nearly perpendicular to one another caused by the bulky *tert*-butyl groups surrounding the azomethine bond. In comparing **2** and **5**, which differ only by the addition of a methyl group on the azomethine carbon, it is evident that substitution on the azomethine is very important for increasing the amount of steric hindrance experienced by the azomethine linkage as the dihedral angle increases by over 20°. As a result of the large dihedral angle between the aromatic planes and the large size of the *tert*-butyl groups, little to no π-stacking is observed in the solid state. This is in contrast to **14** and **15** which form highly organized networks.

Table 1-1. Details of crystal structure determination for **3**.

Formula	C_{23} H_{33} N S
Mw (g/mol); F(000)	355.57 g/mol, 1552
Crystal color and form	Yellow needle
Crystal size (mm)	0.16 x 0.07 x 0.02
T (K); $d_{calcd.}$ (g/cm^3)	138 (2) ; 1.096
Crystal System	Monoclinic
Space Group	C 2/c
Unit cell: *a* (Å)	38.898(3)
b (Å)	6.1786(5)
c (Å)	19.3956(18)
α (°)	90.000
β (°)	112.449(4)
γ (°)	90.000
V (Å^3); Z	4308.2(6) ; 8
Θ range (°) ; completeness	70.40 ; 0.975
Reflections: collected / independant; R_{int}	17194 / 4026 ; 0.0953
μ (mm^{-1}) Abs. Corr.	1.343
R1(F); wR(F^2) [I > 2σ(I)]	0.0743 ; 0.1743
R1(F); wR(F^2) (all data)	0.1471 ; 0.2173
GoF (F^2)	0.985
Max. residual e– density	0.372

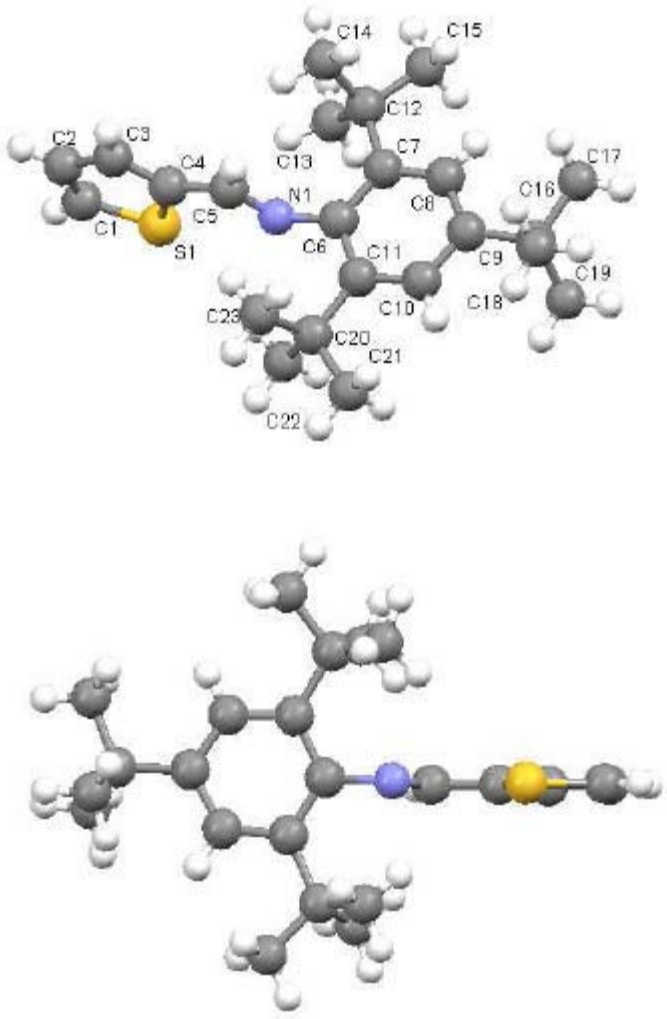

Figure 1-2. Crystallographic structure of **3** as shown along the a axis (top) and b axis (bottom).

1.3.3 Bond Rotation Barriers

The rotation barriers of the aryl groups adjacent to the azomethine bond were calculated semi-empirically using AM1. The experimental parameters derived from the X-ray structures of the corresponding azomethines were used for both the starting geometries and parameters for calculating the heats of formation (ΔH_f). Even though the absolute ΔH_f for each rotamer cannot be precisely calculated semi-empirically, an accurate bond rotation barrier can nonetheless be calculated from the relative energies. A representative rotational barrier energy diagram for **3** derived from these calculations is

shown in Figure 1-3. This a preferred method for determining the rotation barrier over standard NMR methods via coalescence temperatures since the compounds studied do not have required coupled protons allowing for such measurements.

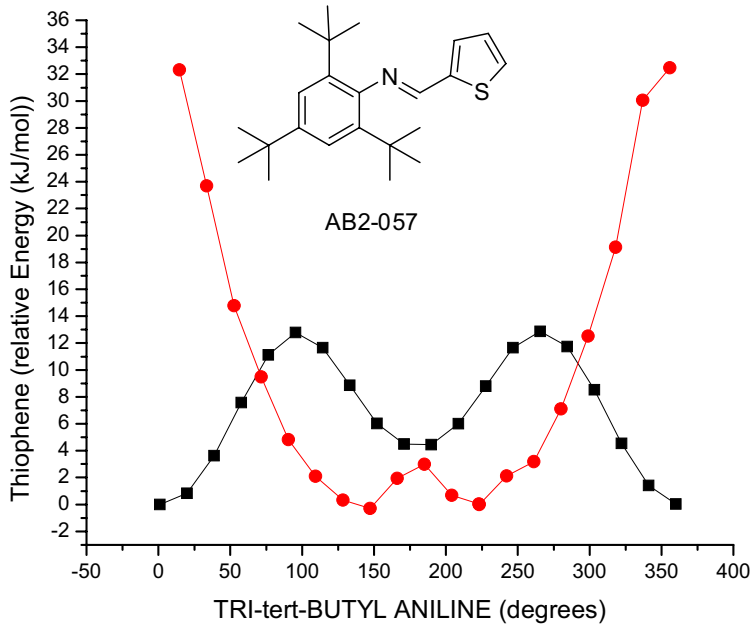

Figure 1-3. A representative rotational barrier energy diagram for **3** semi-empirically calculated for =N–aryl (●) and =CH–thiophene (■) bond rotation.

The calculated rotational barriers calculated from the ΔH_f of the different rotamers are tabulated in Table 2. The effects of substitution on the azomethine and the 2-positions of the thiophene and phenyl on the CH–thiophene and N–aryl bond rotations, respectively, are evident from the calculated data. The bond rotation energy for CH–thiophene is roughly 12 kJ/mol regardless of the substitutions made on the azomethine and thiophene rings, or the aryl groups attached to the azomethine bond. This is supported by the similar barriers calculated for **14**, and the other azomethines reported in Figure 1-1.

Table 1-2. Rotational barriers for various azomethine dyads semi-empirically calculated using AM1 starting from the X-ray crystal structure data.

Compound	N–Phenyl (kJ/mol)	CH–Thiophene (kJ/mol)
1	14	5
2	33	13
3	32.5	13
4	11	10
5	87	5
6	12	9
7	811	8
8	15	5
9	33	13
14	15	15

Conversely, the N–aryl bond rotation is highly dependent upon the substituents. The bond rotation barrier increases by a factor of three compared to that for the CH–thiophene barrier as a result of the *ortho*-*tert*-butyl group. Given the similar values calculated for **2, 3** and **9,** it can be concluded that substitution of the thiophene does not affect the barrier of rotation. This is in contrast to azomethine alkylation and incorporating the *tert*-butyl group on the phenyl which collectively contribute to increase the N–aryl bond rotation barrier.

This is evidenced by the higher rotational barriers calculated for both **5** and **7**. Although the bond distances are longer in the excited state, the calculated bond rotational barriers for the ground state are not expected to be significantly different than for the corresponding excited state.[41,42] Even if the extended bond distances in the excited state lower the bond rotation barrier, the rotational barriers of **5** and **7** should remain significantly higher than the other dyads. The rotation barrier data nonetheless demonstrate that these two azomethines should exhibit increased fluorescence relative to

their homologues if rapid excited state deactivation by bond rotation occurs for the azomethines.

The hindered rotation is further evidenced by the X-ray crystal data showing the lowest energy rotamer where the mean plane angle of the phenyl group relative to the azomethine bond is 65 ^{o} and 53 ^{o} for **5** and **7**, respectively (*vide supra*). This is in contrast to **14** that has relatively low rational barriers and whose X-ray structures show the thiophenes are co-planar to the azomethine bond.[29,30] The calculated barriers combined with the XRD data confirm that the compounds exhibit different rotation barriers. Singlet excited state deactivation via bond rotation can therefore be confirmed with the selected azomethines.

1.3.4 Spectroscopic Studies

Given the significant bond rotation barriers calculated for **5** and **7**, these should exhibit increased fluorescence relative to the other azomethines if efficient singlet excited state deactivation occurs by either N–aryl or CH–thiophene bond rotation. However, only extremely weak fluorescence was observed for all the azomethines despite both their substitution and changes in solvent polarity. These results are shown in Table 1-3.

Very little difference in fluorescence was also observed at 77 K for **1**-**9**, as seen in inset of Figure 1-4. Since all modes of deactivation by rotation are suppressed at this low temperature, deactivation by the internal conversion means of bond rotation would result in increased fluorescence.

Table 1-3. Spectroscopic data for compounds **1-9**, **10**, **11** and **14**. Values listed were recorded in acetonitrile solutions. Phosphorescence measurements were recorded in methylcyclohexane.

Compound	λ_{abs} (nm)	$\lambda_{Sh.}$ (nm)	λ_{fl} (nm)	ΔE (nm)	λ_{Phos} (nm)	φ_{fl} (10^{-3}) (298)K	E_g^{spec} (eV)	E_g^{echem} (eV)
1	298	269, 326	396	345	437, 701	2.3	3.6	3.1
2	298	268, 339	310	305	510, 706	0.8	4.1	3.2
3	283	264	311	294	516, 704	0.9	4.2	3.4
4	284	263	313	300	516, 700	2.5	4.1	3.2
5	288	263	316	298	510, 708	0.4	4.2	3.8
6	257	283	336	307	-	1.7	4	3.4
7	263	231, 284	402	N/A	512, 708	1.6	4.1	3.5
8	287	335	398	364	524, 716	5.4	3.4	3.5
9	298	341	425	362	-	-	3.4	3.7
10	298	-	415	307	-	3.6	4	-
11	227	298	298	294	430	19	4.2	-
14	400	-	480	425	691	2.9	2.9	2.6

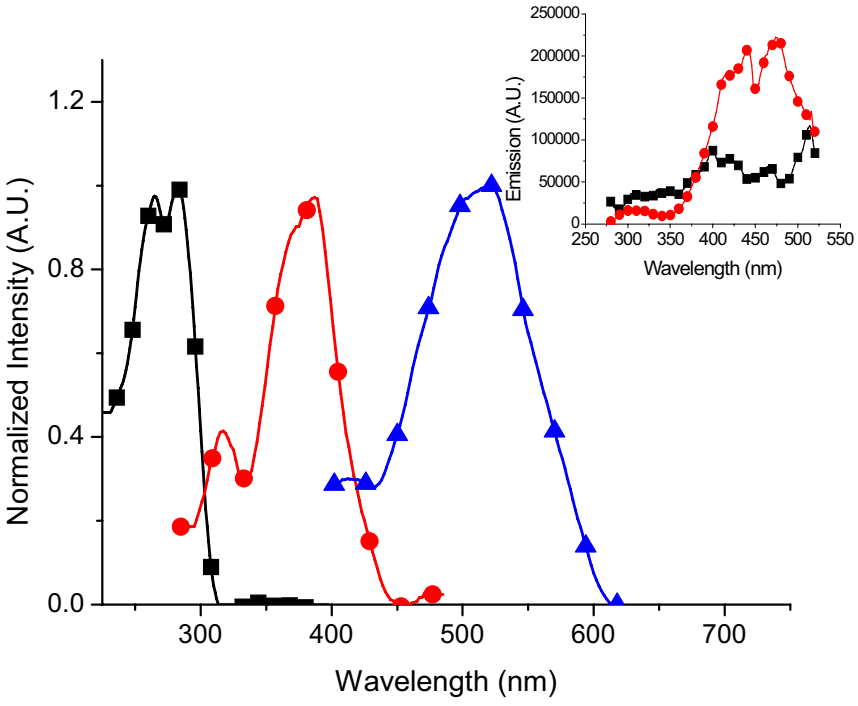

Figure 1-4. Normalized absorbance (■), fluorescence (●), and phosphorescence (▼) spectra of **3** in methylcyclohexane. Inset: Fluorescence spectrum of **3** at room temperature magnified ten times (■) and at 77 K (●)measured in a 4:1 ethanol:methanol matrix.

Further evidence of deactivation by means other than bond rotation is obtained from **10**, which also does not fluoresce. This compound should exhibit enhanced fluorescence compared to **1**-**9** because rotation around either the N–aryl or CH–thiophene bond is not possible. The absence of fluorescence of **10** implies that azomethine fluorescence quenching occurs via another deactivation mode.

The similarly weak fluorescence yields of **10** and **11** imply that thiophene is inherently a weak fluorophore. This is in contrast to oligothiophenes whose fluorescence yield increases with increased degree of conjugation.[36,37] Similary, thiophene vinylenes fluoresce significantly more than their azomethine derivatives. The weak fluorescence notwithstanding, the fluorescence yield of **11** is five times greater than **10**,[43,44] confirming that the heteroatomic bond contributes to fluorescence deactivation. The lack of increased azomethine fluorescence at 77 K concomitant with the nonexistent fluorescence quantum yields unequivocally confirms that internal conversion is not a major deactivation mode of azomethine singlet excited state deactivation.

1.3.5 Singlet Manifold

Useful information concerning the excited state deactivation processes is derived normally from fluorescence lifetime measurements. Unimolecular decays on the order of a few ns were observed for the studied azomethines. However, accurate fast lifetime measurements could not be obtained owing to the weak azomethine fluorescence concomitant with the instrument time resolution. Fluorene and bithiophene were subsequently used to probe the azomethine deactivation by steady-state fluorescene.

Even though thiophene is the ideal model system for investigating the fluorescence deactivation by the azomethine bond for the compounds studied,

bithiophene was selected owing to its stronger fluorescence.[37] Similarly, the deactivation of fluorene was examined because of its inherent fluorescence (Φ_{fl}=0.78).[29] The aliphatic azomethine (**13**) was used for probing the fluorescence quenching of the two fluorophores. This quencher was chosen because fluorescence deactivation uniquely from the heteroatomic bond can be followed. The different singlet excited state energies of fluorene (404 kJ/mol)[45] and bithiophene (358.2 kJ/mol)[36] further allow examining the energetics and quenching kinetics with **13**.

The fluorescence quenching kinetics and efficiencies can be derived using the Stern-Volmer method by examining the change in fluorescence as a function of quencher concentration [**13**] according to: $\Phi_0/\Phi = 1 + k_q \bullet \tau^{-1} \bullet [\mathbf{13}]$, where Φ_0 is the fluorescence in the absence of quencher, Φ the fluorescence with quencher, k_q the second order fluorescence quenching rate constant, and τ is the fluorophore fluorescence lifetime in the absence of quencher. A typical Stern-Volmer fluorescence quenching with **13** is shown in Figure 1-5. The quenching rate constants (k_q) calculated from the fluorophore lifetime for both fluorene and bithiophene in acetonitrile were 1 x 10^{10} and 7 x 10^{10} M^{-1} s^{-1}, respectively. The k_q for bithiophene is slightly greater than the diffusion limit in acetonitrile (k_{diff} = 2 × 10^{10} M^{-1} s^{-1}) owing to inaccurate fluorescence lifetimes of bithiophene.[36,37] This aside, fluorescence deactivation by **13** is diffusion controlled in acetronitrile. Similarly, the fluorene fluorescence lifetime was quenched with **13** at near diffusion controlled limits of k_q = 2.5 x 10^{10} M^{-1} s^{-1}.[42] The time resolved fluorescence confirms that fluorophore quenching by azomethines is a dynamic process.

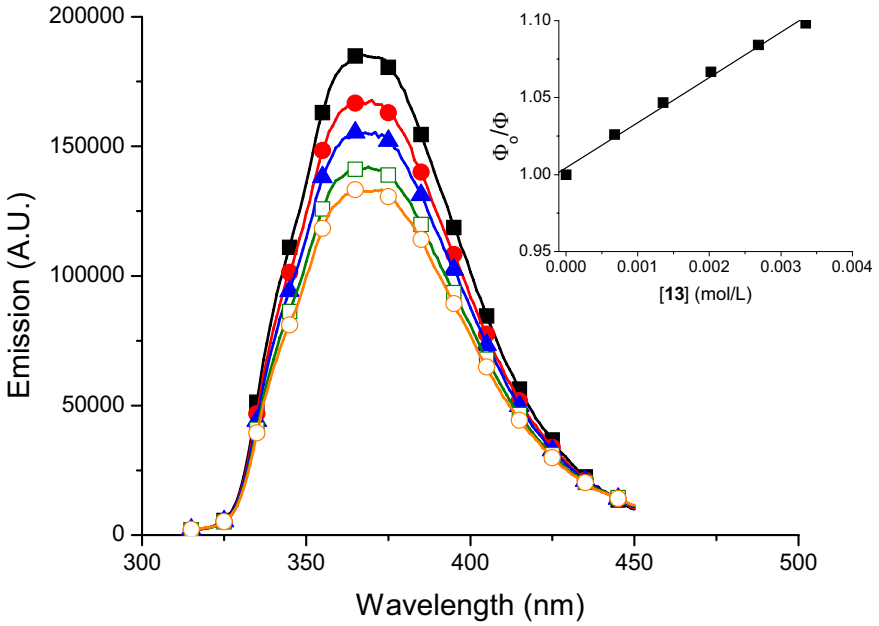

Figure 1-5. Fluorescence quenching of bithiophene in acetonitrile as a function of [**13**]: (0 mM (■) through 3.3 mM (●), 6.6 mM (▲), 12.8 mM (□) and 18.6 mM (○)). Inset: Stern-Volmer relationship of describing bithiophene fluorescence changing with [**13**].

The fast fluorescence deactivation implies that the azomethine deactivation occurs by photoinduced electron transfer from the fluorophore's excited singlet state to the azomethine acceptor. The fast rate constant also suggests that PET is efficient. The amount of quencher required for quenching 95 % of the produced singlets can be calculated according to: 20 x k_o / k_q, where k_o is the inherent lifetime of the fluorophore in the absence of quencher and k_q is the quenching rate constant derived from the Stern-Volmer quenching experiments. From the measured k_q and fluorene fluorescence lifetime, it can be calculated that only 160 mM of **13** is required for quenching 95 % of the singlet excited states of fluorene by intermolecular or intramolecular PET.

For intramolecular deactivations, the fluorophore and quencher are covalently linked and diffusion is not required for deactivation. The concentration of excited state

species produced under such conditions is ca. μM while the fluorophore ground state concentration is ca. 3 M.[46] The azomethine bond of **1**-**9** is in a 20 fold excess to what is required to quench 95 % of the singlet excited states when these azomethines are excited. This leads to rapid and efficient fluorescence quenching by intramolecular PET by the azomethine bond. The excess inherent azomethine concentration in the ground state concomitant with rapid k_q confirms that the suppressed azomethine fluorescence is a result of efficient intramolecular PET.[47,48] Radical ion formation would unequivocally confirm PET. However, such products cannot be formed for the dyads since the back electron transfer reaction is also favoured and that the radical ions cannot diffuse apart once they are formed.

Additional evidence for PET quenching is derived from the complementarity of the electron donor and acceptor energy levels. The fluorophore donor and the azomethine acceptor's suitability of undergoing PET can empirically be calculated according to the Rehm-Weller equation[49]

$$\Delta G^{\circ}_{eT} = E_{pa}\,(\text{fluorophore}) - E_{pc}\,(\text{quencher}) - \Delta E_{0,0} - \lambda.$$

The relationship takes into account the fluorophore's capacity to donate an electron (E_{pa}), the azomethine's capacity to accept the electron to be transferred (E_{pc}), and the solvent reorganization energy (λ). The E_{pa} and E_{pc} correspond to the oxidation and reduction potential of the fluorophore and azomethine, respectively. These values required for the Rehm-Weller equation can be measured by cyclic voltammetry (Figure 1-6, inset) from the oxidation and reduction potential for the electron donor and acceptor, respectively.

Table 1- 4. Oxidation and reduction potentials for **1-9**, **13**, and the model compound bithiophene from cyclic voltammetry measurements in anhydrous and deaerated acetonitrile and calculated energetic of electron transfer.

Compound	E_{pa} (V) vs. Ag/AgCl	E_{pc} (V) vs. Ag/AgCl	$\Delta G°$ (kJ/mol) Bithiophene[a]
1	1.2	-1.9	-44
2	1.2	-2	-35
3	1.4	-	-
4	1.5	-1.7	-69
5	1.5	-2.3	-6
6	1.5	-	-
7	1.4	-	-
8	1.6	-1.9	-44
9	1.6	-2.1	-25
13	-	-1.1	-121

[a]*Electronic transfer energetics calculated from the Rehm-Weller equation for quenching of bithiophene by the various azomethines.*

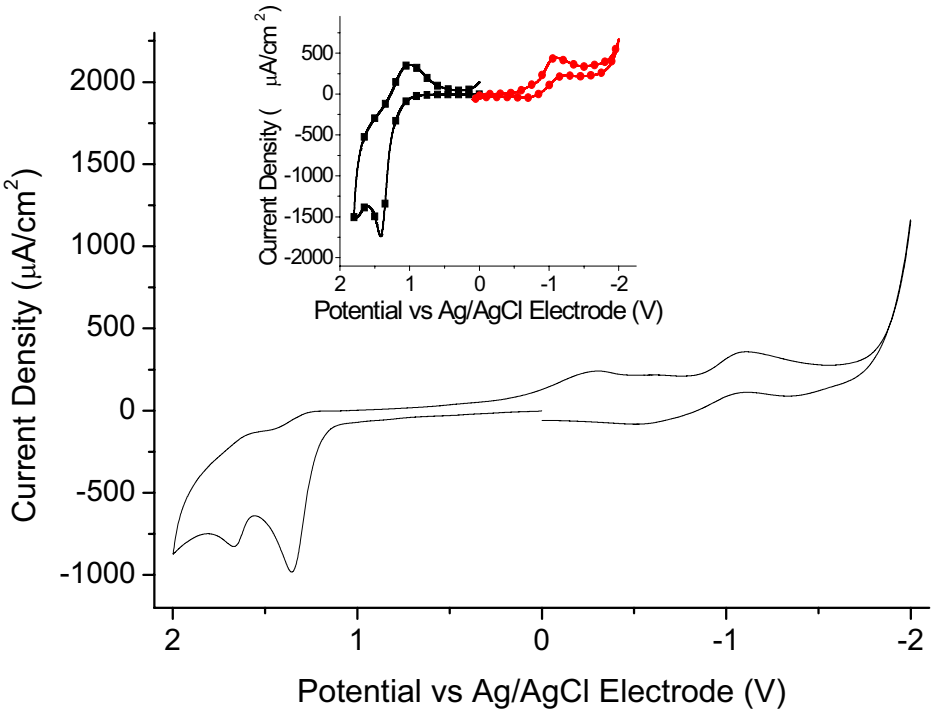

Figure 1-6. Cyclic voltammogram of **3** measured in acetonitrile. Inset: Cyclic voltammogram of bithiophene, anodic (■) scans and **13** cathodic (●) scans as measured in acetonitrile at sweeprate of 100 mV/sec.

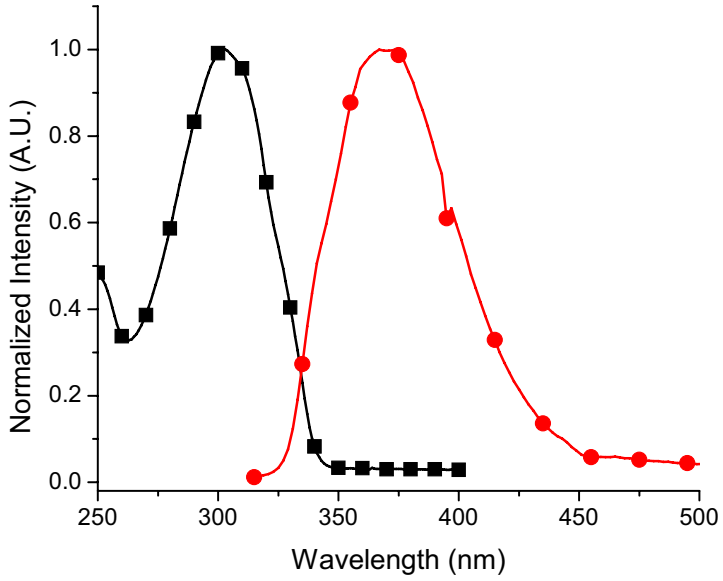

Figure 1-7. Normazlied absorbance (■) and fluorescence (●) spectra of bithiophene measured in anhydrous and deaerated acetonitrile

The corresponding redox potentials measured for bithiophene and **13** are reported in Table 1-4. The energy gap ($\Delta E_{0,0}$) between the ground and excited singlet states of the fluorophore must also be taken into account since PET involves electron transfer from its excited state. This is calculated from the intercept of the normalized plot of the absorption and fluorescence spectra of the fluorophore, illustrated in Figure 1-7.

The calculated energetics of PET for the bithiophene-imine quencher (**13**) donor-acceptor couple is favourable (-121 kJ/mol). The energetics of intramolecular PET are equally exergonic (-25 to -69 kJ/mol) for the azomethines **1-9** as derived from the corresponding the oxidation and reduction potentials recorded in Table 1-4. The quenching studies of **13** confirm that azomethines efficiently quench the singlet excited state via PET. In addition, the electrochemical and spectroscopic data of **1-9** confirm that intramolecular PET is energetically possible. The calculated exergonic values from the

Rehm-Weller equation, the measured diffusion controlled k_q for intermolecular PET, and the 20 fold excess of ground state azomethine prove that intramolecular PET is an efficient mode of singlet excited state deactivation for azomethines.

Azomethine protonation not only effects the azomethine E_{pc}, but it further changes the HOMO and LUMO energy levels such that the $\Delta E_{0,0}$ varies. By perturbing both the $\Delta E_{0,0}$ and E_{pc} of the fluorophore-azomethine pair, PET can be disfavoured, and hence, turned-off. Increased fluorescence should therefore be observed with azomethine protonation resulting from PET being switched off. Protonation of **1** and **4** with trifluoroacetic acid in anhydrous acetonitrile resulted in fluorescence increases of only 60% and 37%, respectively, while increases on the order of 400% were expected. Despite a marginal increase, the fluorescence is not significantly restored to that of inherently fluorescent fluorophores. The observed increased is consistent with the fluorescence difference between **10** and **11**, which differ only with the heteroatom. The increased fluorescence observed with azomethine protonation confirms that PET is responsible for quenching the azomethine fluorescence. However, since the fluorescence of **1** and **4** are not increased by 400%, another nonradiative mechanism for excited state deactivation competes with PET.

1.3.6 Triplet manifold

According to the following energy conservation equation the sum of all the excited state deactivation processes ($\Phi_{fl} + \Phi_{IC} + \Phi_{PET} + \Phi_{PI} + \Phi_{ISC}$) must equal unity, where PI is photoisomerization. Φ_{fl} and Φ_{IC} are negligible since azomethines do not fluoresce and they are not deactivated by internal conversion (IC) confirmed by the temperature dependant fluorescence measurements according to $\Phi_{IC} \approx \Phi_{fl}$ (77 K) - Φ_{fl}

(298 K). Moreover, the slight fluorescence increase upon azomethine protonation confirms that $\Phi_{PET} < 0.1$. The energy conservation equation can further be simplified to: $\Phi_{PET} + \Phi_{ISC} \approx 1$ considering that no photoisomers (PI) were observed and that azomethines are not known to undergo PI.[50] Azomethine singlet excited state deactivation thus occurs by both PET and intersystem crossing (ISC) to form the triplet state.

Laser flash photolysis of the azomethines was used for confirming triplet manifold formation by ISC. The triplet transient produced should be spectroscopically detected and quantified with this technique. However, no triplet was detected for **1**-**9**. Phosphorescence measurements were subsequently done in glass matrices at 77 K. At this low temperature, collision deactivation processes that would otherwise thermally deactivate the triplet are eliminated. Weak phosphorescence can subsequently be seen if the triplet state is formed. Even though phosphorescence was observed for all the azomethines studied, only qualitative information regarding the triplet state can be obtained in part because $\Phi_{phos} < \Phi_{ISC}$. Azomethine phosphorescence confirms that the triplet is produced at 77 K, but that it is efficiently deactivated at room temperature.

Bithiophene was examined by LFP in order to understand the absence of azomethine transient signal. Bithiophene was chosen because it produces a visible triplet detectable by LFP and it serves as a model thiophene compound whose lifetime can be monitored.[37,51] The bithiophene triplet was quenched by the imine **13** as seen in the inset of Figure 1-8. The decrease in signal intensity with added **13** implies static quenching while the shortened lifetime suggests dynamic quenching.

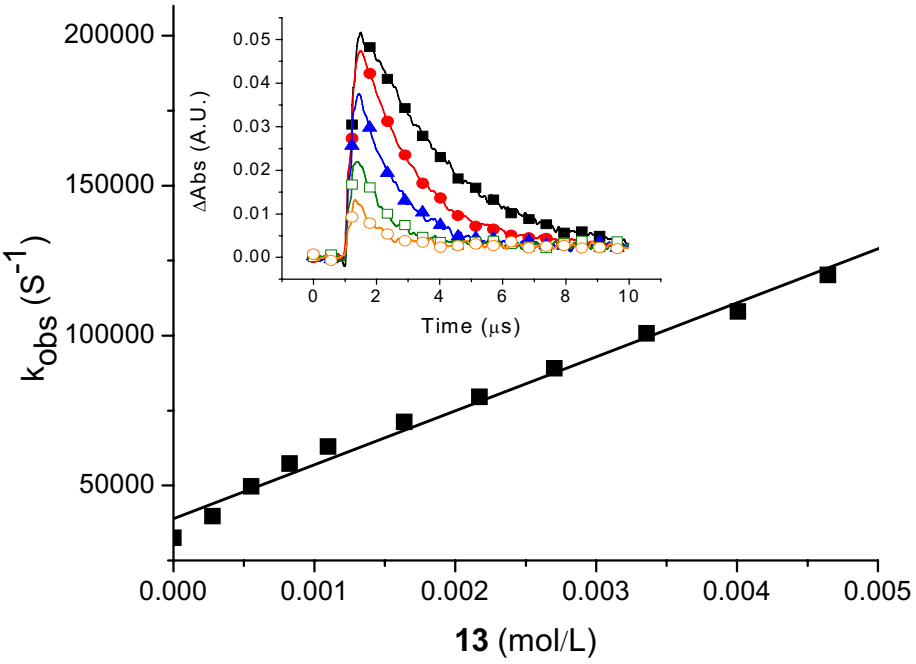

Figure 1-8. Change in the first order rate constant of triplet decay of bithiophene as a function of [**13**] in anhydrous and deaerated acetonitrile. Inset: Triplet decay of bithiophene as a function of [**13**] (0 mM (■) through 0.8 mM (●), 2.2 mM (▲), 4.0 mM (□) and 7.7 mM (○)) in deaerated and anhydrous acetonitrile excited at 266 nm and monitored at 380 nm.

The change in the triplet decay rate constant as a function of added imine quencher **13** leads to the Stern-Volmer plot seen in Figure 1-8. The second order quenching rate constant (k_q) is derived from the slope similar to the fluorescence studies (*vide supra*). The calculated k_q is 2 x 10^7 M^{-1} s^{-1}. The slower than diffusion controlled quenching process is most likely a result of the triplet energy of **13** being higher than that of bithiophene.[36,42] This notwithstanding, only 20 mM of **13** is required to quench 95 % of the bithiophene triplets produced by intermolecular energy transfer. This is derived from the measured k_q and k_o. Although only 20 mM of **13** is required for efficient triplet quenching, the effective azomethine concentration for intramolecular self-quenching with

1-9 is 150 times in excess. Therefore, any triplet of **1-9** that is produced is quenched by intramolecular energy transfer to the azomethine within ca. 5 ns. This lifetime is much shorter than the shortest time measurable by the LFP instrument. The high effective azomethine concentration available for intramolecular triplet quenching results in fast triplet deactivation of **1-9** by energy transfer to the azomethine and no apparent signal by LFP.

1.4 Conclusions

It was demonstrated that azomethines can efficiently deactivate both the singlet and triplet excited states. Therefore, when using these heteroatomic bonds for preparing functional materials, their fluorescence will be completely suppressed resulting from efficient intramolecular self-quenching regardless of the fluorophore. Fluorescence can be restored by protonating the azomethine. Protonation perturbs the donor-acceptor energy levels, exergonically disfavouring PET such that quenching of the singlet excited state by this method is suppressed. Even though the fluorescence can potentially be restored by protonating the azomethine, competitive deactivation of the singlet excited state by ISC must also be considered. This is particularly important since increasing the degree of conjugation modifies the singlet-triplet energy gap and favours ISC.

This is the case with polyazomethines, which are highly conjugated. Formation of the triplet state was observed for the azomethine dyads investigated. This manifold is deactivated via rapid intramolecular energy transfer to the azomethine, occurring much faster than the time resolution of the LFP instrument. Therefore, the azomethine group efficiently deactivates both the singlet and triplet excited states resulting in the

suppressed azomethine fluorescence regardless if intrinsically fluorescence fluorophores are incorporated into the azomethine.

By perturbing the singlet excited state, azomethine protonation also affects the conjugation degree, which in turn, modifies the singlet-triplet energy gap. By choosing inherently fluorescent fluorophores, azomethines can be made highly fluorescent. Azomethine fluorescence can be restored by azomethine protonation resulting in the combined effect of turning off intramolecular PET and reducing ISC by increasing the singlet-triplet energy gap. Subsequently, azomethine fluorescence can switched either on or off by acid protonation. The photophysical properties of azomethines can thus be tuned to match those of their carbon analogues. Taking into account their simple synthesis and green protocols requiring little purification concomitant with their robustness and electrochemical properties, azomethines are viable alternatives for functional materials. This is especially true since their fluorescence can be tuned to equal their carbon analogues.

1.5 Acknowledgements

The authors acknowledge financial support from the Natural Sciences and Engineering Research Council Canada, le Fonds Québécois de la Recherche sur la Nature et les Technologies, and additional equipment funding from the Canada Foundation for Innovation. S.D. and A.B. both thank NSERC Canada for graduate scholarships.

Chapter 2: Synthesis and Characterization of Thiophene Azomethine Metal Complexes

2.1 Introduction

The work presented in this section is based on the formation of metal complexes using various thiophene azomethine ligands. The ligands can be broken down into two categories depending on the heterocycles coupled by the azomethine linkages. The first set of ligands are composed of two or three thiophene rings each separated by an azomethine linkage. The second ligand set contains a hydroxyquinoline moiety linked to a thiophene ring through an azomethine bond.

The choice of azomethine ligand is two-fold. The first reason is that azomethine synthesis is relatively simple; a one-pot reaction that can be easily purified in high yield.[52] Secondly, the study of azomethine photophysics is a central theme of this research group.[30,33,53] As previously discussed, azomethine fluorescence is nonexistent in nearly all cases. To further investigate this curious effect, the azomethine linkage can be used to coordinate with metals thereby restricting the bond rotations and vibrations associated with the azomethine linkage. In Chapter 1, it was shown that increased steric bulk around the azomethine linkage caused an increase in the bond rotation barriers about the thiophene-CH and the N-aniline bonds in the dyads **1-9**.

The processes of bond rotation and vibration are important in defining the quantum yield of internal conversion, Φ_{IC}, for an excited state undergoing decay. Decreasing the contribution of Φ_{IC} could result in an increase in fluorescence, Φ_{fl}, as the other values in equation **E-1** should not change significantly with metal complexation. Therefore, metal complexation could be used to increase the amount of fluorescence observed for azomethine containing ligands by constraining the internal conversion processes of bond rotation and vibration.

The hydroxyquinoline functionality was chosen as a model compound for many reasons. A discussion presenting the benefits and applications of hydroxyquinoline type ligands will be presented in section 2.1.2. At this point, it is important to point out that various quinoline-type molecules and complexes find use in industrial technological applications (e.g. organic light emitting devices),[54,55,56,57] in biological roles (e.g. photosynthetic system II)[58,59] and biological applications (e.g. antifungal medications)[60] as well as in other applications such as metal ion sensors.[61,62]

The ligands synthesized in this work are multidentate. This is important as multidentate ligands play a central role in the field of supramolecular chemistry. A secondary goal of this work was to develop supramolecular structures derived from the polymer-like structure that can form in the presence of multidentate ligands. Structures of interest in supramolecular chemistry include coordination polymers, molecular grids and boxes, as well as multistrand helicies. Supramolecular chemistry will be briefly discussed later in this report.[63,64,65]

The complexes formed in this work were characterized mainly through UV-vis absorbance and fluorescence spectroscopy. NMR spectroscopy and mass spectrometry were used to study the ligands in the free state, but the metal complexes proved difficult to study by these methods due to low solubility and interference with the magnetic field. Cyclic voltammetry studies of the ligands were also carried out, but once again, solubility issues made analyses of the complexes unreliable.

2.1.1 Azomethine Ligands and Polythiophenes

Molecules containing azomethine (C=N) linkages have recently been studied as suitable replacements for currently used conjugated organic materials due to the fact that the azomethine linkage is isoelectronic with the ethene (C=C) linkage.[30,33,53] The delocalization of the π-type electrons allows for aromatic conjugation through the azomethine bond. In this respect, azomethine containing molecules can show a high degree of aromatic conjugation which makes them attractive molecules for applications in organic electronic devices (i.e. organic light-emitting diodes [OLEDs], field effect transistors [OFETs], etc.).

Azomethines can be synthesized rapidly in high yields using simple reaction conditions. Azomethines are frequently synthesized in facile, one-pot reactions that do not require the use of metal catalysts.[30,33,53,64] For this reason, azomethines are very attractive as functional materials due to the ease with which they can be produced. The reactions used to produce them can be scaled up without a significant loss in yield. Due to a high chemical stability and resistance to reduction, the purification of these molecules is made quite simple. They are, however, susceptible to acid-catalyzed hydrolysis and therefore must be protected from acids.[33,66]

The addition of a thiophene moiety to the aromatic core of an azomethine molecule is useful in that it affords a lower oxidation potential than its benzene analogues.[33] Polythiophene type polymers are widely used in electronic devices with materials like polyethylenedioxythiopene (PEDOT) being a main component of the conducting layer of many laboratory synthesized electronic devices.[67] Polythiophene has been shown to be a material that conducts electricity very efficiently. For this reason,

amongst others, thiophene containing materials are chosen as starting points for the design of new conducting materials.

The addition of thiophene to the materials studied in this work not only moderates the electrochemical properties of those materials, but it can also be used to serve as a chelation site in metal complexation reactions. One of the lone pairs on the sulfur atom in thiophene is used in producing the aromaticity in thiophene rings while the other is available as a chelating lone pair. The azomethine nitrogen also demonstrates this property with its lone pair available for chelation. Azomethine materials are useful for the development of metal complexes for this reason.[68,69,70]

2.1.2 Hydroxyquinoline Ligands

Quinoline and hydroxyquinoline-based ligands used in metal complexation reactions have been studied extensively in the past owing to their strong chelating capabilities and the fact that quinolines are an important molecule in many biological systems.[58,59] In addition to their biological relevance, quinoline complexes serve an important role in techonology. Tris(8-hydroxyquinoline)aluminum (AlQ_3), a complex that uses hydroxyquinoline as a bidentate ligand, is the most widely used blue-emitting layer in organic light emitting devices (OLEDs).[56,57]

The extensive use of quinoline-based molecules comes from multiple physical characteristics. Quinoline is a bi-cyclic molecule containing two fused rings, one of benzene and one of pyridine. Hydroxyquinoline often takes the form of 8-hydroxyquinoline, where its hydroxyl group is found in the same position on the benzene ring as is the nitrogen in the pyridine ring. This is important as it gives the ligand a

strong, bidentate chelating site.[55] Figure 2-1 depicts the bidendate chelation site of 8-hydroxyquinoline (8-HQ).

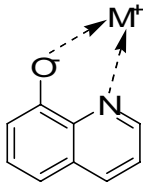

Figure 2-1. Structure and bidentate chelation site of 8-hydroxyquinoline (8-HQ).

The HOMO-LUMO levels on hydroxyquinoline are displaced over the bi-ring system. The result of this is that the HOMO-LUMO levels can be easily tuned to vary the resultant photophysical and electrochemical properties of the ligand, and consequently, the properties of any metal complexes formed from these ligands.[55,71,72]

Substitutions on the hydroxyquinoline ring are often made at the 5-position, para- to the hydroxyl group. Substitutions at the 5-positions including chromophores, electron-withdrawing and donating groups, or chains containing long alkyl spacers can significantly effect the photophysics of the system. The addition of different functional groups on the 2-, 4-, and 5-positions of hydroxyquinoline units has demonstrated a significant variation in the photophysics of substituted quinolines.[55,60,72,73]

Quinoline-based derivatives can also be used to determine the presence of metal ions in solution. Due to their variable photophysical properties, strong, naked-eye visible colour changes can be effected by complexation with a specific metal ion. The obvious device design in this case is a small, portable metal-ion sensor that can be used in the field to detect the presence of metal ions in drinking water when access to an analytical chemistry lab is either impractical or impossible.[61,62,74]

In addition, substituting the 5-position with a molecular fragment containing more chelation sites can give the entire ligand the ability to be tridentate, tetradentate or even more chelating. Substitutions can include the insertion of N=N bonds, C=N bonds and the addition of other chelating units like pyridine and quinoline units.[75]

Molecules with a high degree of denticity, that is four or more chelation sites, are widely used in the field of supramolecular chemistry to form higher order molecular structures like mulitstrand-helices, molecular frameworks like grids and boxes, as well as other higher order aggregates based on the smaller supramolecular structure.[76,77] An example of a supramolecular polymer based on a tetradentate hydroxyquinoline-pryidine ligand is shown in Figure 2-2.

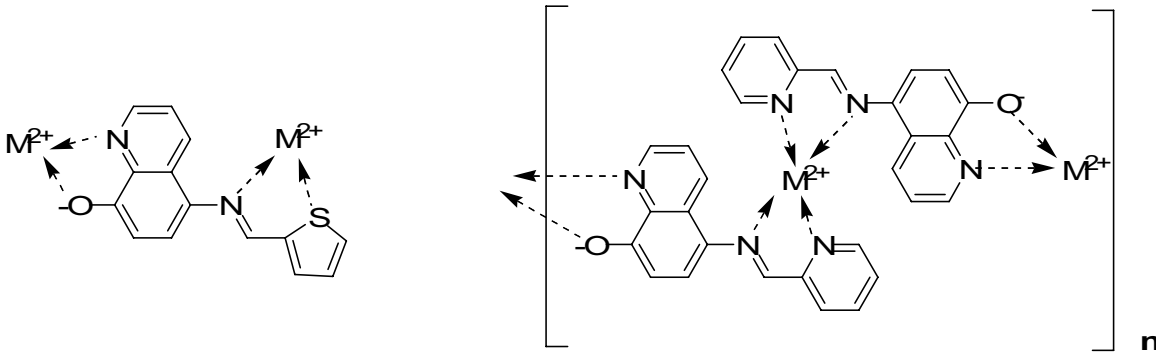

Figure 2-2. An example of the possible chelation modes of ligand $\mathbf{L_4}$ (left). An example of a coordination polymer, a supramolecular structure formed by metal coordination with a multi-dentate ligand (right).

2.2 Experimental Section

2.2.1 General Procedures

All reagents were commercially available and were used as received unless otherwise stated. Anhydrous and deaerated solvents were obtained with a Glass Contour solvent purification system. ^{1}H NMR and ^{13}C NMR spectra were recorded on a Bruker 400 MHz spectrometer with the appropriate deuterated solvents

2.2.2 Spectroscopic Measurements

The absorption measurements were done on a Cary-500 spectrophotometer while the fluorescence studies were performed on an Edinburgh Instruments FLS-920 fluorimeter after deaerating the samples thoroughly with nitrogen for 20 minutes.

Fluorescence quantum yields were measured at 10^{-5} M by exciting the compounds of study at 303 nm in spectroscopic grade ethanol at room temperature and the resulting fluorescence was compared to bithiophene ($\Phi_{fl} = 0.013$ in ethanol).[30]

2.2.3 Electrochemical Measurements

Cyclic voltammetric measurements were performed on a Bio Analytical Systems EC Epsilon potentiostat. Compounds were dissolved in anhydrous and deaerated dichloromethane containing a concentration of 0.1 M NBu_4PF_6. A platinum electrode and a saturated Ag/AgCl electrode were employed as auxiliary and reference electrodes, respectively.

2.2.4 Ligand Synthesis

Ligands synthesized in this work were prepared by the general route used in the formation of azomethine linkages. The synthetic approach towards azomethines is shown in Figure 2-3. Also presented in Figure 2-3 are the structures of precursor molecules **2-1, 2-2** as well as the structures of the prepared ligands, $\mathbf{L_{1\text{-}5}}$. The condensation reaction of an aldehyde and an amine in an alcoholic solution, catalyzed by acid, yields the azomethine ligands. The purification of the ligands is carried out by separation on a silica gel column using the volatile organic base triethylamine to protect the acid-sensitive azomethine linkage from hydrolysis.

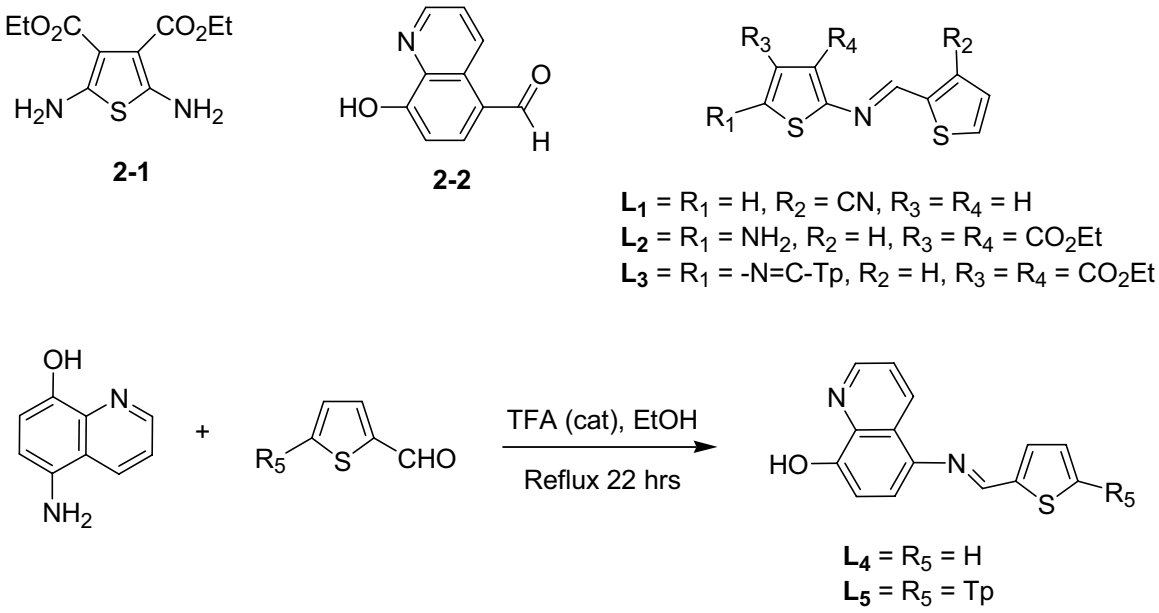

Figure 2-3. The general synthetic route for the preparation of ligands (shown at bottom) and the structures of all prepared ligands, $\mathbf{L_{1\text{-}5}}$.

2,5-Diamino-thiophene-3,4-dicarboxylic acid diethyl ester (2-1). The optimized procedure is based on similar reports.[30,33,53,78] In a round-bottomed flask (50 mL), Sulfur (1.04 g) and triethylamine (0.75 g , 1.03 mL) were stirred together in DMF (5 mL). After 30 minutes of stirring at room temperature, the solution turned a dark-red colour. Ethyl cyanoacetate (7.3 g, 6.9 mL) diluted in DMF (5 mL) was subsequently added dropwise over 30 min. The opaque solution was allowed to stir under ambient conditions for three days, after which the solvent was removed under vacuum, yielding a brown solid. The solid was loaded onto a silica gel column and eluted with using a solvent gradient starting with 100% hexanes and gradually increasing the polarity up to 35% ethyl acetate (EtOAc) yielding the title compound (0.96 g, 12%) as a gold powder. M.p.: 155 - 156 °C. ^{1}H NMR (400 MHz, [D] acetone-d_6); δ = 6.15 (s, 4H), 4.17 (q, 4H, ^{3}J = 7.1 Hz), 1.25 (t, 6H, ^{3}J = 7.1 Hz). ^{13}C NMR (100 MHz, [D] acetone-d_6): δ = 166.7, 151.3, 103.7, 61.0, 15.7. MS: *m/z* = 281.05649 $[M+H]^+$ (calculated 281.05665).

8-Hydroxy-quinoline-5-carbaldehyde (2-2). The aldehyde **2-2** was synthesized according to the literature procedure reported by Clemo and Howe.[79] In a two-necked round-bottomed flask (250 mL) was mixed 50 mL of a 15 % wt solution of NaOH in distilled water (8.3 g dissolved in 47.03 g of water), ethanol (25 mL), and 8-hydroxyquinoline (9.88 g). After dissolution of the 8-hydroxyquinoline, dichloromethane (11.4 g, 8 mL) was added dropwise with stirring over 45 minutes. The reaction mixture was refluxed overnight at which point the mixture was cooled to room temperature and acidified with dilute hydrochloric acid. The brown precipitate formed was filtered and dried under vacuum in the presence of P_2O_5 in a dessicator. The precipitate was then extracted for 48 hours using a Sohxlet extraction apparatus with petroleum ether as the solvent. The extracted crude product was then recrystallized from ethanol, then from a mixture of ethyl acetate and hexanes yielding 45.5 mg (0.5%) of the product as yellow spars. ^{1}H NMR (400MHz, [D] methanol-d_3); δ = 10.10 (s, 1H), 9.66 (d, 1H, ^3J = 8.6 Hz), 8.90 (d, 1H, ^3J = 2.9 Hz), 8.09 (d, 1H, ^3J = 8.0 Hz), 7.70 (dd, 1H, ^3J = 8.6 Hz, ^3J = 4.3 Hz), 7.24 (d, 1H, ^3J = 8.0 Hz), 4.87 (s, OH). ^{13}C NMR (100 MHz, [D] methanol-d_3): δ = 193.7, 161.1, 150.0, 141.9, 135.1, 128.5, 125.5, 124.3, 111.3, 101.0.

2-[(Thiophen-2-ylmethylene)-amino]-thiophene-3-carbonitrile (L_1). In a round-bottomed flask (50 mL) was added 2-thiophenecarboxaldehyde (1.47 g, 1.20 mL) dissolved in ethanol (30 mL), 2-amino-3-cyanothiophene (1.63 g) and a catalytic amount of trifluoroacetic acid (TFA). The mixture was refluxed overnight for 22 hours. Complete removal of the solvent afforded a viscous yellow oil which was purified by flash column chromatography (SiO_2, 10:90 EtOAc:Hexanes, 1% Et_3N) yielding the product as a yellow solid (57%). M.p.: 20 ºC. ^{1}H NMR (400MHz, [D] acetone-d_6); δ = 8.91 (s, 1H), 7.91 (d,

1H, ^{3}J = 5.0 Hz), 7.83 (dd, 1H, ^{3}J = 3.6 Hz, ^{4}J = 1.0 Hz), 7.42 (dt, H, ^{3}J = 7.0 Hz, ^{4}J = 1.8 Hz), 7.30-7.25 (m, 2H).

2-Amino-5-[(thiophen-2-ylmethylene)-amino]-thiophene-3,4-dicarboxylic acid diethyl ester (L_2). The optimized procedure is based on similar reports.[30,33] To an ethanolic solution of **2-1** (254 mg) was added 2-thiophenecarboxaldehyde (137 mg). The mixture was refluxed for 20 hours after the addition of a catalytic amount of trifluoroacetic acid (TFA). The solvent was removed, and the product was isolated (245 mg, 70%) as a yellow solid after purification by flash chromatography (SiO_2, 40:60 EtOAc:Hexanes, 1% Et_3N). M.p.: 114 - 116 °C. ^{1}H NMR (400MHz, [D] acetone-d_6): δ = 8.26 (s, 1H), 7.64 (d, 1H, ^{3}J = 5.0 Hz), 7.52 (d, 1H, ^{3}J = 3.2 Hz), 7.46 (broad, -NH_2), 7.14 (dd, 1H, ^{3}J = 5.2, ^{3}J = 4.0 Hz), 4.33 (q, 2H, ^{3}J = 7.1 Hz), 4.20 (q, 2H, ^{3}J = 7.1 Hz), 1.38 (t, 3H, ^{3}J = 7.1 Hz), 1.26 (t, 3H, ^{3}J = 7.1 Hz). ^{13}C NMR (100 MHz, [D] acetone-d_6): δ = 165.0, 164.3, 161.1, 161.0, 146.1, 143.2, 132.9, 132.0, 130.5, 128.4, 101.9, 61.0, 60.0, 14.3, 14.1. MS: *m/z* = 353.06251 $[M+H]^+$ (calculated 353.06242).

2,5-Bis-[(thiophen-2-ylmethylene)-amino]-thiophene-3,4-dicarboxylic acid diethyl ester (L_3). The optimized procedure is based on similar reports.[30,33] To an solution of **2-1** (209 mg) dissolved in anhydrous isopropanol (15 mL) was added 2-thiophenecarboxaldehyde (200 mg). The mixture was refluxed for 20 hours following the addition of a catalytic amount of trifluoroacetic acid. The solvent was removed, and the product was isolated as a dark red solid (240 mg, 67%) after purification by flash chromatography (SiO_2) starting with 100% hexanes and gradually increasing the polarity to 30% ethyl acetate and 70% hexanes. M.p.: 125 - 126 °C. ^{1}H NMR (400MHz, [D] acetone-d_6): δ = 8.75 (s, 2H), 7.85 (d, 2H, ^{3}J = 5.2), 7.76 (d, 2H, ^{3}J = 3.7), 7.26 (dd, 2H,

^{3}J = 5.2, 3.7), 4.31 (q, 4H, ^{3}J = 7.2), 1.36 (t, 6H, ^{3}J = 7.2). ^{13}C NMR (100 MHz, [D] acetone-d_6): δ = 163.0, 153.60, 149.2, 142.4, 135.1, 133.2, 128.9, 127.5, 61.2, 14.2. MS: *m/z* = 447.04921 $[M+H]^+$ (calculated 447.05015).

Synthesis of Ligands L_4 and L_5

Prior to use in the preparation of ligands **L_4** and **L_5**, the starting material 5-amino-8-hydroxyquinoline (5A8HQ) was both purified and deprotonated. The procedures for these work-ups are presented herein.

Purification of 5-amino-8-hydroxyquinoline dihydrochloride salt

The product obtained from Aldrich-Sigma was dissolved in MeOH and filtered to remove insolubilities. The solution was then treated with diethyl ether causing precipitation of the quinoline salt. The quinoline salt was recovered by filtration and stored prior to use in synthetic reactions.

5-[(Thiophen-2-ylmethylene)-amino]-quinolin-8-ol (L_4). In a round-bottomed flask (25 mL), 5-amino-8-hydroxyquinoline dihydrochloride salt (200 mg) was dissolved in dry methanol (5 mL). To this reddish-brown solution was added triethylamine (excess) such that the solution colour changed to yellow-orange. The solvent and excess triethylamine was removed under vacuum. The de-protonated 5-amino-8-hydroxyquinoline was then re-dissolved in anhydrous ethanol (15 mL). To this was added excess 2-thiophenecarboxaldehyde (1.22 g, 1.0 mL) and a catalytic amount of trifluoroacetic acid. The mixture was heated to reflux overnight, 24 hours, and the solvent removed. The product was purified by flash chromatography (SiO_2, 40:60

EtOAc:Hexanes as eluent, 1% Et_3N). The product was obtained as a yellow-brown solid (181 mg, 40.5 %). M.p.: 157 - 159 ºC. ^{1}H NMR (400MHz, [D] acetone-d_6): δ = 8.92 (s, 1H), 8.88 (dd, 1H, ^3J = 3.8 Hz, ^4J = 1.6 Hz), 8.81 (dd, 1H, ^3J = 8.5 Hz. ^4J = 1.6 Hz), 8.75 - 8.60 (broad, 1H, OH peak), 7.74 (dt, 1H, ^3J = 5.0 Hz, ^4J = 2.0 Hz), 7.68 (dd, 1H, ^3J = 3.7 Hz, ^4J = 0.9 Hz), 7.62 (m, 1H, ^3J = 4.4 Hz), 7.40 (d, 1H, ^3J = 8.2 Hz), 7.23 (m, 1H, ^3J = 4.3 Hz, ^4J = 1.4 Hz), 7.15 (d, 1H, ^3J = 8.1 Hz). ^{13}C NMR (100MHz [D] acetone-d_6): δ = 153.7, 153.4, 150.5, 145.5, 140.7, 140.1, 134.6, 134.4, 132.2, 129.9, 127.0, 123.7, 115.8, 111.8. MS: *m/*z = 255.11557 $[M + H]^+$ (calculated 255.11545).

6-(2-[2,2']Bithiophenyl-5-yl-vinyl)-quinolin-8-ol (L_5). In a round-bottomed flask (25 mL), 5-amino-8-hydroxyquinoline dihydrochloride salt (102 mg) was dissolved in dry methanol (5 mL). To this reddish-brown solution was added triethylamine (excess) such that the solution colour changed to yellowish orange. The solvent and excess triethylamine was removed under vacuum. The deprotonated 5-amino-8-hydroxyquinoline was then re-dissolved in anhydrous ethanol (15 mL). To this was added 2',5-bisthiophen-2-one (73 mg) and a catalytic amount of trifluoroacetic acid. The mixture was heated to reflux overnight, 24 hours, and the solvent removed. The product was purified by flash chromatography (SiO_2, 10:90 EtOAc:Hexanes as eluent, 1% Et_3N). The product was collected as a red powder (5 mg, 4%). M.p.: 193 - 195 ºC. ^{1}H NMR (400MHz, [D] acetone-d_6): δ = 8.91 (s, 1H), 8.90 - 8.85 (m, 2H), 7.66-7.62 (m, 2H), 7.55 (dd, 1H, ^3J = 5.1 Hz, ^4J = 1.0 Hz), 7.49 (dd, 1H, ^3J = 3.7 Hz, ^4J = 1.0 Hz), 7.45 (d, 1H, ^3J = 8.0 Hz), 7.39 (d, 1H, ^3J = 3.9 Hz), 7.16 (m, 2H, ^3J =4.0 Hz, ^4J = 1.4 Hz). ^{13}C NMR (100MHz [D] acetone-d_6): δ = 153.5, 153.1, 150.5, 144.2, 143.2, 140.5, 140.2, 138.6,

135.4, 134.6, 130.3, 128.1, 127.2, 127.0, 126.2, 123.7. 115.8, 111.8. MS: *m/z* = 337. 04640 $[M + H]^+$ (calculated 337.04638).

2.2.5 Metal Complex Synthesis

The metal complexes that were formed using the ligand **L_4** were prepared by a general procedure that makes use of the insolubility of the desired products in solvents like ethanol, methanol and water. Reactions using the ligands **L_{1-3}** were all unsuccessful as either no complexes were formed or the ligands decomposed. Ligand **L_5** was not used for forming metal complexes due to insufficient yields in its preparation.

Synthesis of complexes based on the ligands L_{1-3}

Solutions of the ligands **L_{1-3}** were prepared in either ethanol or methanol while solutions containing the silver (I) compounds $AgNO_3$ and AgOH were prepared in methanol, ethanol or water. Molar ratios for these reactions were set to 2:1 ligand:metal. No colour change was observed upon mixing of ligand and metal ion solutions and no precipitate was readily formed. To induce the metal-ligand reaction, these mixtures were heated to reflux over periods of 6-18 hours. After reflux, the solution colour had often changed to black, still with a lack of precipitate. TLC and NMR measurements on the resulting solutions confirmed that starting ligands had decomposed.

General procedure for metal complexation reactions with ligand L_4

A solution of ligand **L_4** (~ 30 mg) in anhydrous ethanol (5-10 mL) was prepared. Solutions containing metal ions, including Cd^{2+}, Co^{2+}, Cu^{2+}, Fe^{2+}, Mn^{2+}, Ni^{2+}, Pb^{2+}, Zn^{2+} and Ag^+, from various hydroxide, acetate, perchlorate and nitrate salts, were prepared by dissolving the appropriate metal salt in either water, ethanol, acetonitrile or some combination of the three to ensure complete dissolution of the salt. The ligand solution

was then added dropwise over 1-2 minutes until a visible precipitate was formed. The solutions were stirred at room temperature for two hours at which point the solutions were placed in a centrifuge for 20 minutes allowing the solid precipitate to sink to the bottom of the reaction vessel. The remaining liquid was decanted, and then the solid was dispersed in an organic solvent (ex. acetone, ethanol, etc.) to remove uncomplexed ligand. The product was then filtered and collected as a solid.

Bis(5-[(Thiophen-2-ylmethylene)-amino]-quinolin-8-ol) Copper(II)

To a solution of $Cu(OH)_2$ dissolved in ethanol (5.0 mg, 5 mL) was added a solution of **L_4** in ethanol (21.6 mg, 5.0 mL). The solid collected was dark orange/brown in colour, weighing 4.7 mg giving an approximate yield of 20 %.

Bis(5-[(Thiophen-2-ylmethylene)-amino]-quinolin-8-ol) Cobalt(II)

To a solution of $Co(OH)_2$ dissolved in acetonitrile (2.6 mg, 2 mL) was added a solution of **L_4** in acetonitrile (14.3 mg, 2 mL). The solid collected was dark orange/brown in colour, weighing 1.8 mg giving an approximate yield of 10 %.

Bis(5-[(Thiophen-2-ylmethylene)-amino]-quinolin-8-ol) Zinc(II)

To a solution of $Zn(OH)_2$ dissolved in ethanol (3.4 mg, 3 mL) was added a solution of **L_4** in ethanol (17.4 mg, 3 mL). The solid collected was bright yellow in colour, weighing 1.9 mg giving an approximate yield of 15 %.

Bis(5-[(Thiophen-2-ylmethylene)-amino]-quinolin-8-ol) Iron(II)

To a solution of $Fe(ClO_4)_2$ dissolved in ethanol (13.6 mg, 5 mL) was added a solution of **L_4** in ethanol (29.7 mg, 5 mL). The solid collected was black in colour, weighing 9.7 mg giving an approximate yield of 32 %.

Bis(5-[(Thiophen-2-ylmethylene)-amino]-quinolin-8-ol) Manganese(II)

To a solution of $Mn(OAc)_2$ dissolved in 50:50 water:ethanol (13.5 mg, 5 mL) was added a solution of **L_4** in ethanol (35.1 mg, 10 mL). The solid collected was yellow-orange in colour, weighing 15.6 mg giving an approximate yield of 35 %.

Bis(5-[(Thiophen-2-ylmethylene)-amino]-quinolin-8-ol) Nickel (II)

To a solution of $Ni(NO_3)_2$ dissolved in 50:50 water:ethanol (22.6 mg, 5 mL) was added a solution of **L_4** in ethanol (37.6 mg, 10 mL). The reaction mixture turned black overnight, no product was formed and the reaction was deemed unsuccessful.

Bis(5-[(Thiophen-2-ylmethylene)-amino]-quinolin-8-ol) Lead (II)

To a solution of $Pb(OAc)_2$ dissolved in water (38.2 mg, 2 mL) was added a solution of **L_4** in ethanol (50.7 mg, 11 mL). The solid collected was yellow-orange in colour, weighing 28.4 mg giving an approximate yield of 40 %.

Bis(5-[(Thiophen-2-ylmethylene)-amino]-quinolin-8-ol) Cadmium (II)

To a solution of $Cd(OAc)_2$ dissolved in water (14.3 mg, 3 mL) was added a solution of **L_4** in ethanol (30.4 mg, 6 mL). The solid collected was yellow in colour, weighing 3.5 mg giving an approximate yield of 10 %.

2.3 Results and Discussions

2.3.1 Metal Complex Synthesis

The development of ligand molecules for this work is centered on the facile synthesis of azomethine ligands. In total, two novel ligands were synthesized for this work and three previously reported ligands were used for metal complexation. Of the five ligands prepared, only one ligand, $\mathbf{L_4}$, was successfully used to form metal complexes. ^{1}H NMR and ^{13}C NMR spectra of the five ligands synthesized are presented in appendix B.

Metal complexes of the form $\mathbf{ML_2}$ were synthesized via a very straightforward approach. The reactions that were intended to form the complexes $\mathbf{M(L_{1\text{-}3})_2}$ were unsuccessful. This can be confirmed by the lack of precipitate formation in the reaction mixture, ligand decomposition from NMR and TLC experiments and the colour change from red-yellow solutions to very dark colours (often black).

In all but two attempts, the metal used for the $\mathbf{M(L_{1\text{-}3})_2}$ reactions was silver. This became an important factor in determining that the reactions were unsuccessful. As the ligand was decomposed, the silver in the metal salt was reduced to its elemental form. This was confirmed by the deposition of a thin film of elemental silver on the interior of the reaction flask. The coating was only removed by the action of strong acid giving another indication that the residue was metallic silver.

The complexes $\mathbf{M(L_4)_2}$ were successfully synthesized by mixing two equivalents of a solution of the ligand dissolved in ethanol and with one equivalent of the corresponding metal ion solution dissolved in either ethanol, water or a mixture of the two. Upon mixing the two solutions, a strongly coloured insolublility was formed and filtered. The resultant complexes were insoluble in common organic solvents like

acetone, ethanol and dichloromethane but demonstrated low solubility in solvents like DMF and DMSO.

2.3.2 Structural Characterization

Structural characterization of the resultant metal complexes was difficult due to their low solubility. ^{1}H NMR measurements were carried out on a number of the complexes dissolved in DMSO, but these results were largely inconclusive. The NMR spectrum of **Pb(L_4)$_2$**, shown in Figure 2-4, indicates the presence of an azomethine functionality as a result of the peaks centered at 8.8 ppm which correspond to the region in which azomethine protons are most commonly observed.

The structure of the dissolved product cannot be confirmed with certainty from the NMR result shown in Figure 2-4. This spectrum was among the best recorded for metal complexes of the type **M(L_4)$_2$** yet its results are effectively inconclusive. The integrals calculated for the peaks in Figure 2-4 indicate that the number of aromatic protons present may be the same as that of the free ligand. In both the free ligand and the metal complex, nine aromatic protons should be observed. Indeed this is the case observed in Figure 2-5, which shows the ^{1}H NMR spectrum of the free ligand, **L_4**, The three protons in the 8.7 - 9.0 ppm range correspond to the azomethine proton as well as the protons *ortho*- to the nitrogen of the pyridine ring and *ortho*- to the 8-hydroxyl group.

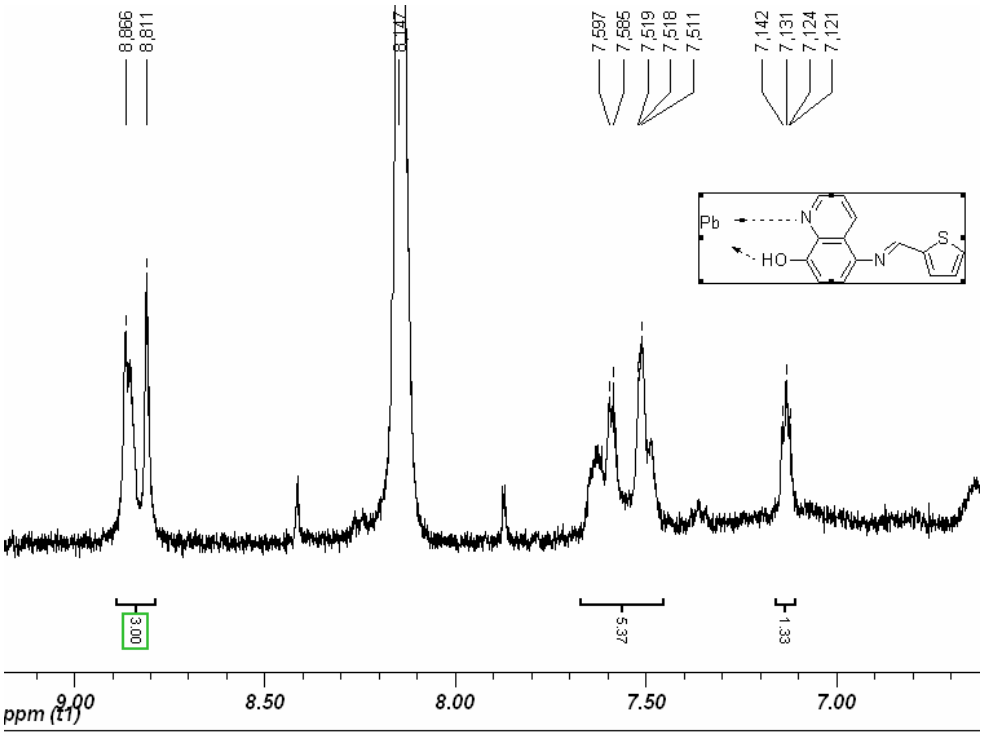

Figure 2-4. [1]H NMR spectrum of the metal complex of **$Pb(L_4)_2$** in deuterated dimethylsulfoxide.

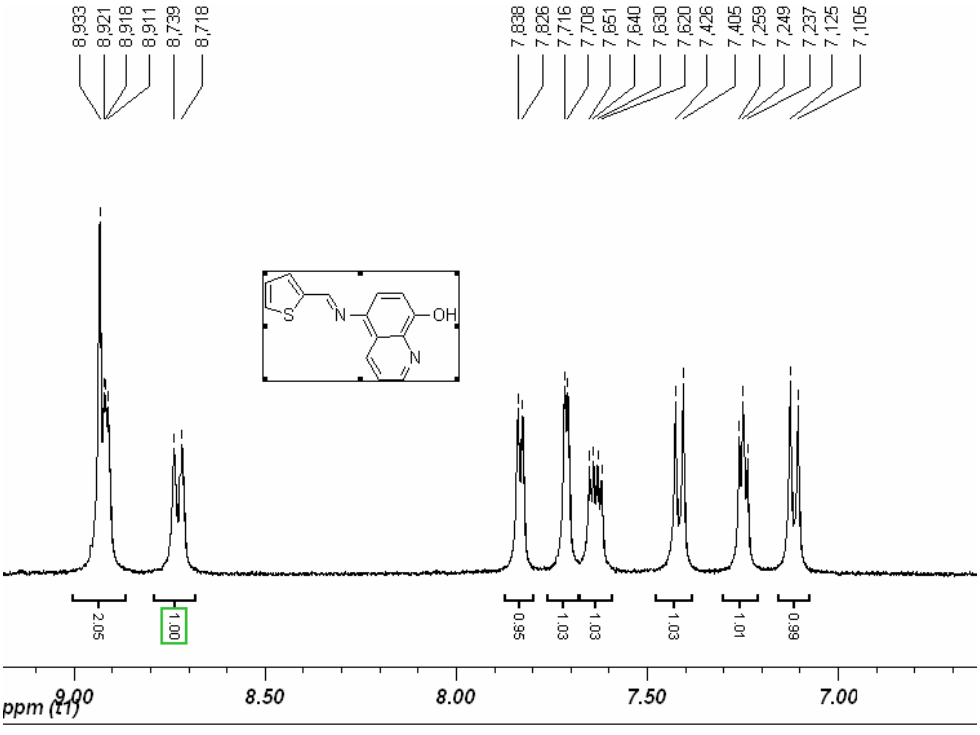

Figure 2-5. [1]H NMR spectrum of the ligand **L_4** in deuterated dimethylsulfoxide.

In the metal complex spectrum of Figure 2-4, it appears that the three protons observed between 8.7 – 9.0 ppm have become more closely spaced. This is in agreement with the expected structure of the complexes. The 8-hydroxyl and pyridine-nitrogen moieties are more likely to interact with a metal centre than the azomethine-thiophene unit on the other end of the molecule. As complexation occurs, electron density from the nitrogen and oxygen atoms is used to bond with the metal centre which causes further deshielding of the downfield protons previously observed at 8.9 and 8.7 ppm. This pushes the two protons closer to the azomethine proton observed in both spectra at 8.9 ppm.

The rest of the aromatic protons are no longer distinct peaks as observed with the free ligand. Due to this it is difficult to use the integral values to accurately determine the relative number of protons present in the metal complex. The peaks located near 8.9 ppm in Figure 2-4 were used as the reference peaks for determining the relative number of protons observed in the other peaks. Based on the structure of the spectrum in Figure 2-4 as well as the spectrum of the free ligand shown in Figure 2-5 it appears that three aromatic protons are present around 8.9 ppm. For this reason, those peaks were set to an integration of 3.0. The integral calculated for the bunch of peaks at 7.4 - 7.7 ppm is slightly more than 5.3. The other peak at 7.12 ppm integrates for 1.3 protons. This yields the correct sum of 9 protons when the values of 5.3 and 1.3 are rounded down.

Unfortunately, the ^{1}H NMR spectrum lacks the required clarity and precision needed to confirm the structure of the product with a high degree of confidence. ^{13}C NMR experiments were attempted but the very low solubility of the complexes made it impossible to detect any products even with a long analysis time (16 hours, overnight).

Furthermore, as solvent evaporated and the temperature decreased within the NMR instrument, much of the dissolved product precipitated from solution.

The combination of these confounding factors made it difficult to confidently confirm the structure of the formed products. In spite of this, the fact that the protons observed in Figure 2-4 for the lead complex are found in a region that is similar to the free ligand, yet displaced by reasonable amounts based on the change in the chemical environment leads to the presumption that in fact a metal complex was formed. The protons in the region of the most effective chelation site are displaced through a downfield shift, consistent with the removal of electron density, and the peak integrations are very close to what would be expected for the ligand $\mathbf{L_4}$. Despite the positive correlations between the proton spectrum measured and the spectrum of the free ligand, it is impossible to confirm the structure of the metal complexes from the data available.

In light if the difficulties encountered in the course of NMR analysis, further structural characterization was attempted by means of single crystal X-ray diffraction and by electrospray ionization mass spectrometry (ESI-MS). Neither of these two techniques was useful in the elucidation of the exact structure of the metal complexes. However, the ESI-MS results provided further indirect evidence indicating the formation of metal complexes.

The preparation of X-ray quality crystals was attempted by dissolving the complexes in DMF and DMSO. After one month on the bench, the solutions had lost only minimal solvent and no precipitation was observed. Precipitation induced by the introduction of a secondary solvent, e.g. acetone and ethanol, was rapid and produced only powders. These materials were not useful in the production of single crystals.

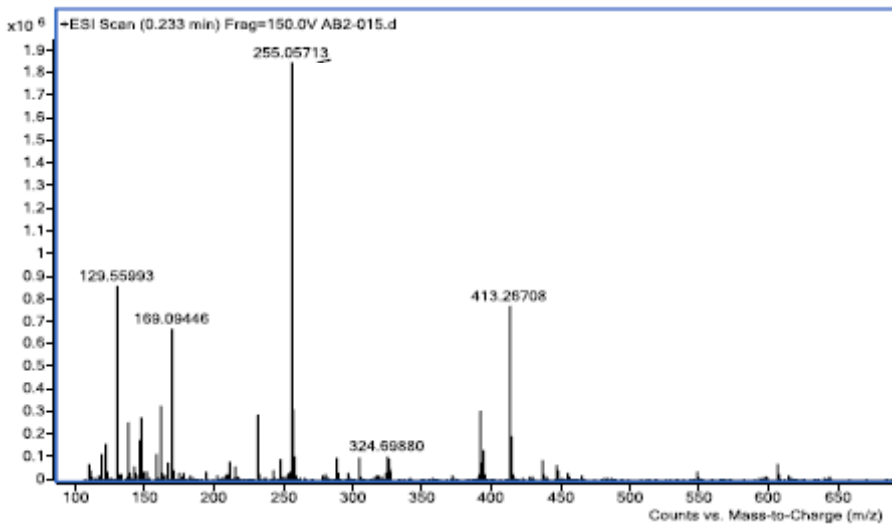

Figure 2-6. ESI mass spectrum of the lead complex of $\mathbf{L_4}$ recorded from DMSO solution.

Mass spectrometry analysis was also attempted with DMSO solutions of the metal complexes. This presented the issue of volatilizing not only the solvent (DMF and DMSO are not recommended for ESI-MS), but also in volatilizing the complex. Results from these analyses confirmed the presence of free ligand which is likely produced from the decomposition of a metal complex under the abrasive conditions of the ionization source.

Shown in Figure 2-6 is an ESI-MS spectrum of the lead complex. The sample was prepared in DMSO which is not a particularly good solvent for ESI. The free ligand $\mathbf{L_4}$ is clearly observed in the spectrum as the major contributor in the sample. The likely reason for this is decomposition of the complex either upon volatilization or ionization. In any case, the presence of free ligand is very useful in inferring the formation of a metal complex. If the dried powder contained free ligand, washing of the complex with a solvent like dichloromethane or chloroform would cause the dissolution of the ligand. However, after numerous washes with common organic solvents, no ligand was observed in subsequent washes indicating that ligand produced within the mass spectrometer is in fact coming from a decomposing complex. The result of Figure 2-6 is repeated in the

mass spectrum of the copper complex shown in Figure 2-7. Again, free ligand is observed while the expected product is not.

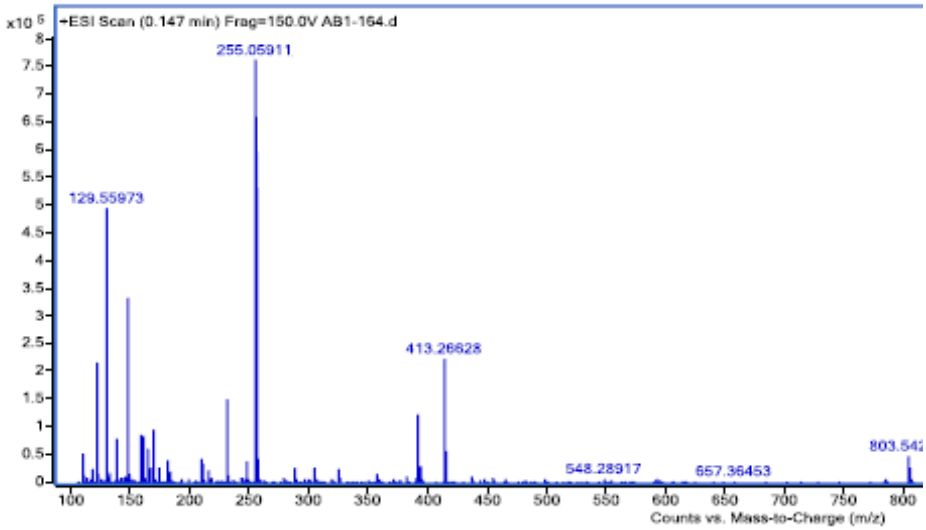

Figure 2-7. ESI mass spectrum of the copper complex of $\mathbf{L_4}$ recorded from DMSO solution.

To summarize, it is not possible to positively confirm the formation of metal complexes from the data presented here. However, based on the NMR results which seem to indicate a change in chemistry in the region of the pyridine nitrogen and the hydroxyl group, it seems reasonable that a metal complex containing the ligand $\mathbf{L_4}$ has been formed. The mass spectrometry results indicate that the ligand is present in the isolated powders, but that the complex formed may not be stable to strong ionization sources. Furthermore, the strong colours of the isolated powders concomitant with the insolubility of the powders in common solvents like DCM, chloroform and acetone give credence to the supposition that in fact new metal complexes have been formed. While it is impossible to describe the stoichiometry of the complexes, it is possible to infer that metal complexes have been formed based on the indirect evidence provided in this section.

2.3.3 Spectroscopic Properties

The most effective method to observe a change in chemistry in the ligands is the use of UV-vis absorption and fluorescence spectroscopy. The formation of a new metal complex should significantly effect the location and intensity of the absorption and emission maxima upon metal complexation. The observation of a change in fluorescence quantum yield was also foreseen; however experimental difficulties precluded its exact determination.

As previously mentioned, the low solubility of the metal complexes in common organic solvents like ethanol, acetonitrile and water forced the use of DMF as the solvent for UV-vis spectroscopic analysis. Due to this, it was impossible to observe changes in the UV-vis spectrum below 300 nm, where the absorbance maximum of the free ligand, **L**$_4$, was observed in solvents like ethanol and acetonitrile.

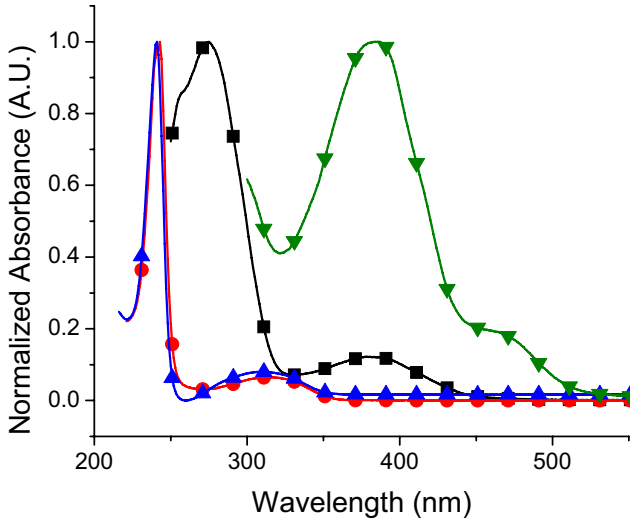

Figure 2-8. Solvatochromism of ligand **L**$_4$. Measurements were made in dichloromethane (■), ethanol (●), acetonitrile (▲) and dimethylformamide (▼).

Figure 2-8 demonstrates the solvatochromism of the free ligand, **L**$_4$. The absorbance spectra in ethanol and acetonitrile are nearly identical while moving to

solvents like dichloromethane and DMF induce a bathochromic shift in the absorbance maxima. The maximum in the DMF spectrum appears to be in the same location as the small absorption peak in the dichloromethane spectrum. This indicates that the global maximum of the DMF spectrum is in fact below 300 nm as was observed for the global maximum in the DCM spectrum. Wavelengths shorter than 300 nm are fully absorbed by DMF so the absorbance maximum of the ligand is most likely hidden by the solvent. For this reason, changes in the absorbance band at 386 nm are used for determining if complexation has occurred.

Upon complexation, significant changes in the absorbance spectra are observed. Figure 2-9 shows the changes in absorbance between free ligand and metal complexes, with measurements made in DMF. In general, a bathochromic shift of the absorption maximum is observed when the ligand is mixed with Cu^{2+}, Pb^{2+} and Mn^{2+}. The bathochromic shifts of the absorption maximum for the complexes compared to that of the free ligand are 78 nm, 65 nm and 65 nm for the copper, lead and manganese complexes, respectively.

The Fe^{2+} complex shown in Figure 2-9 demonstrates a significant change in the structure of the absorbance spectrum indicating that the complex may not contain the ligand $\mathbf{L_4}$. This is corroborated by the fact that the solid powder itself is black, indicating that the ligand actually decomposed. This is further supported by the fact that all other powders obtained were coloured; yellow, orange or brown. The bathochromic shift of the absorption maximum when compared to the free ligand is also much smaller, only 28 nm.

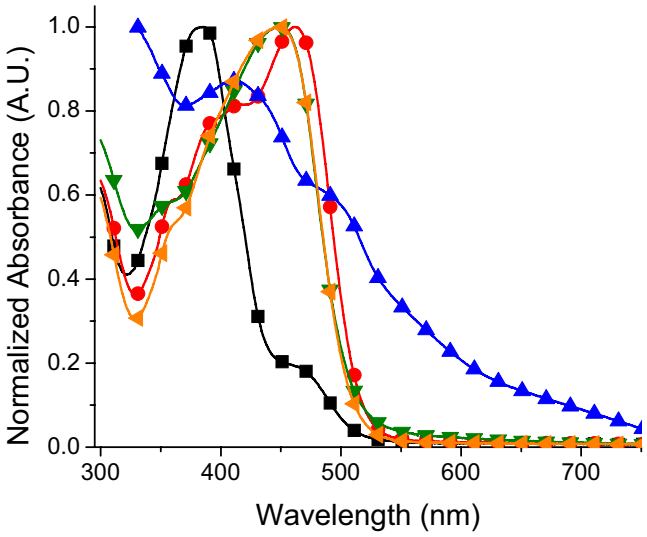

Figure 2-9. A comparison of the absorption spectra of the free ligand $\mathbf{L_4}$ (■) and its corresponding copper (●), iron (▲), manganese (▼) and lead (◀) complexes.

Fluorescence spectroscopy was also used to observe the change in physical properties occurring with ligand complexation. As with the absorbance measurements, the photoluminescence studies were carried out in DMF. Fluorescence measurements of the free ligand, $\mathbf{L_4}$, and its metal complexes are shown in Figure 2-10. Excitation of the ligand is made at the absorbance maximum, 386 nm. All of the complexes studied using excitations at 386 nm demonstrated a spectral structure that is nearly identical to the fluorescence spectrum of the free ligand with a slight bathochromic shift of the maximum in all cases, except for the iron complex. The bathochromic shifts for the copper, manganese and lead complexes were 25 nm, 32 nm and 15 nm, respectively. The displacement of the luminescence maxima is therefore significantly smaller than the displacement of the absorbance maxima.

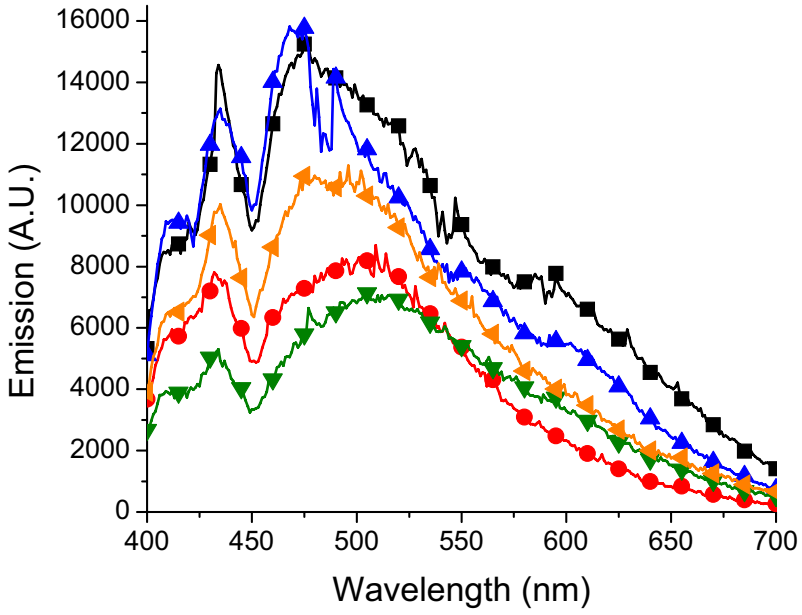

Figure 2-10. A comparison of the fluorescence spectra of the free ligand $\mathbf{L_4}$ (■) and its corresponding copper (●), iron (▲), manganese (▼) and lead (◀) complexes.

The quantum yields of fluorescence of the ligands $\mathbf{L_4}$ and $\mathbf{L_5}$ were also measured. The quantum yields were measured in ethanol using bithiophene as a reference. The values were determined to be 3.4 * 10^{-3} and 2.0 * 10^{-3}, for ligands $\mathbf{L_4}$ and $\mathbf{L_5}$, respectively. Ligands $\mathbf{L_{1\text{-}3}}$ were previously analyzed and their quantum yields were also determined to be on the order of 10^{-3}.[30]

Unfortunately, the quantum yields of the metal complexes could not accurately determined due to issues with solubility. In spite of this, the photoluminescence measurements shown in Figure 2-10 can be used to qualitatively describe the fluorescence quantum yields of the complexes. The free ligand $\mathbf{L_4}$ and its corresponding complexes were excited at 386 nm where the absorption maximum of the free ligand is observed in DMF solutions. The absorbances of the complexes were between 0.25 and 0.35 at 386 nm. The spectra presented in Figure 2-10 are the experimentally observed

fluorescence spectra without corrections. It is apparent from Figure 2-10 that the amount of luminescence observed for the complexes does not vary significantly from that of the free ligand, and in most cases is less intense. While the exact values cannot be reported, the metal complexes demonstrate quantum yields on the order of 10^{-3}, which is in the same range as ligands **L$_4$** and **L$_5$** as well as the previously reported ligands **L$_{1-3}$**.[30]

The intersection of the normalized absorbance and photoluminescence spectra give a good indication of the energy gap separating the ground state and the singlet excited state value for each complex. An example of this type of plot is given in Figure 2-11, which shows the spectral overlap for the ligand and the lead complex. The values determined for the four metals complexes are given below in Table 2-1. The intersection values, denoted by $\lambda_{A\text{-}F}$ in Table 2-1, give the lower estimate of the energy gap.

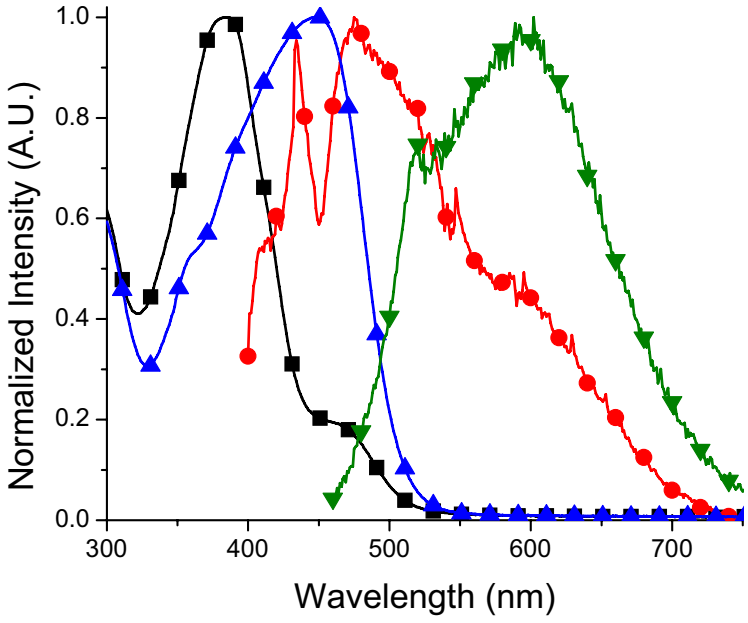

Figure 2-11. The crossover of the normalized absorbance and fluorescence scans of the free ligand **L$_4$** (■ and ●) and its corresponding lead complex (▲ and ▼).

Table 2-1. A summary of the photophysical data for ligand **L_4** and its corresponding metal complexes. Data listed here were recorded in dimethylformamide solutions.

Compound	λ_{max} (nm)	$\lambda_{Shoulder}$ (nm)	λ_{fluo} (nm)	λ_{A-F} (nm)	ΔE (eV)
Ligand, **L_4**	383	472	475, 590	416	2.97
$Cu(L_4)_2$	461	405	532	491	2.52
$Fe(L_4)_2$	413	500	496 (broad)	460	2.69
$Mn(L_4)_2$	448	350	514, 570 (sh)	487	2.54
$Pb(L_4)_2$	448	360	596	494	2.50

2.3.4 Metal Ion Sensing Devices

An objective of this work was to show that the ligands prepared could serve as metal ion sensors for water solutions. To this end, crude metal ion sensing devices were designed. A thin layer of the ligand **L_4** was spin cast from DCM solution, at a concentration of 2 mg per 5 mL, onto a glass slide, then immersed in a water solution containing 0.1 M $Cu(OTf)_2$. The immersed slide was then placed in an ultrasonic bath for 30 minutes to increase the speed of complexation.

Complex formation on the surface of the glass slide was followed by UV-vis absorbance spectroscopy. Figure 2-12 demonstrates the results of these measurements. After immersion in the metal ion solution, a new peak corresponding to the copper complex evolves around 475 nm, well above the 402 nm maximum observed for the free ligand on the glass slide. While very crude in design, these results give a preliminary indication that this ligand could be used in metal-sensing devices.

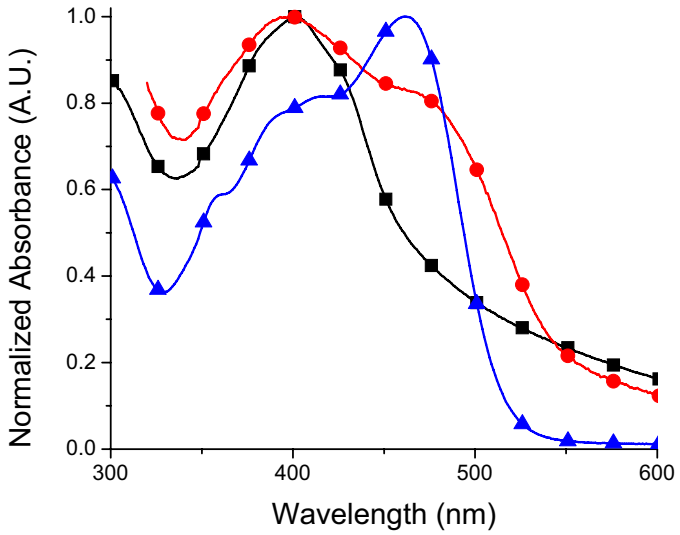

Figure 2-12. Changes in absorbance spectra of ligand $\mathbf{L_4}$ immobilized on a glass slide before (■) and after (●) treatment with a copper (II) solution. The other curve (▲) demonstrates the absorption of the copper complex in DMF solution.

2.4 Conclusions and Future Work

The hydroxyquinoline type ligand synthesized in this work, $\mathbf{L_4}$, serves as a suitable starting place for the study of the photophysical properties metal complexes containing both thiophene moieties and azomethine linkages. In spite of the difficulties associated with accurately determining the structures of the formed complexes, indirect evidence for their formation was used to determine that indeed complexes have been formed. Significant bathochromic shifts were observed in the absorbance spectra, with smaller shifts occurring in the fluorescence spectra. Ligands $\mathbf{L_{1\text{-}3}}$ did not produce the desired metal complexes and this remains a point of focus for this laboratory in future work.

From quantitative luminescence quantum yield data for the ligands $\mathbf{L_4}$ and $\mathbf{L_5}$, in conjunction with previously reported data on the ligands $\mathbf{L_{1\text{-}3}}$, it is clear that the azomethine bond strongly deactivates singlet excited state through non-radiative methods. This is based on the observation that the five ligands studied in this work have fluorescence quantum yields on the order of 10^{-3}. The qualitative Φ_{fl} values observed for the metal complexes of $\mathbf{L_4}$, also on the order of 10^{-3}, give a strong indication that the excited states of these molecules do not make use of internal conversion processes as a main method of excited state deactivation.

Enhanced structural rigidity caused by metal complexation should decrease the effect of internal conversion excited decay processes as the internal conversion pathways of bond rotation and vibrational are significantly dampened. In this way, restricted deactivation through internal conversion pathways should cause a subsequent increase in radiative deactivation in the form of fluorescence. Since the observed change in fluorescence upon metal complexation of $\mathbf{L_4}$ is small, the excited state must not be deactivated by internal conversion processes to any large extent and another form of excited state deactivation must be the major contributor. This is in good agreement with results reported in this work (*vide supra*, Chapter 1) as well as previous reports on the excited state decay mechanisms observed in azomethines which demonstrate that azomethines are non-fluorescent and are mainly deactivated through photoinduced electron transfer processes (intramolecular) as well as by intersystem crossing to the triplet state.

As a secondary goal of this work, a metal ion sensing device was prepared using the ligand $\mathbf{L_4}$ and was shown to have an affinity for copper ions in solution. The sample

of **L_4** spin cast onto glass demonstrated a change in absorbance when exposed to a water solution containing Cu^{2+} ions. The ligand showed resistance to water even after being immersed for 30 minutes which is of great concern for all azomethine containing molecules. While the device was crude in design, it succeeding in demonstrating the desired result: a water-stable slide that can test for the presence of metal ions in water solutions.

The work presented here is of importance in the elucidation of the excited state decay mechanics of azomethines. The small change in fluorescence upon complexation indicates that not only is fluorescence a negligible decay route but also that internal conversion processes have only a small role in excited state decay. This is of great value as the other non-radiative methods of excited state decay can be studied in greater detail.

Further work in this area will center on the use of ligands **L_{1-3}** in the formation of novel metal complexes. The study of their decomposition when exposed to certain metal ions, namely Ag^{+}, can provide useful information about the electrochemistry of these ligands. Also, the continued studied of ligands such as **L_4** and **L_5** will provide useful information about the excited state decay processes in thiophene azomethines. The application of analytical techniques will be very important in defining the solid state structures of formed metal complexes as it was apparent in this work that conventional NMR and MS techniques are not sufficient to positively confirm complex structure.

Chapter 3: Unsuccessful Syntheses

3.1 Background

In working towards new types of sterically hindered thiophene azomethines, such as those presented in chapter 1, various synthetic strategies were employed. Many of these reactions were not fruitful. These reactions as well as the objectives behind them will be discussed in this chapter.

In the first chapter of this work, a set of sterically hindered thiophene azomethine dyads was presented. These dyads were prepared through conventional azomethine preparation methods including acid-catalysed condensation in alcoholic solution, reaction with $TiCl_4$ as well as a few attempts on larger scales by applying an azeotropic distillation with a Dean-Stark trap. In general, the preparations of these products proceeded readily when steric hindrance in the region of the thiophene carbonyl was small. This was not the case when condensing the reagent 2,4,6-tri-*tert*-butylaniline with the methyl and ethyl ketones of 2-thiophenecarboxaldehyde.

The synthesis of dyads based on the aforementioned 2,4,6-tri-*tert*-butylaniline proved challenging as it took upwards of ten different reaction conditions to prepare the dyad **1-3** using 2-thiophenecarboxaldehyde. The dyads composed of 2,4,6-tri-*tert*-butylaniline condensed with the methyl and ethyl ketones of 2-thiophenecarboxaldehyde were also sought after, however, the desired products were not detected in any of the reactions attempted.

Once it was determined that the synthesis of these sterically hindered products would not be possible using the methods described above, it was decided that the bulky groups should be placed on the thiophene ring instead of the aniline ring. This could help to reduce the steric hindrance around the reaction centre. The nitrogen atom in 2,4,6-tri-

tert-butylaniline is surrounded by the large *tert*-butyl groups which makes it difficult for the amine to carry out nucleophilic attack at the carbonyl carbon. To this end, its was decided that new synthetic approaches would be examined with the goal of attaching *tert*-butyl groups directly to the thiophene ring, as well as to the carbonyl carbon used in azomethine formation.

Attachment of bulky groups directly to the thiophene ring would present the opportunity to observe how the bond rotation barriers vary with location of the bulky substituents. The addition of *tert*-butyl to the carbonyl carbon also presents an interesting opportunity. Since it was difficult to add a very bulky amine to the unsubstituted carbonyl it should also be difficult to add a small amine to a strongly sterically hindered carbonyl group. Reaction of the sterically hindered ketone with small amines such as n-propyl amine should give a clear indication as to the amount of steric hindrance around the reaction centre.

As mentioned above, the dyads previously discussed in this work contain the bulky *tert*-butyl groups only on the aniline moiety. To complete the series of sterically hindered dimers, bulky groups must be added to the thiophene ring. To this end, *tert*-butylated thiophene aldehydes and ketones were sought after. Multiple synthetic strategies were employed to arrive at these products. While some preparations were successful, namely the synthesis of a thiophene-diketone with *tert*-butyl groups attached to the carbonyl carbons, many of the synthetic strategies employed were ineffective for affording the desired products.

3.2 Synthetic Approaches

The first synthetic route discussed in this section uses bromopinacolone as a starting material. While bromopinacolone is available for purchase, it is rather expensive. For this reason, it was decided that bromopinacolone should be synthesized in-house. Various synthetic procedures for this bromination reaction are reported in the literature with varying degrees of success.[80,81,82] Two brominating agents were prepared for the synthesis of bromopinacolone. Although the brominating agents were synthesized in high yield, the subsequent preparations of bromopinacolone did not yield the desired product. As a result, bromopinacolone used in later syntheses, was purchased from a commercial supplier.

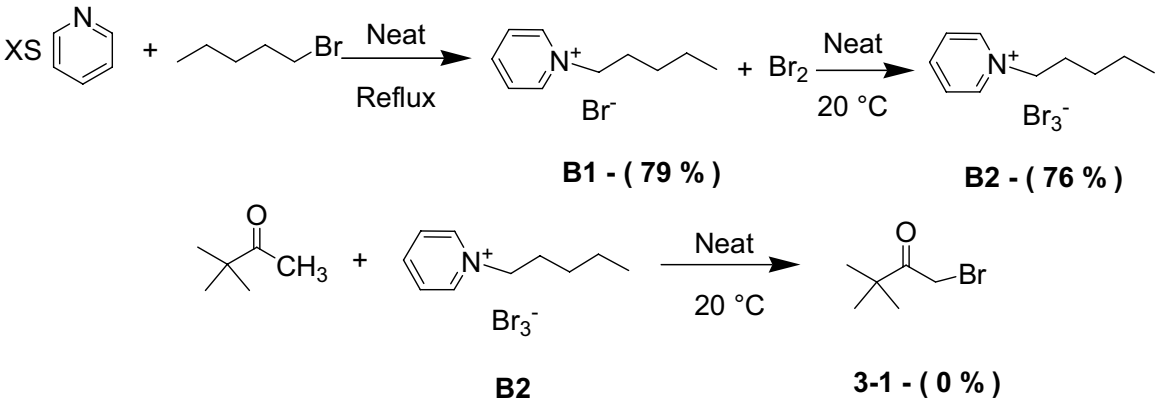

Figure 3-1. Synthesis of brominating agents **B1** and **B2** and synthesis of bromopinacolone **3-1**.

The first brominating agent used was an ionic liquid composed of the cationic N-pentylpyridinium ion and the monoanionic tribromide ion (Br_3^-).[82] It is prepared first from the reaction of pyridine with 1-bromopentane,[83] followed by further bromination of the resulting ionic liquid with liquid bromine.[82] The brominating agent, N-pentylpyridinium tribromide (**B2**), was then reacted with pinacolone. This reaction was

unsuccessful as no bromopinacolone was detected in the reaction mixture. This synthetic procedure is shown in Figure 3-1.

To continue towards bromopinacolone **(3-1)**, a second brominating agent was prepared. The second brominating agent, tetrabuylammonium tribromide **B3**, was synthesized from tetrabutylammonium bromide and hydrobromic acid.[81] The synthetic route is demonstrated in Figure 3-2. Once again, the brominating agent was synthesized in high yield; however the subsequent bromination of pinacolone was unsuccessful.

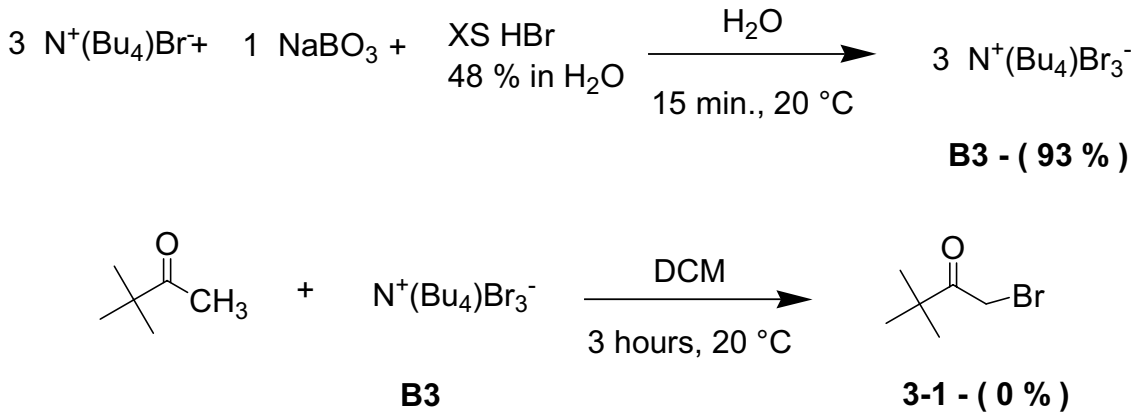

Figure 3-2. Synthesis of brominating agent **B3** and synthesis of bromopinacolone **3-1**.

The bromination reactions did not yield the desired bromopinacolone as suggested from the literature.[81,82] This can be attributed to two factors. The first is that bromopinacolone is volatile and may have evaporated while attempting to purify the reaction mixture. The second reason is that bromopinacolone is unstable under ambient conditions and may have decomposed prior to or during the work-up. These problems were not realized until after a few attempts of synthesizing bromopinacolone. Due to the synthetic difficulties encountered while preparing bromopinacolone, commercially available bromopinacolone was used in subsequent reactions.

The preparation of *tert*-butylated thiophenes was attempted using commercial bromopinacolone as a starting point. Reaction of bromopinacolone **3-1** with sodium sulfide produces the important diketosulfide intermediate **3-2** which can be isolated. From this diketosulfide intermediate, various approaches were investigated for forming an alkylated thiophene with a large degree of steric hindrance.

The first approach examined was the addition of *tert*-butyl functionalities in the 3- and 4-positions of a thiophene ring.[84] Formylation of the resultant 3,4-di-tert-butylthiophene **3-3** would then produce the desired *tert*-butylated thiophene aldehyde. The first step involves the addition of bromopinacolone, **3-1**, to a solution of disodium sulfide (as Na_2S-$9H_2O$) which produced the diketosulfide **3-2** in high yield. This molecule was then reacted with elemental zinc and $TiCl_4$ for thiophene ring formation with the ultimate product being 3,4-di-*tert*-butylthiophene **3-3**. Unfortunately, the desired substituted thiophene was not detected in the reaction mixture after work up. The synthetic route is demonstrated in Figure 3-3.

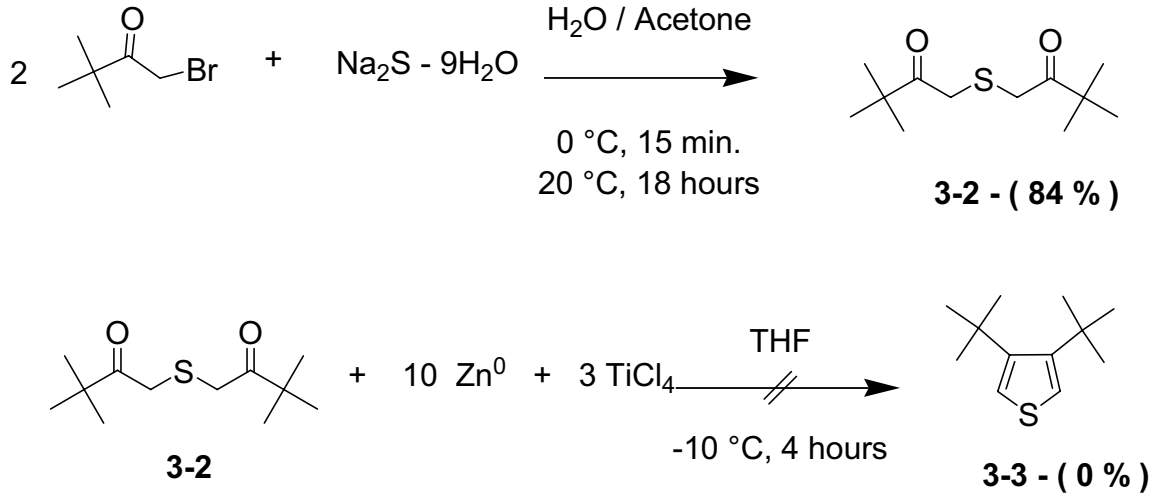

Figure 3-3. Synthesis of diketosulfide **3-2** and subsequent ring-closing reaction to form 3,4-di-*tert*-butylthiophene **3-3**.

It must be noted at this point that a side-product of this reaction was tremendously pungent. This reaction, if repeated in the future, must be done with extreme caution as the unidentified side product left a very foul odour in the synthetic laboratory for nearly a week. This side product, along with the fact that the reaction did not yield the desired product, influenced the use of a different synthetic methodology.

In continuing towards 3,4-di-*tert*-butylthiophene, a Grignard reaction between 3,4-dibromothiophene and *tert*-butylchloride was envisioned. 3,4-Dibromothiophene is readily available commercially, so the reaction was attempted by producing the Grignard reagent *tert*-butylmagnesium chloride from magnesium chloride, elemental potassium and *tert*-butylchloride.[85] This procedure is shown schematically in Figure 3-4. As mentioned before, the product obtained would subsequently be formylated yielding 3,4-di-*tert*-butyl-2-thiophenecarboxaldehyde and potentially the 2,5-dialdehyde. The formation of the Grignard reagent was visually confirmed through the dissolution of magnesium chloride and the production of a thick grey solution which was added to a solution of 3,4-dibromothiophene. Unfortunately, the desired product **3-3** was not observed in the reaction therefore a new synthetic route was considered.

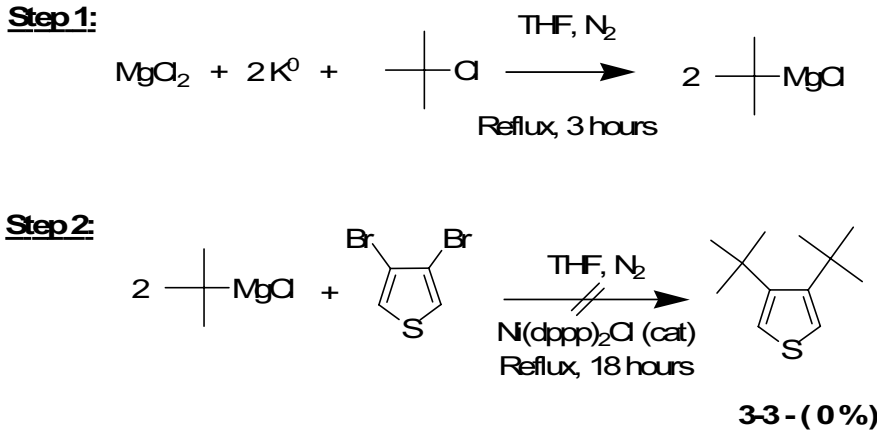

Figure 3-4. Synthesis of 3,4-di-*tert*-butylthiophene **3-3** using the Grignard reagent tert-butyl magnesium chloride.

The Grignard method of producing the 3,4-di-*tert*-butylthiophene **3-3** proved unsuccessful after two attempts, so a second procedure using the readily available diketosulfide **3-2**, was attempted. In this synthetic approach, glyoxal trimer dihydrate is reacted with the previously synthesized *tert*-butylated diketosulfide **3-2**.[86] The product of this reaction is a thiophene-diketone, with the ketones in the 2- and 5-positions being substituted with *tert*-butyl groups. The synthetic procedure starting from the diketosulfide **3-2** is shown in Figure 3-5. This reaction was designed to form the thiophene ring, while at the same time maintaining the *tert*-butylated ketone functionality. This reaction proceeded readily in fair yield (42 %).

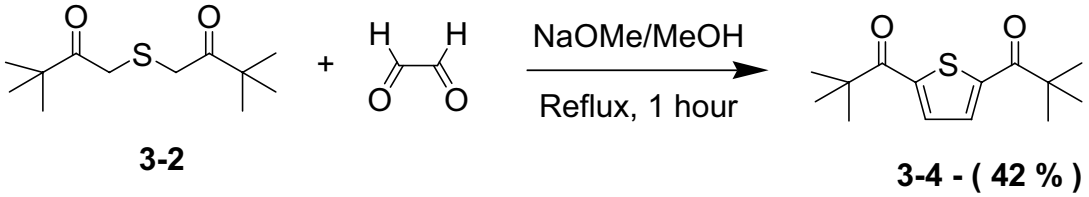

Figure 3-5. Synthesis of 2,5-thiophene-(di-*tert*-butyl)-keton**e 3-4**.

The newly formed thiophene diketone **3-4** was then reacted with various amines to complete the objective of forming sterically hindered azomethine dimers and trimers. To this end, the thiophene diketone was reacted with aniline, propylamine and other amines under standard dehydration/condensation reaction conditions. No azomethine containing products were formed after reaction with the amines mentioned under various dehydration conditions. The increased steric bulk around the carbonyl group likely made it very difficult for the amine to attack the carbonyl carbon making these reactions unfavourable. Even though these reactions were not capable of producing the desired products, they helped to confirm the hypothesis made in the introduction that the

increased steric bulk around the reaction centre would make any condensation reaction very difficult. Due to the lack of condensation reactions with the product **3-4**, new approaches towards sterically hindered thiophenes were examined.

Due to the overwhelming steric hindrance around the thiophene ketone in **3-4**, it was decided that a long alkyl chain could be added to the ketone moiety instead of the bulky *tert*-butyl groups. This approach would still offer some steric hindrance at the reaction site while at the same time allowing enough space for an amine to approach for a condensation reaction. It was shown in Chapter 1 that the addition of alkyl groups to the azomethine carbon significantly affected the barriers to bond rotation about the thiophene-CH bond. By adding longer alkyl chains, such as C_6, to the carbonyl carbon, a marked increase in the bond rotation barrier should be observed. To this end, 2,5-thiophenedicarboxylic acid was converted to its methyl ester by refluxing in methanol and was then subjected to a Grignard reaction in both oxidative (in the presence of CuCN) and non-oxidative conditions for replacing the methoxy group by a C_6 chain.

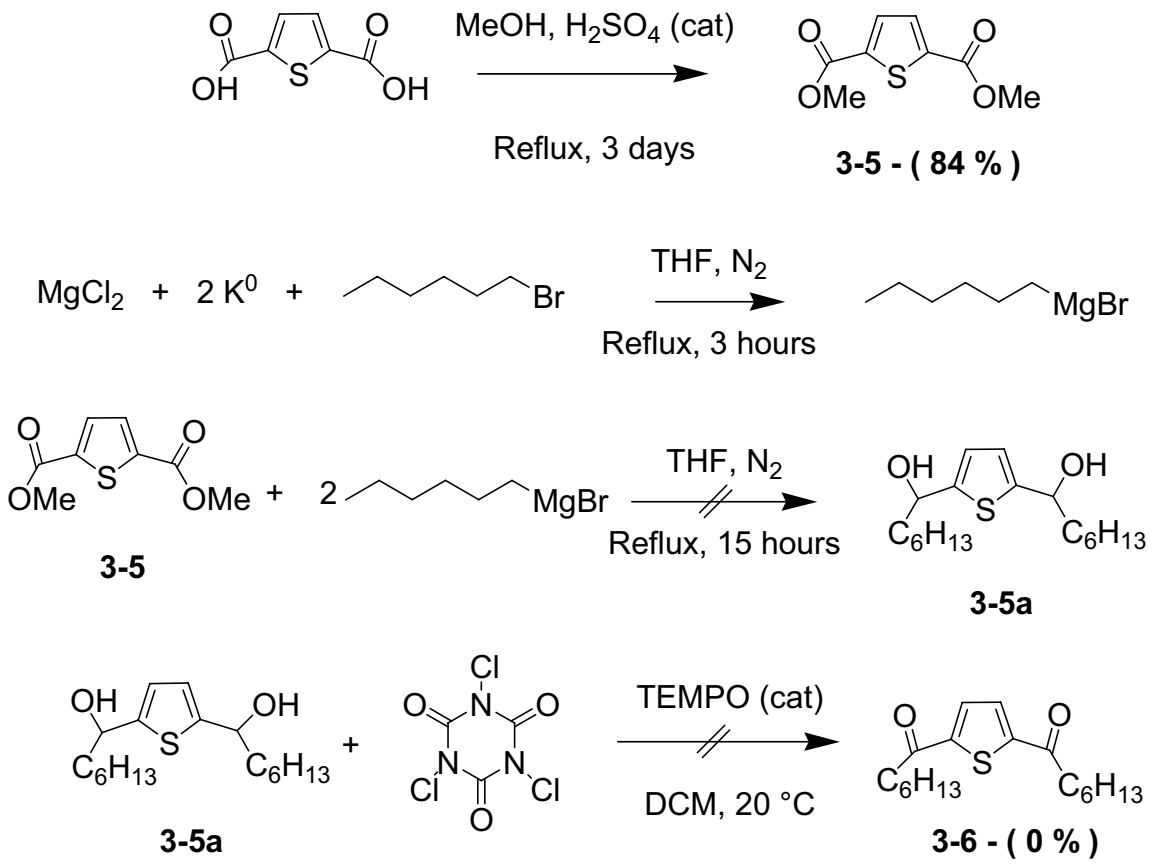

Figure 3-6. Synthesis of thiophene-2,5-dicarboxylic acid methyl ester , **3-5**, 1-[5-(1-Hydroxy-heptyl)-thiophen-2-yl]-heptan-1-ol, **3-5a**, by non-oxidative Grignard reaction and subsequent oxidation to 2,5-thiophene-di(hexylketone) **3-6**.

The Grignard reactions carried out under non-oxidative conditions followed a similar pathway to that previously described for the synthesis of 3,4-di-*tert*-butylthiophene **3-3**.[85] The Grignard reagent was formed from 1-bromohexane and elemental magnesium derived from the reduction of magnesium chloride by elemental potassium. After the Grignard reaction, the reaction mixture was subjected to mild oxidative conditions by the addition of trichloroisocyanuric acid in the presence of a catalytic amount of TEMPO.[87] The oxidation was designed to convert the tertiary alcohol **3-5a** from the Grignard reaction into the corresponding ketone, as shown in Figure 3-6.

^{1}H NMR and mass spectrometry measurements could not confirm the presence of the desired product after five reaction attempts, so a different methodolgy was examined.

The last reaction discussed in this section was a Grignard reaction carried out under oxidative reaction conditions. Instead of forming the tertiary alcohol from the methyl ester, catalytic CuCN was used to preserve the ketone **3-6** after the Grignard has added to the carbonyl carbon.[88] This reaction was also unsuccessful as the desired product was not detected in the reaction mixture. This reaction should also be approached with caution as CuCN is highly poisonous. The oxidative approach using CuCN is shown schematically in Figure 3-7.

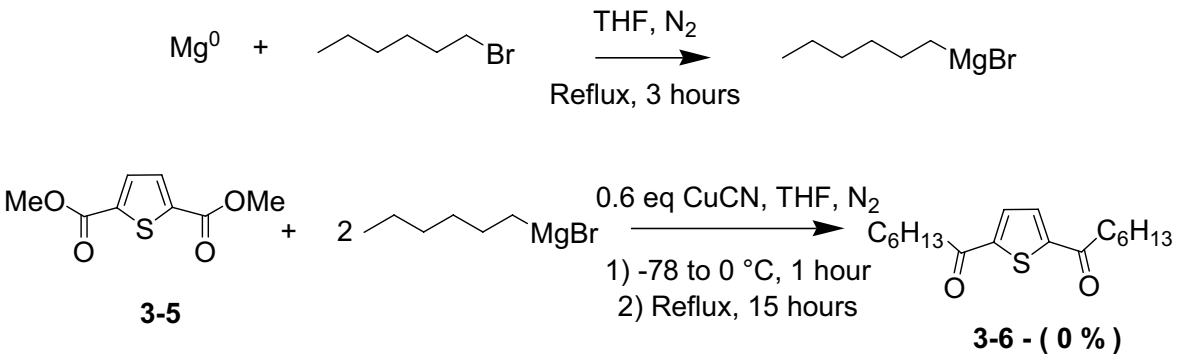

Figure 3-7. Synthesis of 2,5-thiophene-di(hexylketone) **3-6** from thiophene-2,5-dicarboxylic acid methyl ester **3-5** by oxidative Grignard reaction in the prescence of CuCN.

3.3 Experimental Section

3.3.1 General Procedures

All reagents were commercially available and were used as received unless otherwise stated. Anhydrous and deaerated solvents were obtained with a Glass Contour solvent purification system. ^{1}H NMR and ^{13}C NMR spectra were recorded on a Bruker 400 MHz spectrometer with the appropriate deuterated solvents

3.3.2 Synthetic Protocols

N-pentylpyridinium bromide (B1). In round-bottomed flask (50 mL) was added pyridine (0.12 mol, 10 mL) along with a few 4 Å molecular sieves to scavenge water. To this was added 1-bromopentane (0.024 mol, 3 mL) and the reaction mixture was heated at reflux for four hours with constant stirring. Excess pyridine was removed under reduced pressure overnight. The mixture was extracted using a diethyl ether/water mixture with the product moving into the water layer. The water was removed under reduced pressure and then the resultant liquid was further dried under reduced pressure in the presence of P_2O_5. The product was obtained as a clear orange liquid (4.40 g, 79 %). ^{1}H NMR (400MHz, [D] chloroform-d_1): δ = 9.53 (d, 2H, ^{3}J = 5.8 Hz), 8.47 (t, 1H, ^{3}J = 7.7 Hz), 8.08 (t, 2H, ^{3}J = 7.0 Hz), 4.89 (t, 2H, ^{3}J = 7.5 Hz), 1.95 (t, 2H, ^{3}J = 7.9 Hz), 1.28-1.21 (m, 4H), 0.74 (t, 3H, ^{3}J = 6.8 Hz).

N-pentylpyridinium tribromide (B2). In a round-bottomed flask (50 mL) was added **B1** (0.019, 4.4 g). The reaction flask was cooled to 10 °C for the course of the reaction. To this was added liquid bromine (0.019 mol, 1.0 mL) in a drop-wise fashion, over the course of 15 minutes, ensuring that the temperature did not significantly increase. The initial orange solution quickly turned to deep red upon the addition of the

red-brown bromine. The mixture was stirred overnight at room temperature under reduced pressure. The product was obtained pure from the reaction mixture, without further treatment, as a red liquid (5.6 g, 76%). ^{1}H NMR (400MHz, [D] acetone-d_6): δ = 9.64 (d, 2H, ^{3}J = 5.9 Hz), 8.78 (t, 1H, ^{3}J = 7.7 Hz), 8.32 (t, 2H, ^{3}J = 6.9 Hz), 5.04 (t, 2H, ^{3}J = 7.5 Hz), 2.11 (p, 2H, ^{3}J = 7.0 Hz, 7.9 Hz), 1.42-1.32 (m, 4H), 0.86 (t, 3H, ^{3}J = 7.0 Hz).

Bromopinacolone (3-1). A two-necked round-bottomed flask (50 mL) was charged with pinacolone (8.2 mmol, 1.0 mL) to which was added **B2** (8.4 mmol, 3.25 g) in three fractions. The clear solution of pinacolone turned red/orange upon addition of the red/orange brominating agent **B2**. The reaction mixture was stirred under ambient conditions for three hours and then extracted with a diethyl ether/water mixture. The diethyl ether layer was then evaporated under reduced pressure. ^{1}H NMR experiments did not show the prescence of the desired product, only starting pinacolone.

Tetrabutylammonium tribromide (B3). To a round-bottomed flask (250 mL) was added tetrabutylammonium bromide (0.031 mol, 9.99 g) dissolved in distilled water (50 mL). To this was added sodium borate (0.018 mol, 1.50 g) and then, with constant stirring, 48 % hydrobromic acid solution in water (0.065 mol, 7.0 mL). Upon complete addition of hydrobromic acid, a deep orange precipitate was formed. This precipitate was filtered and washed with diethyl ether yielding the product as an orange crystalline solid (13.22 g, 93%). The product was used directly in the next step of synthesis without further characterization.

Bromopinacolone (3-1). To a round-bottomed flask (50 mL) containing pinacolone (5.0 mmol, 0.5 g) was added a solution of **B3** (5.4 mmol, 2.61 g) dissolved in dichloromethane (20 mL). The reaction was stirred for three hours and the solvent was then removed. The reaction mixture was extracted with dichloromethane/water. The dichloromethane fractions were combined and the solvent removed under reduced pressure. ^{1}H NMR experiments did not show the prescence of the desired product, nor the starting materials.

1-(3,3-Dimethyl-2-oxo-butylsulfanyl)-3,3-dimethyl-butan-2-one (3-2). In a round-bottomed flask (100 mL) was added bromopinacolone (11.3 mmol, 2.03 g) which was then dissolved in acetone (20 mL). The flask was then cooled to 0 °C in an ice-water bath. To this was added, by dropwise addition under a nitrogen atmosphere, a solution of sodium sulfide nonahydrate (5.67 mmol, 1.36 g) dissolved in distilled water (10 mL). The mixture was stirred at 0 °C for 15 minutes, and then the mixture was warmed to room temperature and stirred for an additional 18 hours. The product precipitated as a white powder and was removed by filtration. Drying over $MgSO_4$ yielded the product as a white powder (1.1 g, 84%). ^{1}H NMR (400MHz, [D] acetone-d_6): δ = 3.65 (s, 4H), 1.16 (s, 18H).

3,4-di-*tert*-butylthiophene (3-3). In a two-neck round-bottomed flask (50 mL) was added diketosulfide **3-2** (1.36 g, 5.9 mmol) dissolved in THF (15 mL). To this was added zinc powder (50 mmol, 3.25 g). The reaction vessel was kept under a nitrogen atmosphere and cooled to -10 °C using a NaCl/H_2O ice bath. To this solution, $TiCl_4$ 1 M in THF (18 mmol, 18 mL), was added dropwise over 20 minutes. After stirring for four hours on the ice bath, 100 g of ice was added to quench the reaction. The mixture was

extracted with dichloromethane, the resulting fractions were combined and the solvent removed under reduced pressure. None of the desired product was observed by ^{1}H NMR. This reaction produced a terribly pungent product which was not identified. Extreme caution should be taken to ensure that the pungent compound is properly contained within a fumehood.

3,4-di-*tert*-butylthiophene (3-3). To first prepare reactive elemental magnesium, dried magnesium chloride (12.2 mmol, 1.17 g) was added to a two-necked round-bottomed flask (100 mL). To this was added anhydrous THF (15 mL) followed by elemental potassium (24 mmol, 0.94 g). The reaction mixture was then stirred for two hours at reflux under an inert atmosphere. The solution turned dark grey and once all of the $MgCl_2$ was reacted (by visual inspection), *tert*-butyl chloride (13 mmol, 1.2 g) was added via a syringe. The mixture was stirred at reflux for 5 minutes at which point the Grignard reagent was transferred via cannula line to a three-necked round-bottomed flask (250 mL). The second flask, held under a constant flux of nitrogen gas, contained 3,4-dibromothiophene (3.05 mmol, 1.00 g) and the catalyst $Ni(dppp)_2Cl$ (0.15 mmol, 74.4 mg) dissovled in THF (40 mL). Prior to addition of the Grignard, the second flask was subjected to three freeze-thaw cycles using liquid nitrogen, while held under vacuum, to ensure the complete removal of oxygen. Upon addition of the Grignard reagent to the second flask, the mixture was heated to reflux and stirred for an additional 18 hours. ^{1}H NMR of the resultant reaction mixture did not show the presence of *tert*-butylated thiophene, only that of the starting material dibromothiophene and a small amount of *tert*-butylchloride.

2,5-thiophene-(di-*tert*-butyl)-ketone (3-4). A 0.44 M solution of sodium methoxide was produced by slowly adding 100 mg of sodium metal to dry methanol (10 mL). Glyoxal trimer dihydrate (4.8 mmol of monomer, 336 mg) was added to methanol (30 mL) and heated at reflux for an hour to ensure complete dissolution of the trimer. After the trimer was dissolved, the mixture was cooled to room temperature and the diketosulfide **3-2** (4.0 mmol, 921 mg) was added. To this was added the sodium methoxide solution by dropwise addition over 10 minutes. The mixture was stirred at room temperature for 10 minutes, then at reflux for one hour. The title product precipitated from the reaction mixture upon addition of 50 mL of H_2O. The product was filtered and dried over $MgSO_4$, yielding the title product as a white powder (388 mg, 42%). ^{1}H NMR (400MHz, [D] acetone-d_6): δ = 7.91 (s, 2H), 1.38 (s, 18H).

Thiophene-2,5-dicarboxylic acid dimethyl ester (3-5). To a stirred solution of 2,5-thiophenedicarboxylic acid (7.9 mmol, 1.36 g) dissovled in methanol (200 mL), was added three drops of H_2SO_4. The mixture was stirred at reflux for 72 hours. The reaction mixture was dried and the crude white solid was purified by silica gel column chromatography eluted with 100% dichloromethane. The product fractions were collected and the solvent removed yielding the methyl ester product as a white powder (1.29 g, 84%). ^{1}H NMR (400MHz, [D] methanol-d_3): δ = 7.77 (s, 2H), 3.91 (s, 6H).

1-(5-Heptanoyl-thiophen-2-yl)-heptan-1-one (3-6). In a round-bottomed flask (100 mL), dried magnesium chloride (18.9 mmol, 1.8 g) and metallic potassium (38.3 mmol, 1.5 g) were mixed in anhydrous THF (50 mL). The reaction mixture was stirred under nitrogen atmosphere, at reflux, for three hours until the THF had turned a cloudy grey colour. The mixture was cooled to room temperature at which point 1-bromohexane

(19.9 mmol, 3.06 g) was added. The mixture was stirred for an additional five minutes before being transferred via cannula line into a second flask containing a solution of the methyl ester (5.0 mmol, 1.0 g,) dissolved in anhydrous THF (20 mL). The mixture was heated to reflux overnight, 15 hours, under a constant flux of nitrogen. The crude reaction mixture was poured into a 1 M HCl solution and extracted three times with dichloromethane. The organic fractions were collected and the solvent removed. The crude product mixture was re-dissolved in dichloromethane (25 mL) to which was added trichloroisocyanuric acid (10.5 mmol, 2.45 g). The mixture was cooled to 0 °C and stirred for 15 minutes at which point TEMPO (0.105 mmol, 19.7 mg) was added. The reaction mixture was warmed to room temperature and stirred for an additional 6 hours. The mixture was washed with a saturated Na_2CO_3 solution, followed by a 1 M NaCl solution. Mass spectra of the washed ogranic fractions were recorded with no masses corresponding to that of the desired product. ^{1}H NMR also indicated that the desired product was not formed.

1-(5-Heptanoyl-thiophen-2-yl)-heptan-1-one (3-6). In a round-bottomed flask (100 mL), dried elemental magnesium (5.0 mmol, 122 mg) and 1-bromohexane (5.5 mmol, 908 mg) were mixed in anhydrous THF (50 mL). The reaction mixture was stirred at reflux under nitrogen atmosphere for three hours until the THF turned a cloudy grey colour. The mixture was cooled to room temperature and transferred via cannula line into a second flask containing a suspension of copper (I) cyanide (0.73 mmol, 65.2 mg) and the methyl ester **3-5** (5.0 mmol, 1.0 g) dissolved in anhydrous THF (25 mL). The mixture was heated to reflux for 15 hours, under a constant flux of nitrogen. The crude reaction mixture was poured into an ice water solution and extracted three times with diethyl ether

and washed with a sodium hypophosphate solution. ^{1}H NMR of the crude product indicated the presence of the starting methyl ester, but did not show the prescence of the desired ketone.

3.4 Conclusions and Future Work

While many of the reactions in this section were unsuccessful, this research has helped to lay the ground work for the approaches that need to be followed when attempting to form sterically hindered azomethines. Given that some smaller, yet still hindered, azomethines were prepared, it leaves open options for future work in this area including the use of the thiophene diketone **3-4** towards making new azomethines, the addition of bulky groups to the 3-,4-positions of the thiophene as well as other substitutions including the insertion of other heterocycles.

This work was also able to determine some issues concerning the preparation of sterically hindered azomethines which will undoubtedly be useful for researchers who choose to continue down similar paths. In the end, a small portion of the desired syntheses were unsuccessful, but with the ease with which azomethines can be prepared, a large catalogue of sterically hindered thiophene azomethines dyads has been prepared and a much larger catalogue is not far from reach.

General Conclusions:

Conjugated thiophenes have attracted much attention in recent years due to the fact that they have demonstrated attractive physical properties that can make them suitable replacements for current materials. Their variable physical properties make them interesting materials for real-world applications including a variety of organic electronic devices including OLEDs, OFETs and NLOs. A major issue confronting their use is their synthesis, which often requires expensive catalysts and extensive purification procedures.

Thiophene azomethines, which incorporate the azomethine linkage (C=N) in place of conventional carbon-carbon linkages, are of significant interest because their preparation proceeds through a one-pot reaction that requires minimal purification. In addition, thiophene azomethines can be substituted in many ways leading to highly varied photophysical and electrochemical properties.

In stark contrast with their isoelectronic alkene (C=C) counterparts, conjugated azomethines demonstrate no fluorescence. Arylvinylenes which contain large degrees of conjugation through extended pi-bonding backbones regularly demonstrate high fluorescence quantum yields (e.g. anthracene and fluorene). These types of highly fluorescent molecules often contain inflexible backbones that disallow excited state deactivation via the internal conversion (IC) processes of bond rotation and vibration. These restrictions to bond rotations are often a main cause of fluorescence enhancement in organic molecules.

The initial objective of Chapter 1 was to deactivate the excited state decay pathway of internal conversion by increasing the amount of steric bulk in the vicinity of the central azomethine linkage in a series of thiophene-aniline dyads. By increasing the

barrier to bond rotation, it was foreseen that the fluorescence quantum yield would increase due to a decrease in the quantum yield of internal conversion. However, it was shown through fluorescence quantum yield measurements that in fact all of the studied azomethine dyads were effectively non-fluorescent. Quantum calculations of bond rotation barriers demonstrated that substitutions made on the thiophene and azomethine carbons caused more significant changes in the barriers to bond rotation than substitutions on the aniline ring.

After it was determined that internal conversion processes were not significantly involved in excited state decay, experiments were devised to study the other methods of excited state decay. To further investigate the excited state decay mechanisms of thiophene azomethines, bimolecular quenching experiments were carried out. These experiments, along with phosphorescence data, demonstrated that the excited state in azomethines is very quickly deactivated via intersystem crossing to the triplet state, and to a much larger extent, photoinduced electron transfer (PET) processes.

Through the study of Stern-Volmer relationships, it was shown that azomethines can be used to quench the both the singlet and triplet excited states of the fluorophores bithiophene and fluorene. Azomethines are able to quench their own excited states, as is the case in the thiophene azomethines presented herein, via unimolecular photoinduced electron transfer. Rehm-Weller calculations based on electrochemical oxidation and reduction potentials were used to demonstrate that PET is energetically favourable for all of the dyads studied.

In Chapter 2, metal complexes based on a thiophene-hydroxyquinoline ligand were prepared. The ligand, $\mathbf{L_4}$, contains a central azomethine linkage. As with the dyads

presented in Chapter 1, all of the ligands prepared in Chapter 2 and their subsequent metal complexes, demonstrated no fluorescence. As the ligand formed complexes with the metal centres an increase in fluorescence was envisioned due to an increase in the rigidity of the backbone. However, fluorescence was non-existent in both the free ligand state and in the complexes which gives further evidence that internal conversion processes do not play a central role in excited state decay. In addition to this, a metal ion sensor was prepared via simple spin-coating techniques. The device was capable of detecting the presence of copper (II) ions in solution and the azomethine ligand was shown to be resistant to water when submerged for 30 minutes.

Chapter 3 discussed some of the synthetic protocols used in this work that did not provide the desired products. This work outlined some of the difficulties that arise during the synthesis of sterically hindered molecules. The work presented in Chapter 3 stands as an excellent starting point for the continued synthesis of highly hindered thiophene azomethines.

The work presented herein provides a detailed look at the photophysical properties, and to a larger extent the excited state decay mechamisms, of thiophene azomethines. Bimolecular quenching experiments demonstrated that azomethines can be used to efficiently and rapidly quench excited states. As a result of this, fluorescence and phosphorescence can also be rapidly deactivated. These physical properties, along with the incomparable ease of synthesis and purification, make thiophene azomethines an interesting set of materials with potential applications wherever excited states need deactivating.

References

[1] Yang, C.-J.; Jenekhe, S. A. *Chem. Mater.* **1991**, *3*, 878.

[2] Mannerbro, R.; Ranlöf, M.; Robinson, N.; Forchheimer, R. *Synth. Met.* **2008**, 158, 556.

[3] Hou, J.; Park, M.-H.; Zhang, S.; Yao, Y.; Chen, L.-M.; Li, J.-H.; Yang, Y. *Macromolecules* **2008**, *41*, 6012.

[4] Blouin, N.; Leclerc, M. *Acc. Chem. Res.* **2008**, *41*, 1110.

[5] Yokoyama, A.; Suzuki, H.; Kubota, Y.; Ohuchi, Y.; Higashimura, H. ; Yokozawa, T. *J. Am. Chem. Soc.* **2007**, *129*, 7236.

[6] Xu, Q.; An, L.; Yu, M.; Wang, S. *Macromolecules: Rapid Comm.* **2008**, *29*, 390.

[7] Galand, E. M.; Mwaura, J. K.; Argun, A. A.; Abboud, K. A.; McCarley, T. D.; Reynolds J. R. *Macromolecules* **2006**, *39*, 7286.

[8] Banishoeib, F.; Henckens, A.; Fourier, S.; Vanhooyland, G.; Breselge, M.; Manca, J.; Cleij, T. J.; Lutsen, L.; Vanderzande, D.; Nguyen, L. H.; Neugebauer, H.; Sariciftci, N. S. *Thin Solid Films*, **2008**, *516*, 3978-3988.

[9] Oswald, F.; Islam, D.-M. S.; Araki, Y.; Troiani, V.; de la Cruz, P.; Moreno, A.; Ito, O.; Fernando Langa. *Chem. Eur. J.* **2007**, *13*, 3924.

[10] Nishide, Y.; Osuga, H.; Saito, M.; Aiba, T.; Inagaki, Y.; Doge, Y.; Tanaka, K. *J. Org. Chem.* **2007**, *72*, 9141.

[11] Lukes, V.; Matis, M.; Végh, D.; Stefko, M.; Hrdlovic, P.; Laurinc, V. *Synth. Met.* **2007**, *157*, 770.

[12] Tsuge, A.; Hara, T.; Moriguchi, T. *Tetrahedron Lett.* **2009**, *50*, 4509.

[13] Kim, D.-S.; Ahn, K. H. *J. Org. Chem.* **2008**, *73*, 6831.

[14] Dufresne, S.; Hanan, G. S.; Skene, W. G. *J. Phys. Chem. B* **2007**, *111*, 11407.

[15] Kavarnos, G. J. *Fundamentals of Photoinduced Electron Transfer*, VHC Publishers, New York, **1993**; Chapter 1.

[16] Lakowicz, J.R. *Principles of Fluorescence Spectroscopy*, Plenum Press, New York, **1983**; Chapter 1.

[17] Sciano, J. C. *J. Am. Chem. Soc.* **1980**, *102*, 7743.

[18] Tsang, D.; Bourgeaux, M.; Skene. W.G. *J. Photochem. Photobiol. A,* **2007**, *192*, 122.

[19] Raven, P. H.; Evert, R. F., Eichhorn, S. E., *Biology of Plants, 7th Edition*, New York, W.H. Freeman and Company Publishers, **2005**, 124–127.

[20] Pushkar Y., Yano J., Sauer K., Boussac A., Yachandra V. K., *Proc. Nat. Acad. Sci.* **2008,** *105*, 1879.

[21] Yorozu, T.; Hoshino, M.; Imamura, M. *J. Phys. Chem.*, **1982**, *86*, 4422.

[22] Weller, A.; *Zeitschr. Phys. Chem*. **1982**, *NF 133*, 93.

[23] Heitele, H.; Finckh, P.; Weeren, S.; Pöllinger, F.; Michel-Beyerle, M. E. *J. Phys. Chem.* **1989**, *93*, 5173.

[24] Sinha, J.; Sahoo, R.; Kumar, A. *Macromolecules* **2009**, *42*, 2015.

[25] Lee, W.-H.; Kong, H.; Oh, S.-Y.; Shim, H.-K.; Kang, I.-N. *J. Polym. Sci. A,* **2009**, *47*, 111.

[26] Yu, N.; Zhu, R.; Peng, B.; Huang, W.; Wei, W. *J. Appl. Polym. Sci.* **2008**, *108*, 2438.

[27] Qian, Y.; Meng, K.; Lu, C.-G.; Lin, B.-p.; Huang, W.; Cui, Y.-P. *Dyes & Pigm.* **2009**, *80*, 174.

[28] Beryozkina, T.; Senkovskyy, V.; Kaul, E.; Kiriy, A. *Macromolecules* **2008**, *41*, 7817.

[29] Pérez Guarìn, S. A.; Dufresne, S.; Tsang, D.; Sylla, A.; Skene, W. G. *J. Mater. Chem.* **2007**, *17*, 2801.

[30] Pérez Guarìn, S. A.; Bourgeaux, M.; Dufresne, S.; Skene, W. G. *J. Org. Chem.* **2007**, *72*, 2631.

[31] Pérez Guarìn, S. A.; Skene, W. G. *Mater. Lett.* **2007**, *61*, 5102.

[32] Dufresne, S.; Bourgeaux, M.; Skene, W. G. *J. Mater. Chem.* **2007**, *17*, 1166.

[33] Bourgeaux, M.; Skene, W. G. *J. Org. Chem.* **2007**, *72*, 8882.

[34] Bourgeaux, M.; Perez Guarin, S. A.; Skene, W. G. *J. Mater. Chem.* **2007**, *17*, 972.

[35] Seixas de Melo, J.; Elisei, F.; Gartner, C.; Aloisi, G. G.; Becker, R. S. *J. Phys. Chem. A,* **2000**, *104*, 6907.

[36] Seixas de Melo, J.; Silva, L. M.; Arnaut, L. G.; Becker, R. S. *J. Chem. Phys.* **1999**, *111*, 5427.

[37] Becker, R. S.; Seixas de Melo, J.; Maçanita, A. L.; Elisei, F. *J. Phys. Chem.* **1996**, *100*, 18683.

[38] Tsai, F.-C.; Chang, C.-C.; Liu, C.-L.; Chen, W.-C.; Jenekhe, S. A. *Macromolecules* **2005**, *38*, 1958.

[39] Liu, C.-L.; Chen, W.-C. *Macromol. Chem. Phys.* **2005**, *206*, 2212.

[40] Graulich, A.; Liégeois, J.-F. *Synthesis* **2004**, 1935.

[41] Puranik, M.; Chandrasekhar, J.; Umapathy, S. *Chem. Phys. Lett.* **2001**, *337*, 224.

[42] Turro, N. J.; Ramamurthy, V.; Scaiano, J. C. *Principles of Molecular Photochemistry: An Introduction*; University Science Books: Sausalito, **2009**.

[43] Seixas de Melo, J.; Rodrigues, L. M.; Serpa, C.; Arnaut, L. G.; Ferreira, I. C. F. R.; Queiroz, M. J. R. P. *Photochem. Photobiol.* **2003**, *77*, 121.

[44] Wex, B.; Kaafarani, B. R.; Danilov, E. O.; Neckers, D. C. *J. Phys. Chem. A,* **2006**, *110*, 13754.

[45] Pinkham, C. A.; Wait, S. C. *J. Mol. Spectrosc.* **1968**, *27*, 326.

[46] Assuming the density of the thiophene azomethines to be ca. 0.8 g/ml.

[47] Kavarnos, G. J.; Turro, N. J. *Chem. Rev.* **2002**, *86*, 401.

[48] Sarker, A. M.; Kaneko, Y.; Nikolaitchik, A. V.; Neckers, D. C. *J. Phys. Chem. A* **1998**, *102*, 5375.

[49] Gilbert, A.; Baggott, J. *Essentials of Molecular Photochemistry*; CRC Press: Boca Raton, **1991**.

[50] Sliwa, M.; Spangenberg, A.; Métivier, R.; Létard, S.; Nakatani, K.; Yu, P. *Res. Chem. Intermed.* **2008**, *34*, 181.

[51] Evans, C.; Weir, D.; Scaiano, J. C.; Mac Eachern, A.; Arnason, J. T.; Morand, P.; Hollebone, B.; Leitch, L. C.; Philogene, B. J. R. *Photochem. Photobiol.* **1986**, *44*, 441.

[52] Tuna F.; Lees M. R.; Clarkson G. J.; Hannon M. J. *Chem. Eur. J.* **2004**, *10*, 5737.

[53] Dufresne S.; Skene W. G. *J. of Org. Chem.* **2008**, *73*, 3859.

[54] Tang C. W.; VanSlyke, S. A. *J. Appl. Phys.* **1989**, *65*, 3610.

[55] Ghedini M.; La Deda, M.; Aiello I.; Grisolia, A. *J. Chem. Soc. Dalton Trans.* **2002**, 3406.

[56] Meyers A.; Weck, M. *Macromolecules* **2003**, *36*, 1766.

[57] Zeng H.; Huang, W.; Shi, J. *Chem. Comm.* **2006**, 880.

[58] Kornyeyev, D. Y. *Photosynthetica* **1998**, *35*, 269.

[59] Berthomieu, C.; Hienerwadel, R. *Biochemistry* **2001**, *40*, 4044.

[60] Ismail, T. M. A. *J. Coord. Chem.* **2005**, *58*, 141.

[61] Asher, S. A.; Charma, A. C.; Goponenko, A. V.; Ward, M. M. *Anal. Chem.* **2003**, *75*, 1676.

[62] Cheng, Y.; Zhang, M.; Yang, H.; Li, F.; Yi, T.; Huang, C. *Dyes and Pigments* **2008**, *76*, 775.

[63] Lehn, J.-M. *Angew. Chem. Int. Ed.* **1990**, *29*, 1304.

[64] Hannon, M. J.; Painting, C. L.; Alcock, N. W. *Chem. Comm.* **1999**, 2023.

[65] Horowitz, E.; Tryon, M.; Christensen, R. G.; Perros, T. P. *J. of Appl. Polym. Sci.* **1965**, *9*, 2321.

[66] Drisko, R. W.; McKennis, Jr., H. *J. Am. Chem. Soc.* **1952**, *74*, 2626.

[67] Wakizaka, D.; Fushimi, T.; Ohkita, H.; Ito, S. *Polymer* **2004**, 45(25), p. 8561-8565.

[68] Wang, D.; Cui, D; Miao, W.; Li, S.; Huang, B. *J. Chem. Soc. Dalton Trans.* **2007**, 4576.

[69] Lu, C. C.; Bill, E.; Weyhermüller, T.; Bothe, E.; Wieghardt, K. *J. Am. Chem. Soc.* **2008**, *130*, 3181.

[70] Wezenburg, S. J.; Escudero-Adán, E. J.; Benet-Buchholz, J.; Kleij, A. W. *Org. Letters* **2008**, 10(15), 3311.

[71] La Deda, M.; Grisolia, A.; Aiello, I.; Crispini, A.; Ghedini, M.; Belviso, S.; Amati, M.; Lelj, F. *J. Chem. Soc. Dalton Trans.* **2004**, 2424.

[72] Ghedini, M.; La Deda, M.; Aiello, I.; Grisolia, A. *Inorg. Chim. Acta* **2004**, *357*, 33.

[73] Giraudi, G.; Baggiani, C.; Giovannoli, C.; Marletto, C.; Vanni, A. *Anal. Chim. Acta* **1999**, *378*, 225.

[74] Gladis, J. M.; Prasada Rao, T. *Anal. Bioanal. Chem.* **2002**, *373*, 867.

[75] Xie, J.; Fan, L.; Su, J.; Tian, H. *Dyes and Pigments* **2003**, *59*, 153.

[76] Yue, Y.-F.; Gao, E.-Q.; Fang, C.-J.; He, Z.; Bai, S.-Q.; Yan, C.-H. *Polyhedron* **2005**, *25*, 2778.

[77] Hamblin, J.; Tuna, F.; Bruce, S.; Childs, L. J.; Jackson, A.; Errington, W.; Alcock, N. W.; Nierengarten, H.; Van Dorsselaer, A.; Leize-Wagner, E.; Hannon, M. J. *Chem. Eur. J.* **2007**, *13*, 9286.

[78] Bourgeaux, M.; Vomscheid, S.; Skene, W. G. *Synth. Comm.* **2007**, *37*, 3551.

[79] Clemo, G. R.; Howe, R. *J. Chem. Soc.*, **1955**, 3552.

[80] Cox, R. A.; Warkentin, J. *Can. J. Chem.* **1972**, *50*, 3242.

[81] Kajigaeshi, S.; Kakinami, T.; Okamoto, T.; Fujisaki, S. *Chem. Soc. Jap.* **1987**, *60*, 1159.

[82] Salazar, J.; Dorta, R. *Synth. Lett.* **2004**, *7*, 1318.

[83] Zhu, Y.; Ching, C.; Carpenter, K.; Xu, R.; Selvaratnam, S. Hosmane, N. S.; Maguire, J. A. *Appl. Organomet. Chem.* **2003**, *17*, 346.

[84] Nakayama, J.; Yamaoka, S.; Nakanishi, T.; Hoshino, M. *J. Am. Chem. Soc.* **1988**, *110*, 6598.

[85] Rieke, R. D.; Bales, S. E. *J. Amer. Chem. Soc.* **1974**, *96*, 1775.

[86] Miyahara, Y. *J. Het. Chem.* **1979**, *16*, 1147.

[87] de Luca, L.; Giacomelli, G.; Porcheddu, A. *Org. Lett.* **2001** *3*, 3041.

[88] Hansford, K. A.; Pérez-Guarìn, S. A.; Skene, W. G.; Lubell, W. D. *J. Org. Chem.* **2005**, *70*, 7996-8000.

Appendix A

Supporting Information

Chapter 1: Thiophene-Phenyl Azomethines with Varying Rotational Barriers – Model Compounds for Examining Imine Fluorescence Deactivation

Article 1

Alex N. Bourque, Stéphane Dufresne, W. G. Skene

Centre for Self-Assembled Chemical Structures, Department of Chemistry
Université de Montréal, Pavillon J.A. Bombardier, C.P. 6128, succ. Centre-Ville, Montreal QC, H3C3J7, Canada

Published:

Journal of Physical Chemistry C, **2009**, 113, 19677-19685

Table of Figures

Figure A-1. Absorption (■), fluorescence (●) and phosphorescence (▲) spectra of **1-1**. III
Figure A-2. Absorption (■), fluorescence (●) and phosphorescence (▲) spectra of **1-2**. III
Figure A-3. Absorption (■), fluorescence (●) and phosphorescence (▲) spectra of **1-3**. IV
Figure A-4. Absorption (■), fluorescence (●) and phosphorescence (▲) spectra of **1-4**. IV
Figure A-5. Absorption (■), fluorescence (●) and phosphorescence (▲) spectra of **1-5**. V
Figure A-6. Absorption (■), fluorescence (●) and phosphorescence (▲) spectra of **1-6**. V
Figure A-7. Absorption (■), fluorescence (●) and phosphorescence (▲) spectra of **1-7**. VI
Figure A-8. Absorption (■), fluorescence (●) and phosphorescence (▲) spectra of **1-8**. VI
Figure A-9. Absorption (■) and fluorescence (●) spectra of **1-9**. VII
Figure A-10. Absorption (■) and fluorescence (●) spectra of **1-10**. VII
Figure A-11. Cyclic voltammogram of **1-1** in deaereated acetonitrile solution of 0.1 M of TBA-PF_6 using Ag/AgCl as reference and Pt as working electrodes. VIII
Figure A-12. Cyclic voltammogram of **1-2** in deaereated acetonitrile solution of 0.1 M of TBA-PF_6 using Ag/AgCl as reference and Pt as working electrodes. VIII
Figure A-13. Cyclic voltammogram of **1-3** in deaereated acetonitrile solution of 0.1 M of TBA-PF_6 using Ag/AgCl as reference and Pt as working electrodes. IX
Figure A-14. Cyclic voltammogram of **1-4** in deaereated acetonitrile solution of 0.1 M of TBA-PF_6 using Ag/AgCl as reference and Pt as working electrodes. IX
Figure A-15. Cyclic voltammogram of **1-5** in deaereated acetonitrile solution of 0.1 M of TBA-PF_6 using Ag/AgCl as reference and Pt as working electrodes. X
Figure A-16. Cyclic voltammogram of **1-6** in deaereated acetonitrile solution of 0.1 M of TBA-PF_6 using Ag/AgCl as reference and Pt as working electrodes X
Figure A-17. Cyclic voltammogram of **1-7** in deaereated acetonitrile solution of 0.1 M of TBA-PF_6 using Ag/AgCl as reference and Pt as working electrodes. XI
Figure A-18. Cyclic voltammogram of **1-8** in deaereated acetonitrile solution of 0.1 M of TBA-PF_6 using Ag/AgCl as reference and Pt as working electrodes. XI
Figure A-19. Cyclic voltammogram of **1-9** in deaereated acetonitrile solution of 0.1 M of TBA-PF_6 using Ag/AgCl as reference and Pt as working electrodes. XII
Figure A-20. ^{1}H Spectrum of **1-1** in deuterated acetone. XII
Figure A-21. ^{1}H Spectrum of **1-2** in deuterated acetone. XIII
Figure A-22. ^{13}C Spectrum of **1-2** in deuterated acetone. XIII
Figure A-23. ^{1}H Spectrum of **1-3** in deuterated acetone. XIV
Figure A-24. ^{13}C Spectrum of **1-3** in deuterated acetone. XIV
Figure A-25. ^{1}H Spectrum of **1-4** in deuterated acetone. XV
Figure A-26. ^{13}C Spectrum of **1-4** in deuterated acetone. XV
Figure A-27. ^{1}H Spectrum of **1-5** in deuterated acetone. XVI
Figure A-28. ^{13}C Spectrum of **1-5** in deuterated acetone. XVI
Figure A-29. ^{1}H Spectrum of **1-6** in deuterated acetone. XVII
Figure A-30. ^{13}C Spectrum of **1-6** in deuterated acetone. XVII
Figure A-31. ^{1}H Spectrum of **1-7** in deuterated acetone. XVIII
Figure A-32. ^{13}C Spectrum of **1-7** in deuterated acetone. XVIII
Figure A-33. ^{1}H Spectrum of **1-8** in deuterated acetone. XIX
Figure A-35. ^{13}C Spectrum of **1-8** in deuterated acetone. XIX
Figure A-34. ^{13}C Spectrum of **1-8** in deuterated acetone. I
Figure A-36. ^{1}H Spectrum of **1-9** in deuterated acetone. XX
Figure A-37. ^{13}C Spectrum of **1-9** in deuterated acetone. XX
Figure A-38. ^{1}H Spectrum of **1-10** in deuterated chloroform. XXI
Figure A-39. ^{13}C Spectrum of **1-10** in deuterated chloroform XXI

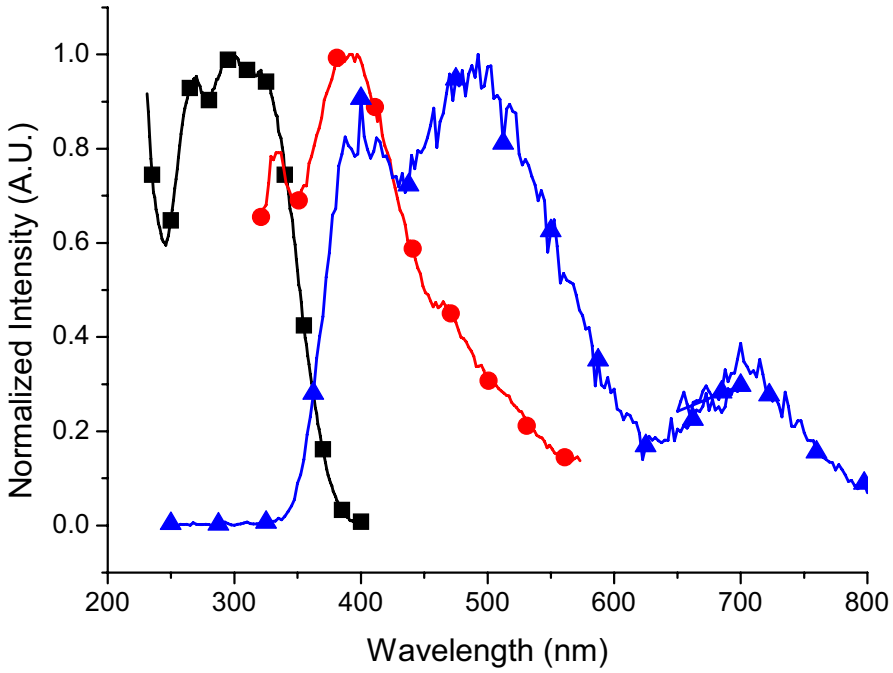

Figure A-0-1. Absorption (■), fluorescence (●) and phosphorescence (▲) spectra of **1-1.**

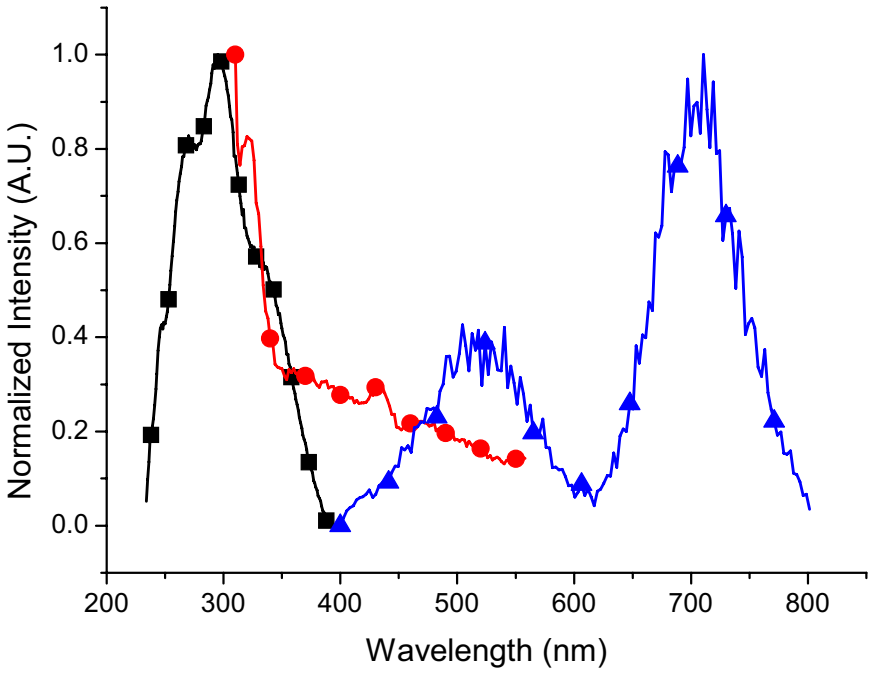

Figure A-0-2. Absorption (■), fluorescence (●) and phosphorescence (▲) spectra of **1-2**.

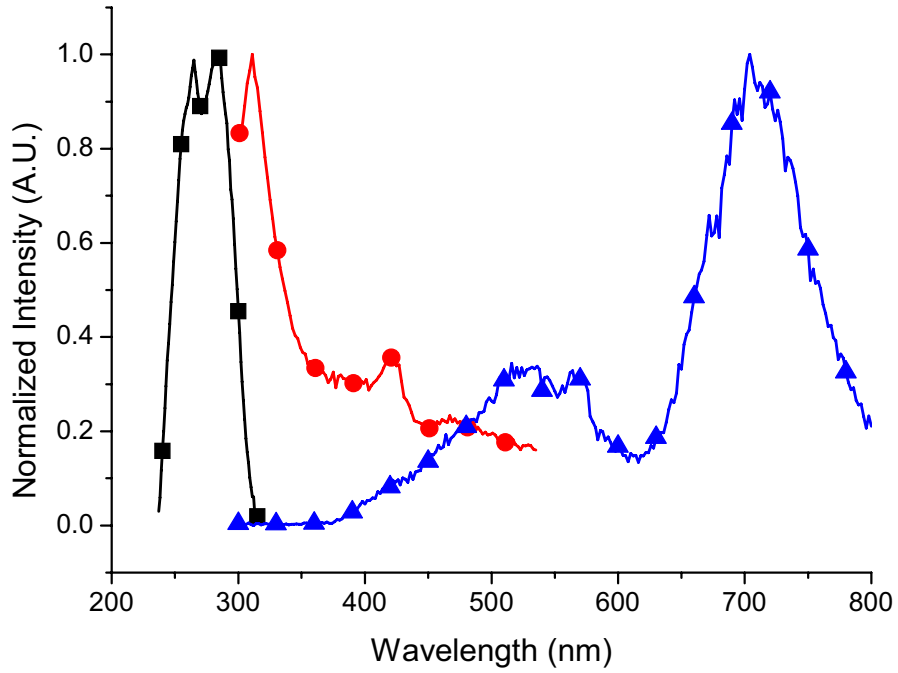

Figure A-0-3. Absorption (■), fluorescence (●) and phosphorescence (▲) spectra of **1-3**.

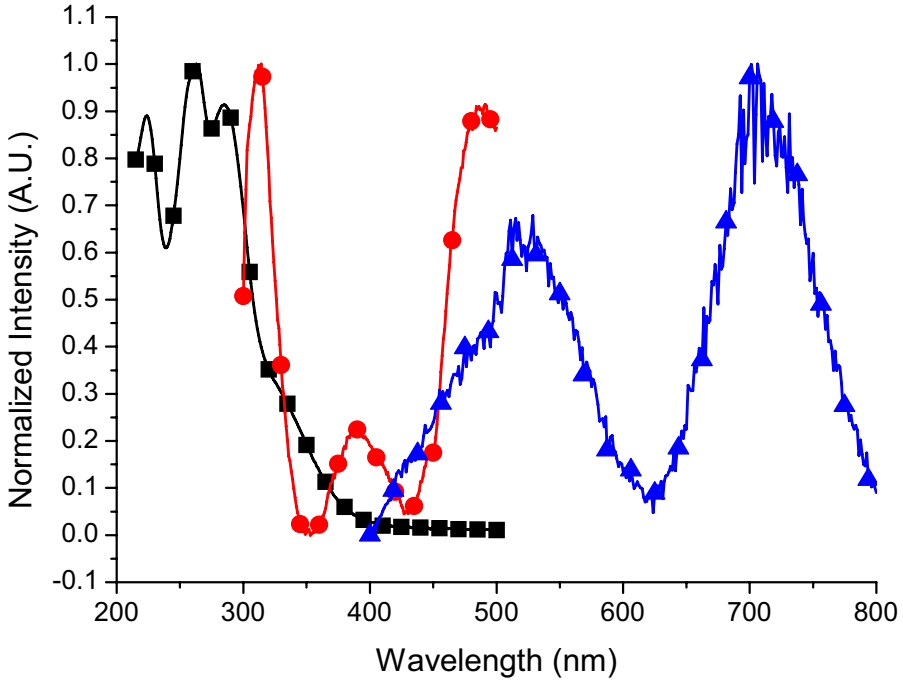

Figure A-0-4. Absorption (■), fluorescence (●) and phosphorescence (▲) spectra of **1-4**.

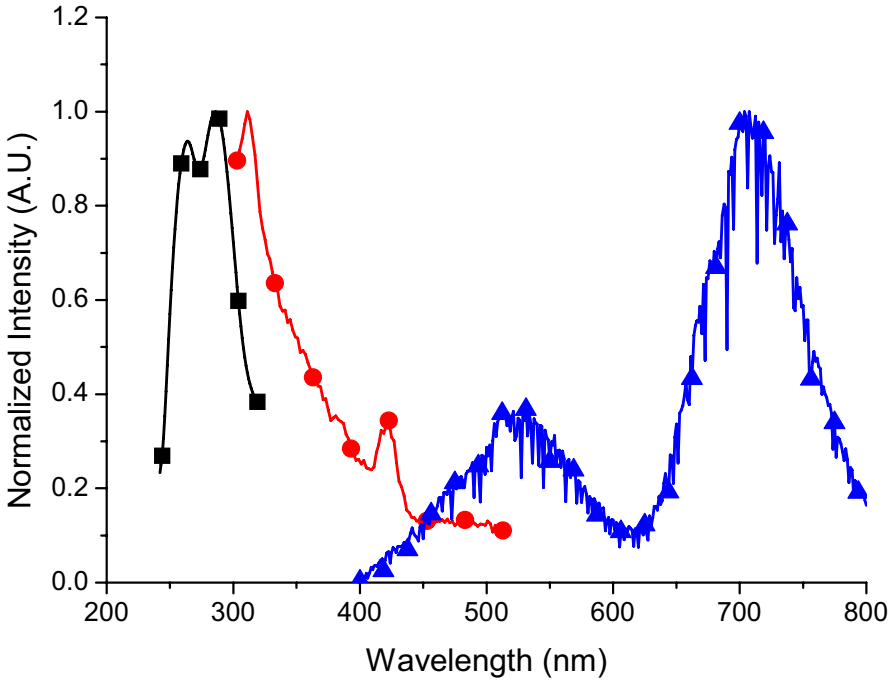

Figure A-0-5. Absorption (■), fluorescence (●) and phosphorescence (▲) spectra of **1-5**.

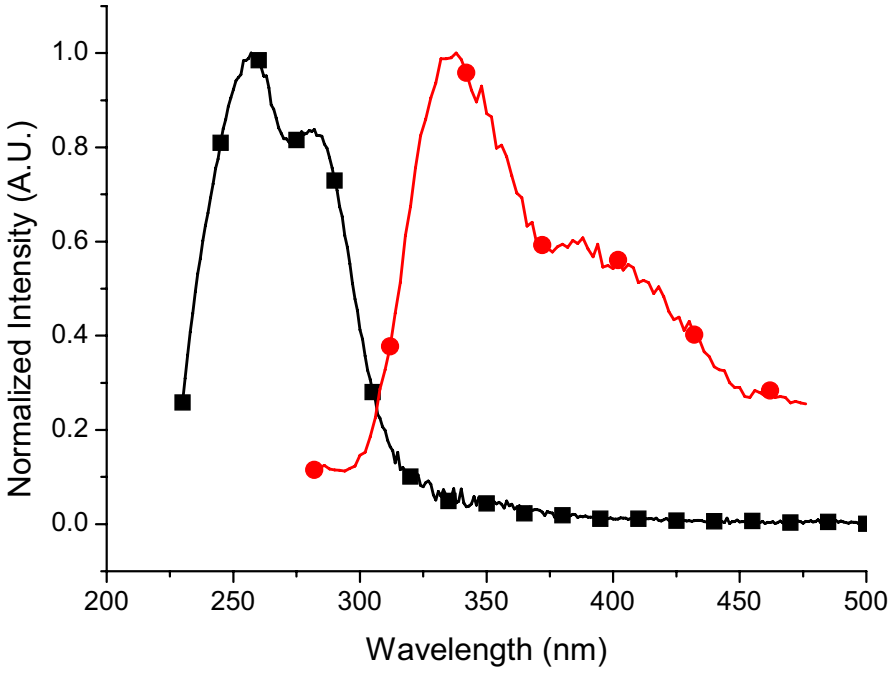

Figure A-0-6. Absorption (■), fluorescence (●) and phosphorescence (▲) spectra of **1-6**.

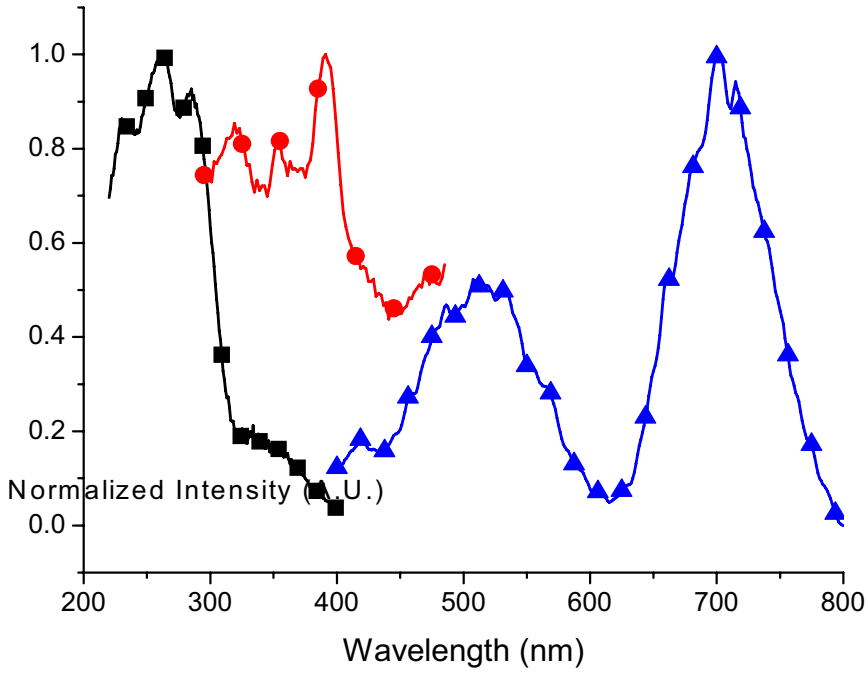

Figure A-0-7. Absorption (■), fluorescence (●) and phosphorescence (▲) spectra of **1-7**.

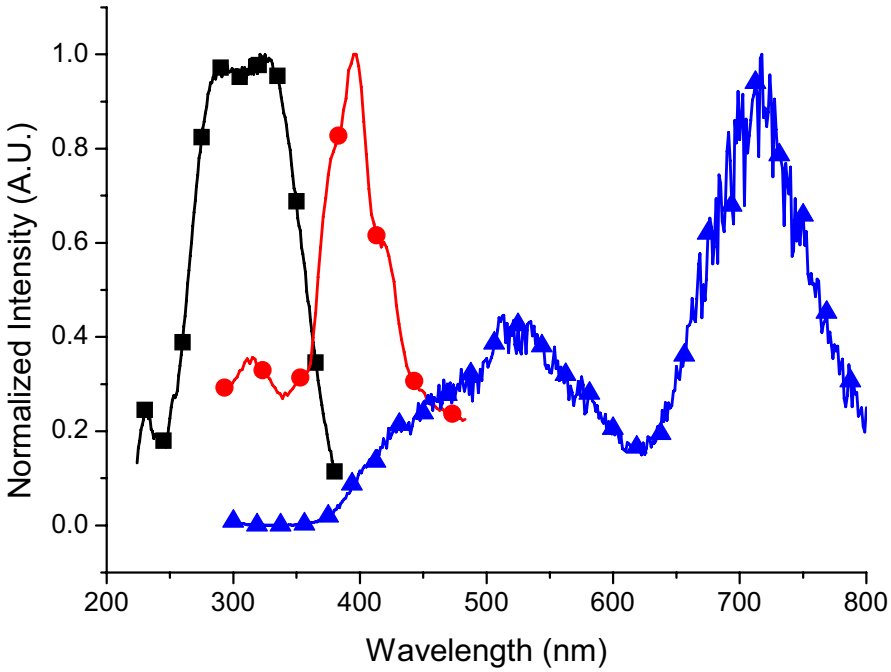

Figure A-0-8. Absorption (■), fluorescence (●) and phosphorescence (▲) spectra of **1-8**.

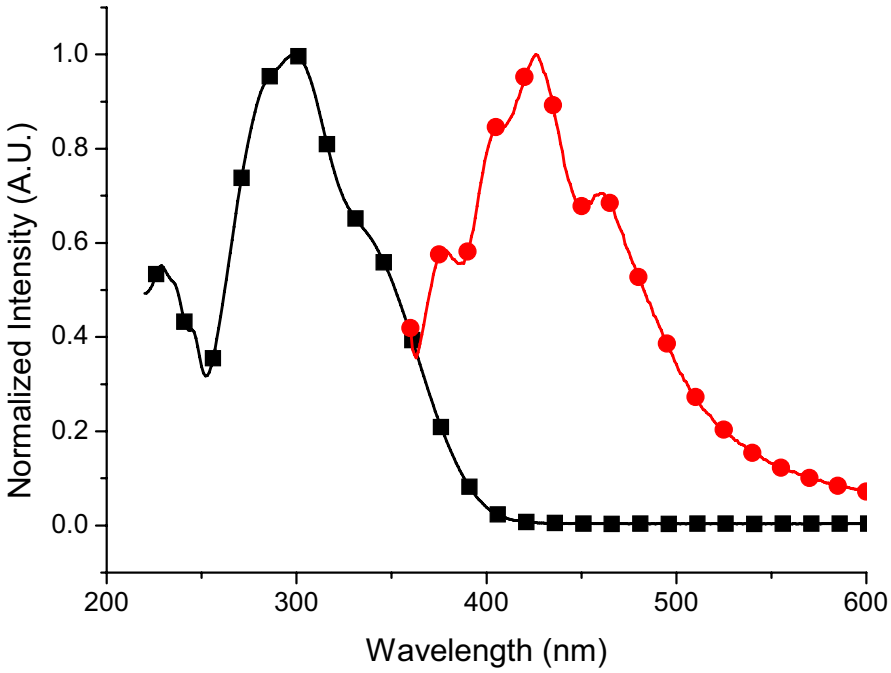

Figure A-0-9. Absorption (■) and fluorescence (●) spectra of **1-9**.

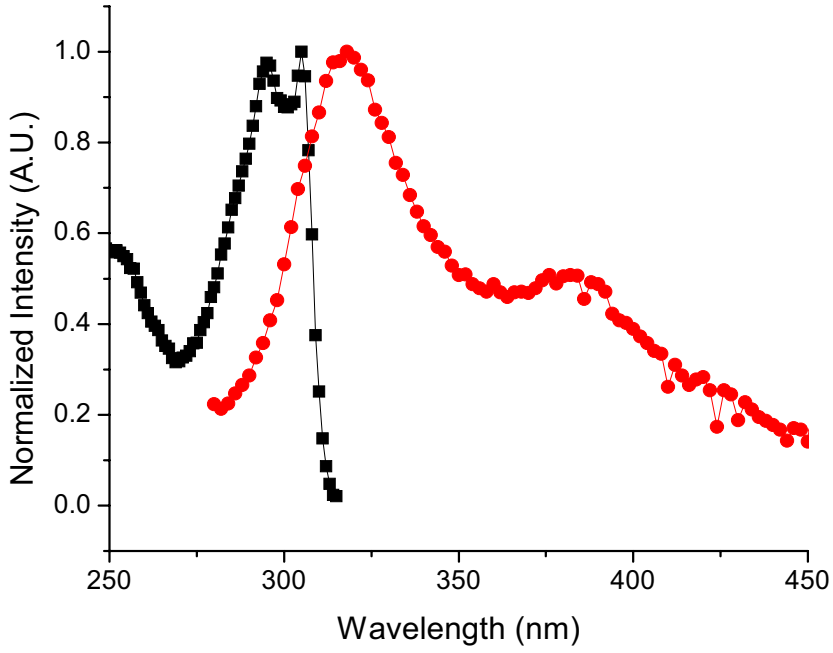

Figure A-0-10. Absorption (■) and fluorescence (●) spectra of **1-10**.

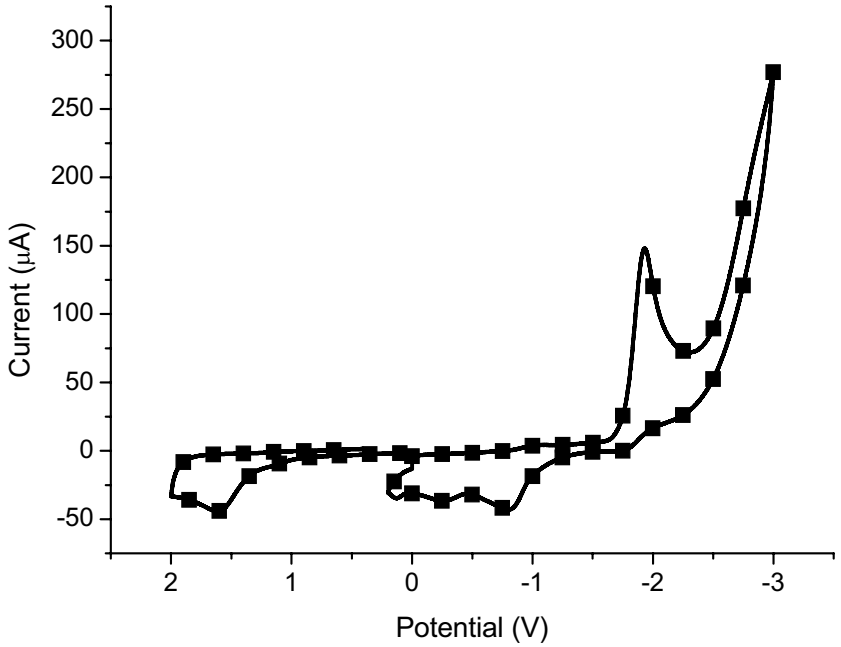

Figure A-0-11. Cyclic voltammogram of **1-1** in deaereated acetonitrile solution of 0.1 M of TBA-PF_6 using Ag/AgCl as reference and Pt as working electrodes.

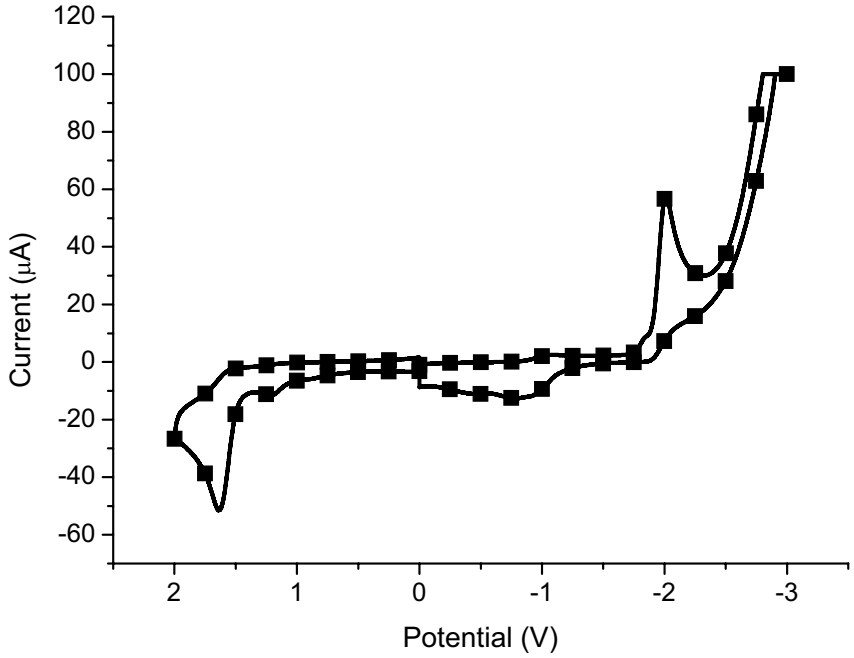

Figure A-0-12. Cyclic voltammogram of **1-2** in deaereated acetonitrile solution of 0.1 M of TBA-PF_6 using Ag/AgCl as reference and Pt as working electrodes.

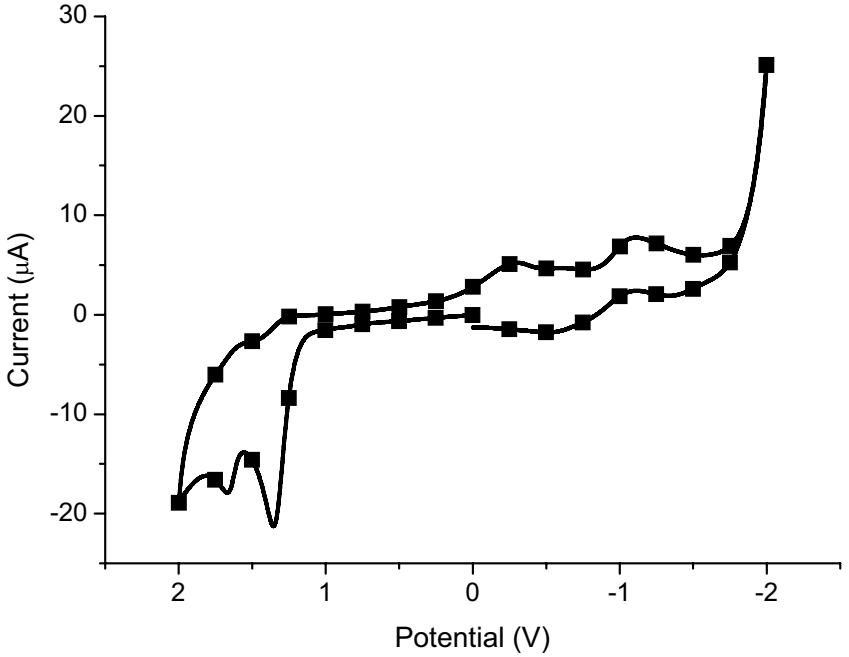

Figure A-0-13. Cyclic voltammogram of **1-3** in deaereated acetonitrile solution of 0.1 M of TBA-PF_6 using Ag/AgCl as reference and Pt as working electrodes.

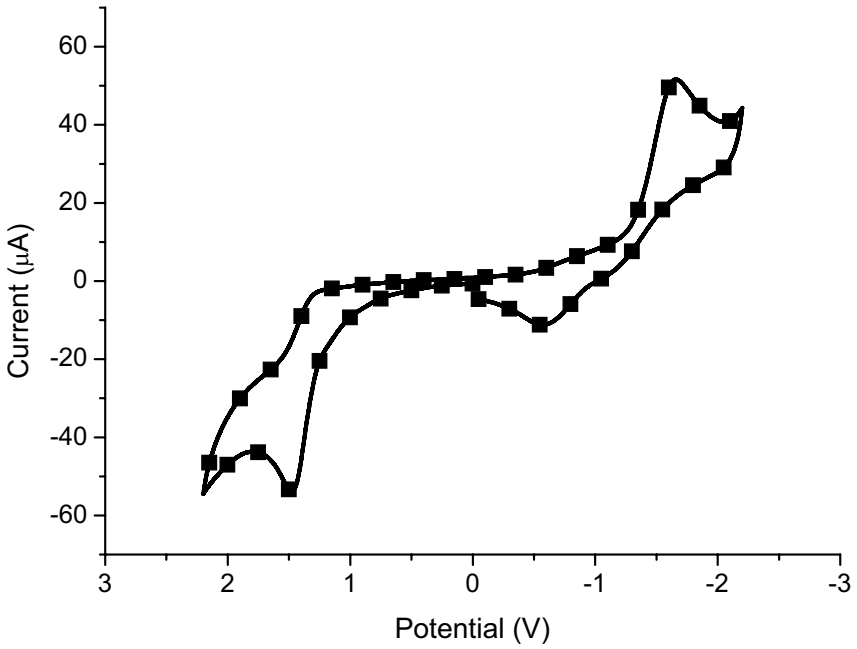

Figure A-0-14. Cyclic voltammogram of **1-4** in deaereated acetonitrile solution of 0.1 M of TBA-PF_6 using Ag/AgCl as reference and Pt as working electrodes.

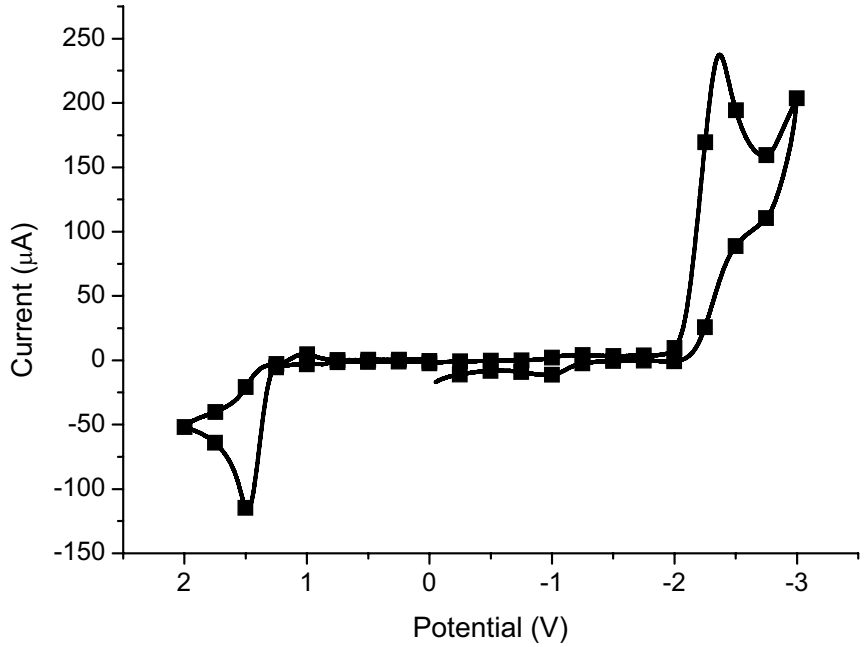

Figure A-0-15. Cyclic voltammogram of **1-5** in deaereated acetonitrile solution of 0.1 M of TBA-PF_6 using Ag/AgCl as reference and Pt as working electrodes.

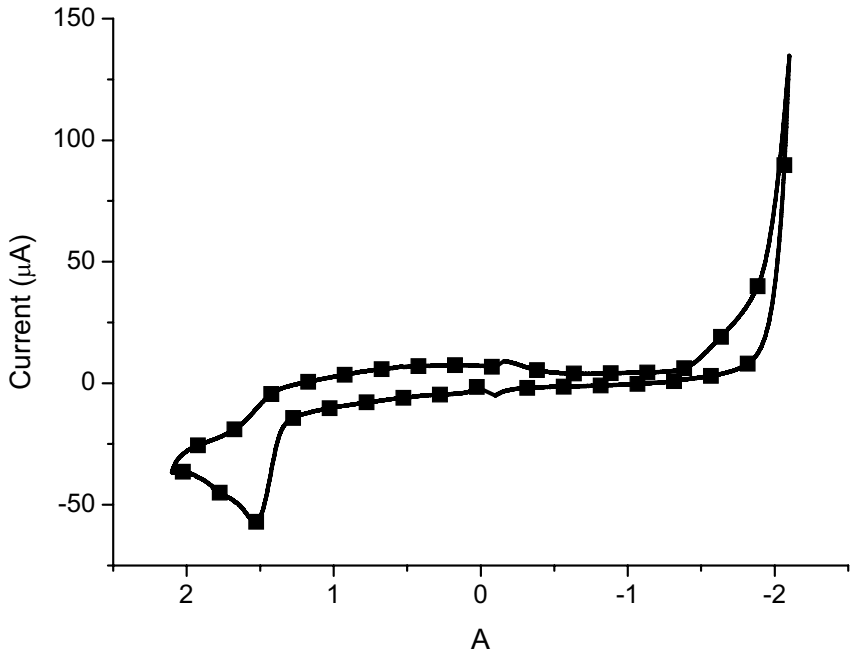

Figure A-0-16. Cyclic voltammogram of **1-6** in deaereated acetonitrile solution of 0.1 M of TBA-PF_6 using Ag/AgCl as reference and Pt as working electrodes

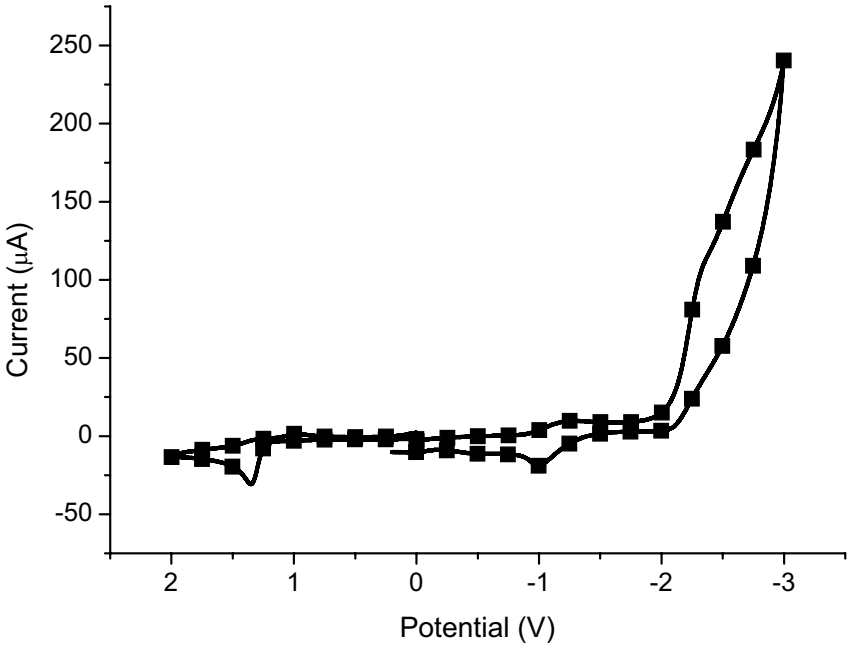

Figure A-0-17. Cyclic voltammogram of **1-7** in deaereated acetonitrile solution of 0.1 M of TBA-PF_6 using Ag/AgCl as reference and Pt as working electrodes.

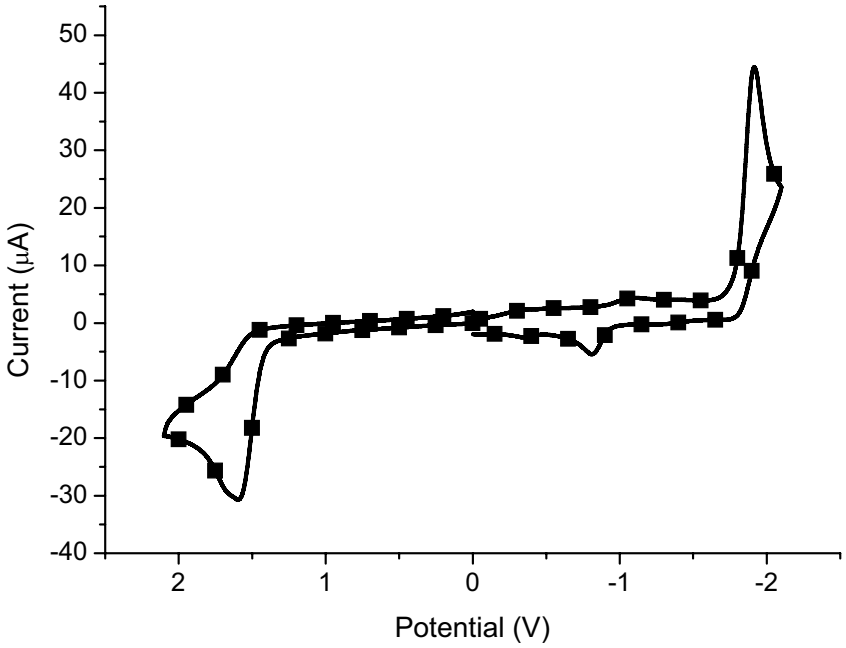

Figure A-0-18. Cyclic voltammogram of **1-8** in deaereated acetonitrile solution of 0.1 M of TBA-PF_6 using Ag/AgCl as reference and Pt as working electrodes.

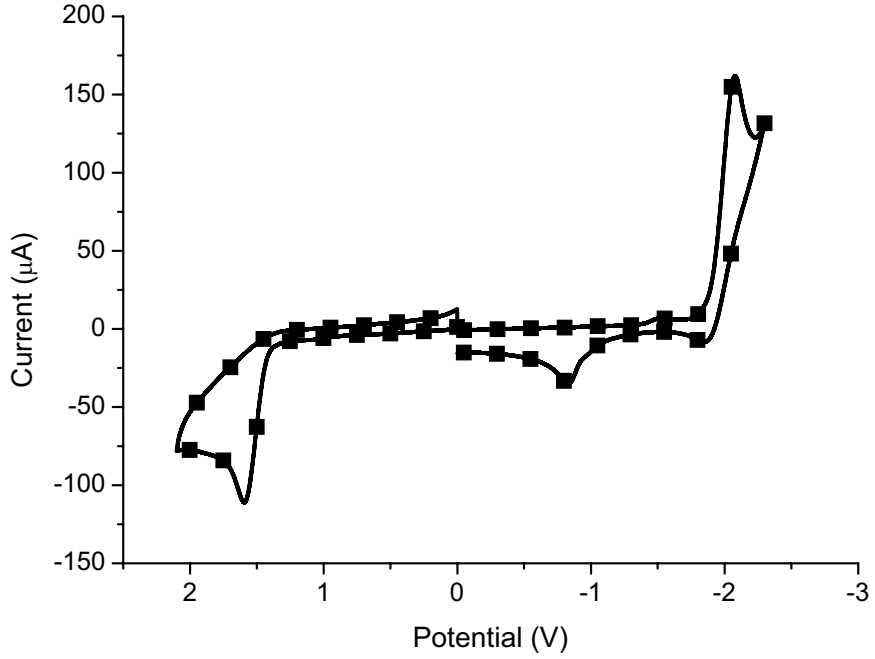

Figure A-0-19. Cyclic voltammogram of **1-9** in deaereated acetonitrile solution of 0.1 M of TBA-PF_6 using Ag/AgCl as reference and Pt as working electrodes.

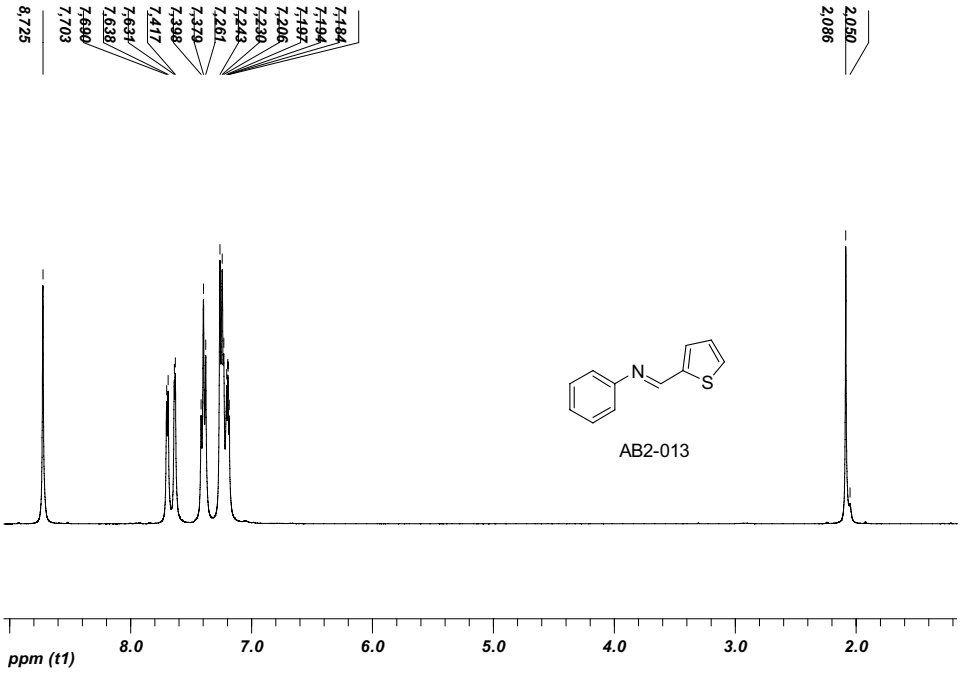

Figure A-0-20. ^{1}H Spectrum of **1-1** in deuterated acetone.

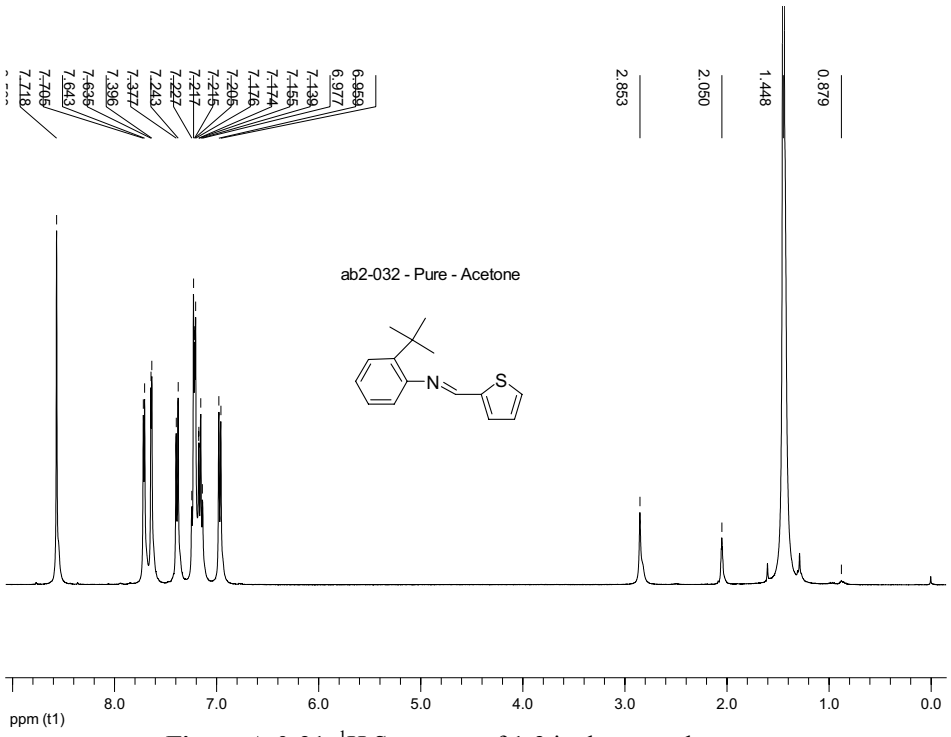

Figure A-0-21. ^{1}H Spectrum of **1-2** in deuterated acetone.

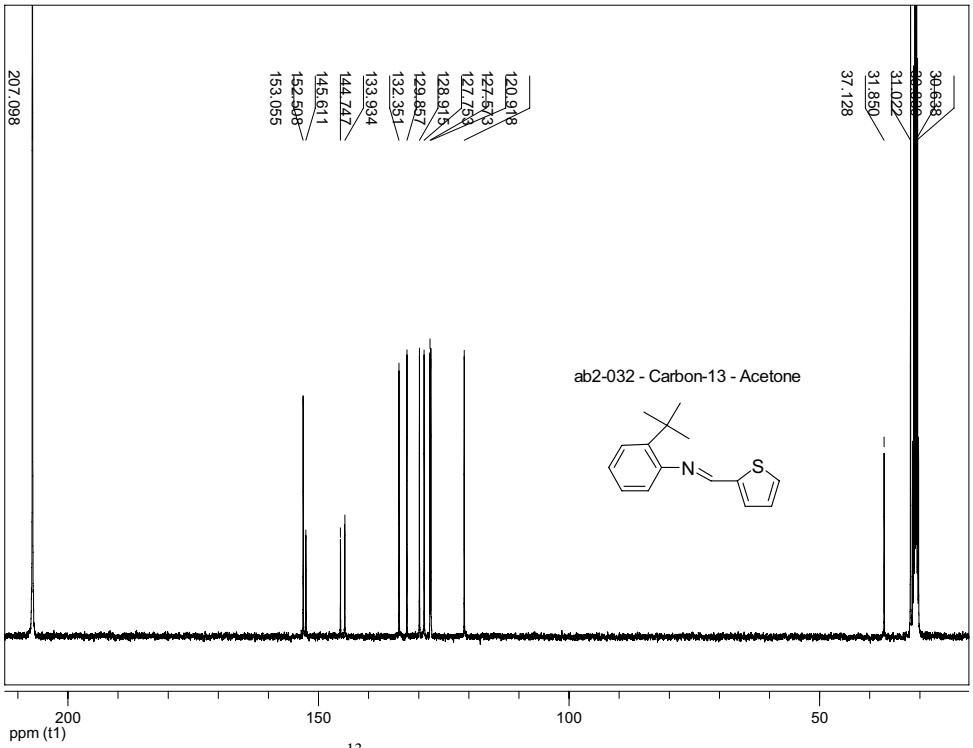

Figure A-0-22. ^{13}C Spectrum of **1-2** in deuterated acetone.

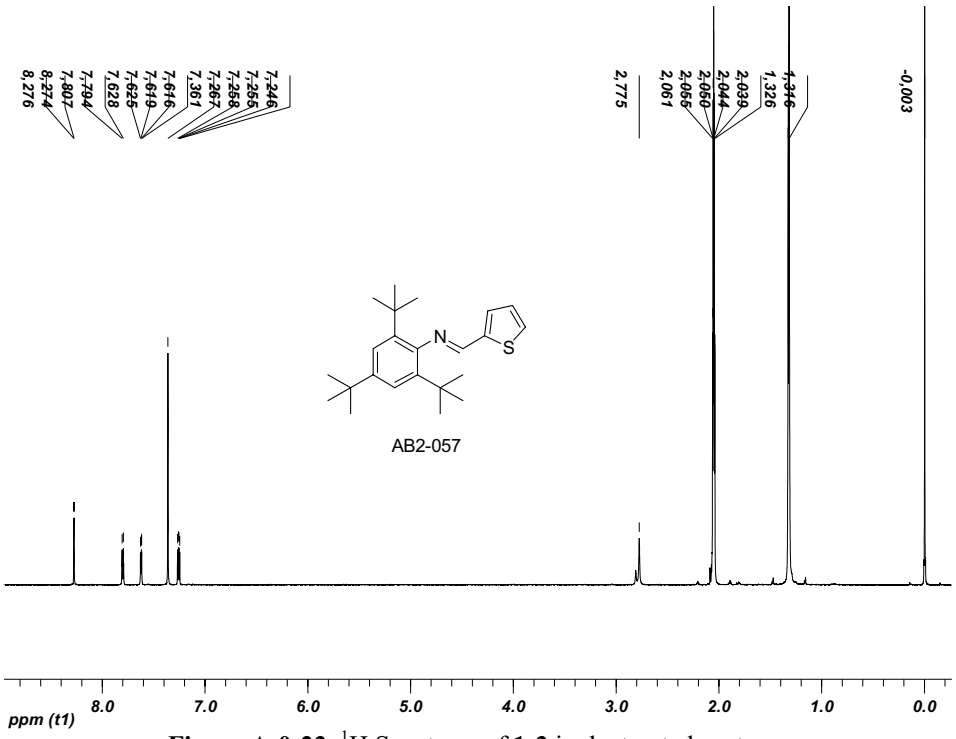

Figure A-0-23. ^{1}H Spectrum of **1-3** in deuterated acetone.

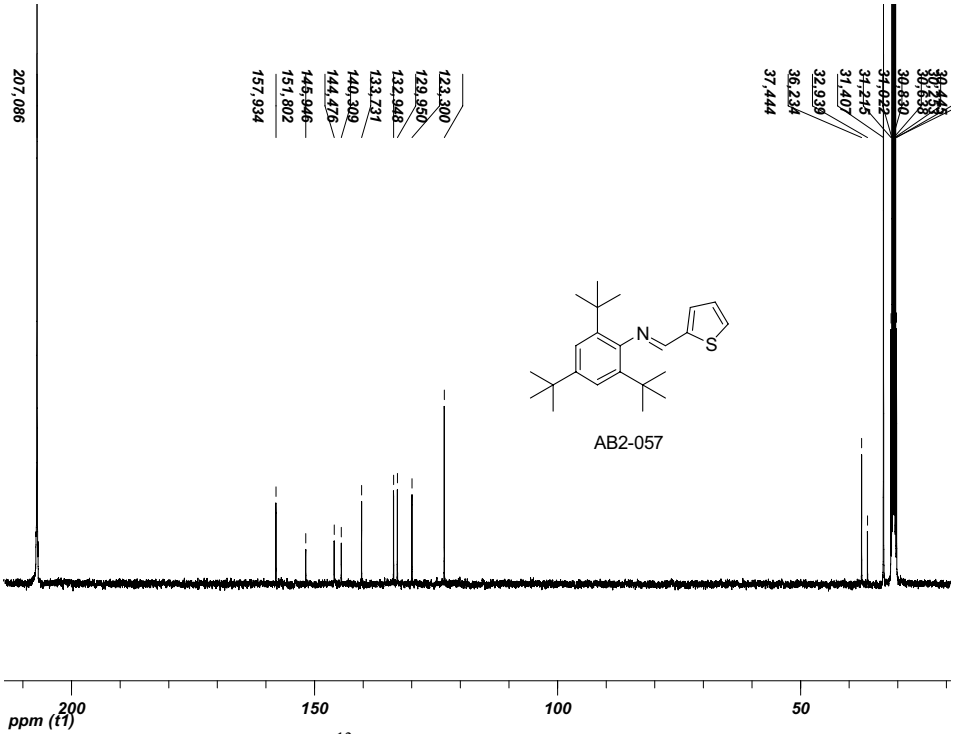

Figure A-0-24. ^{13}C Spectrum of **1-3** in deuterated acetone.

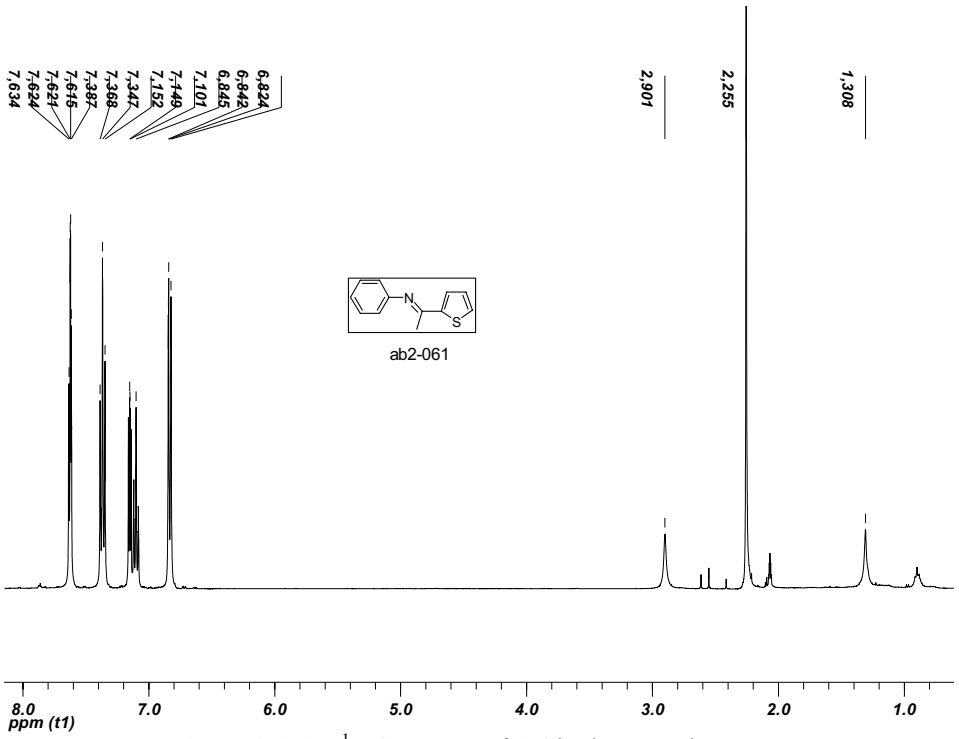

Figure A-0-25. ^{1}H Spectrum of **1-4** in deuterated acetone.

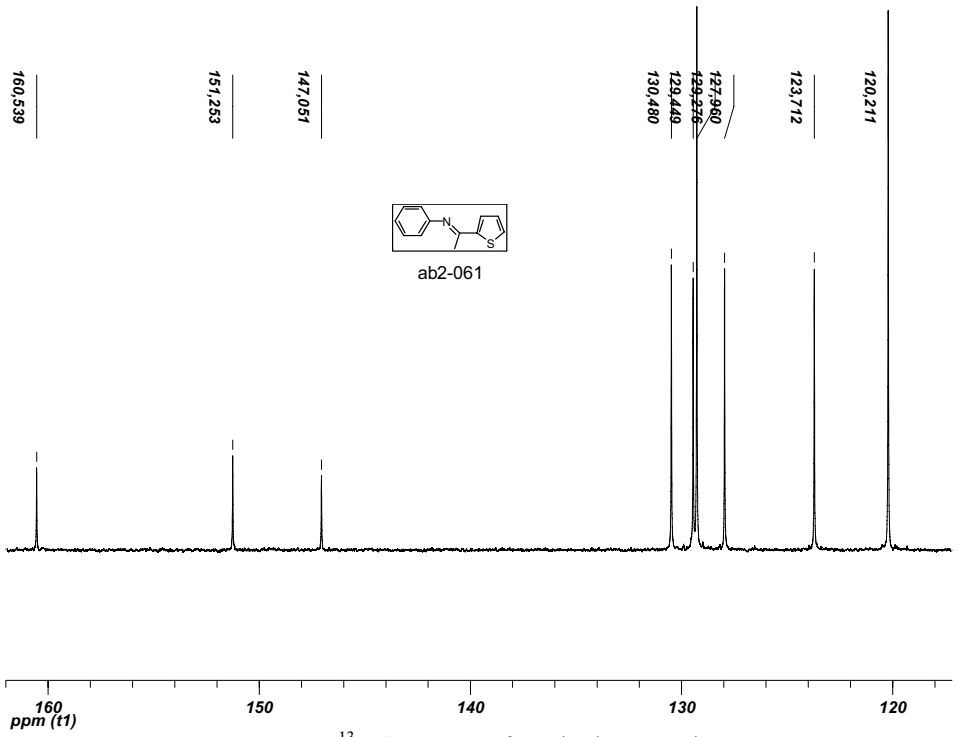

Figure A-0-26. ^{13}C Spectrum of **1-4** in deuterated acetone.

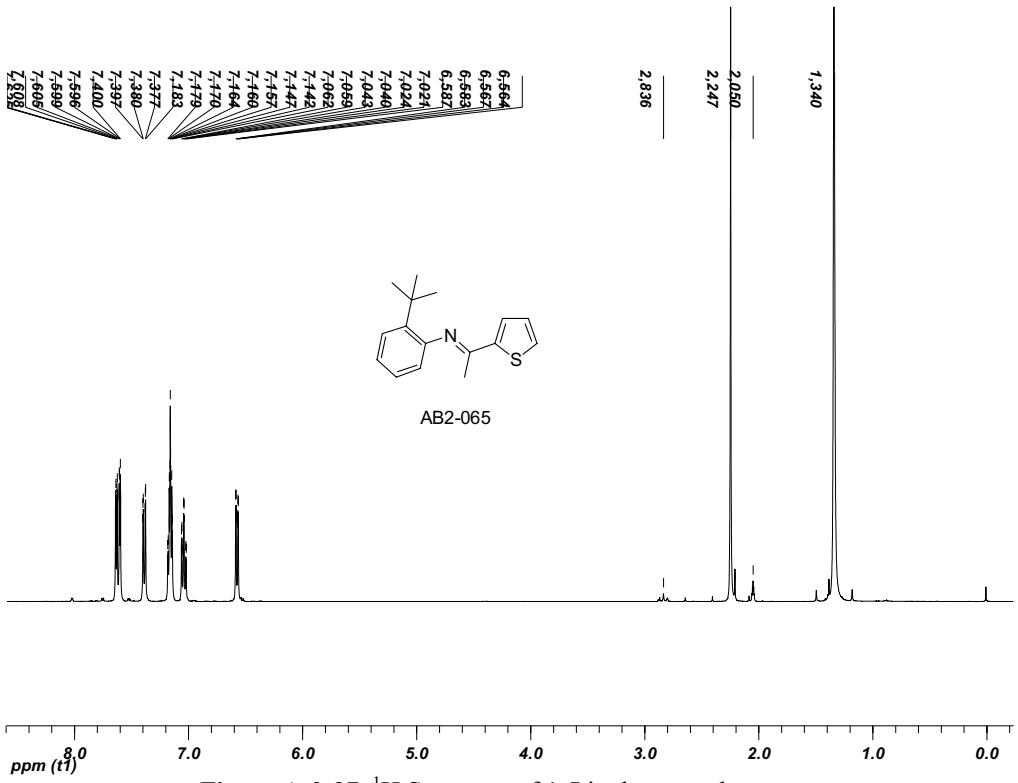

Figure A-0-27. ^{1}H Spectrum of **1-5** in deuterated acetone.

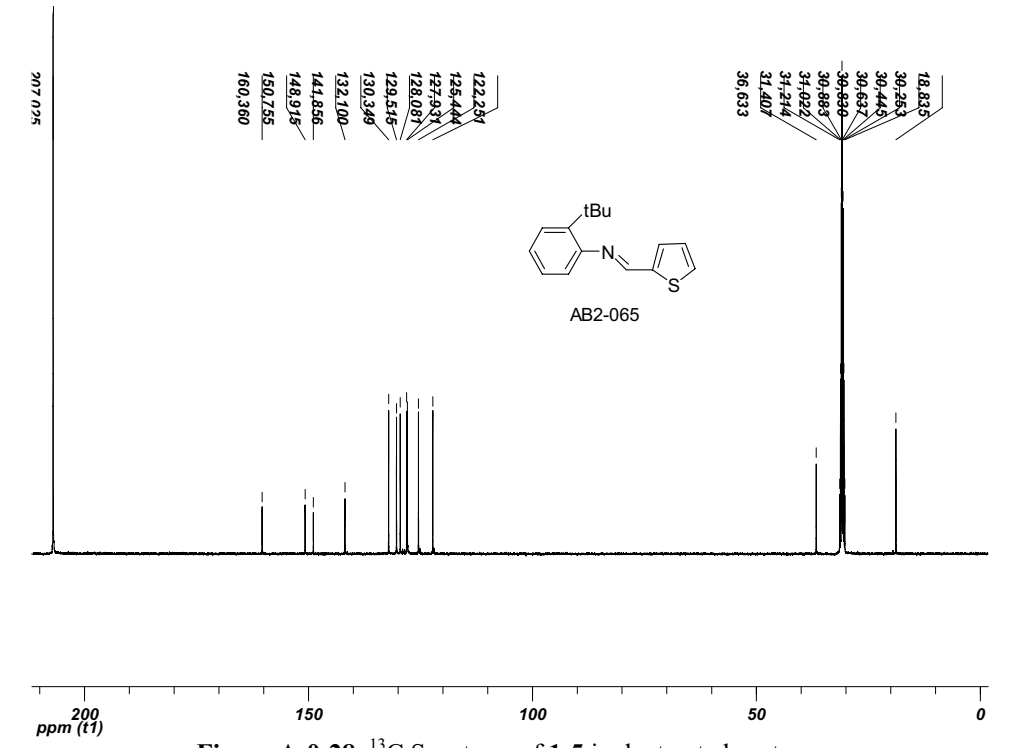

Figure A-0-28. ^{13}C Spectrum of **1-5** in deuterated acetone.

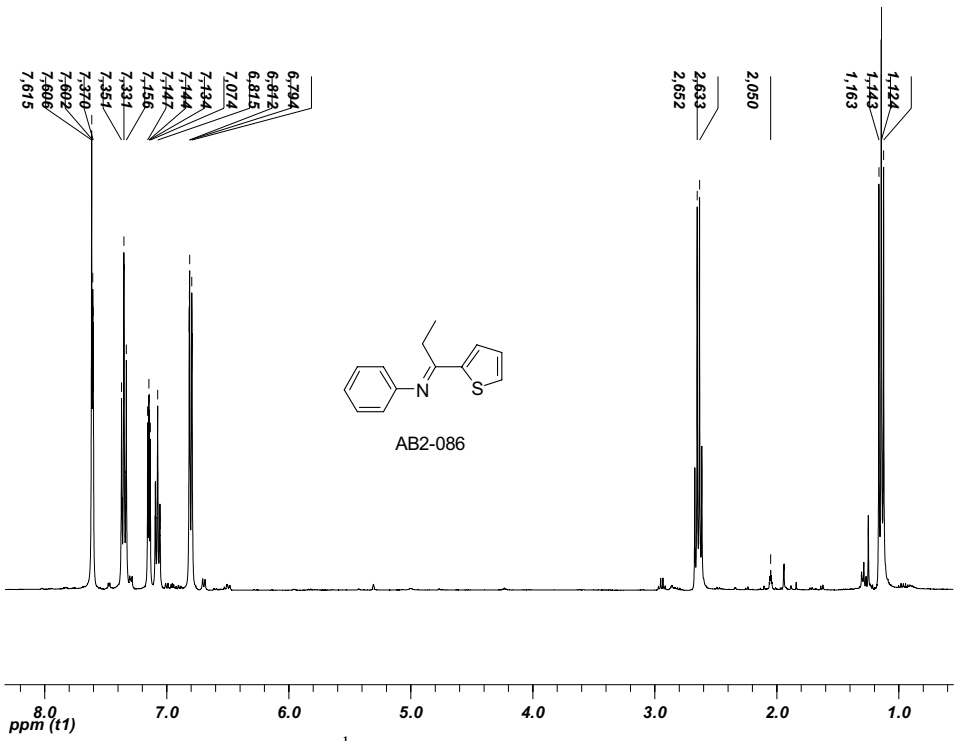

Figure A-0-29. ^{1}H Spectrum of **1-6** in deuterated acetone.

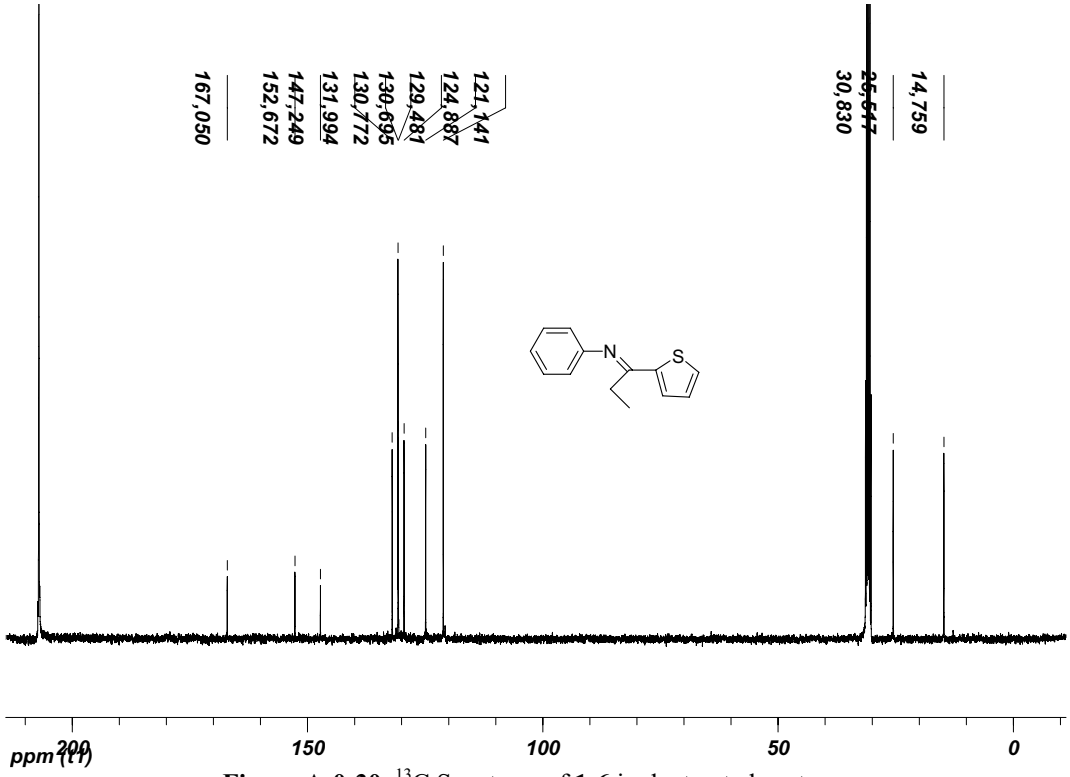

Figure A-0-30. ^{13}C Spectrum of **1-6** in deuterated acetone.

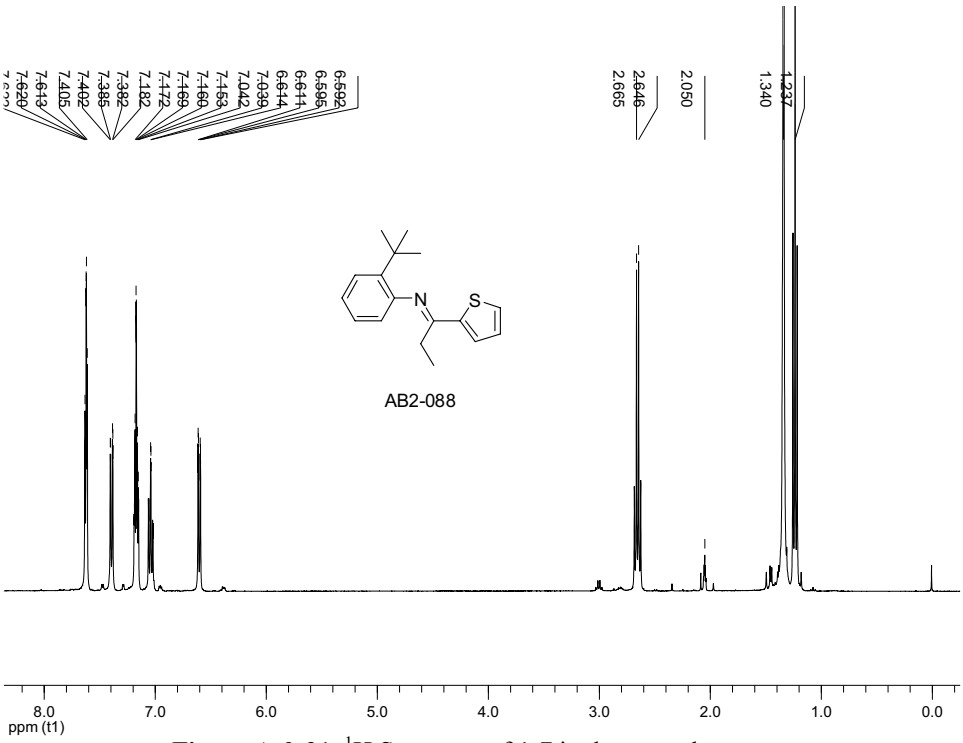

Figure A-0-31. ^{1}H Spectrum of **1-7** in deuterated acetone.

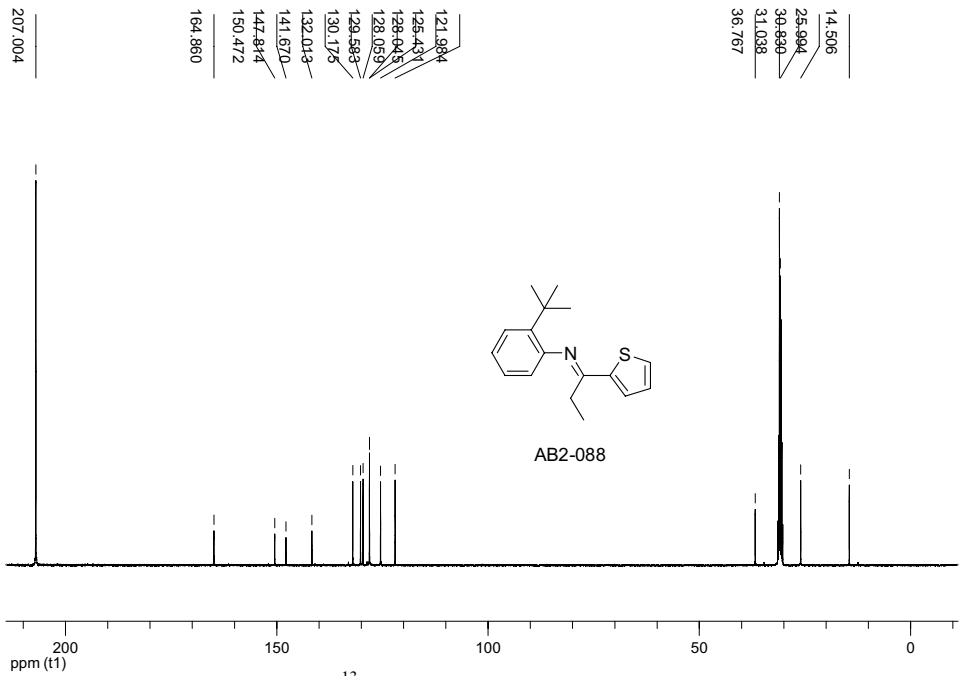

Figure A-0-32. ^{13}C Spectrum of **1-7** in deuterated acetone.

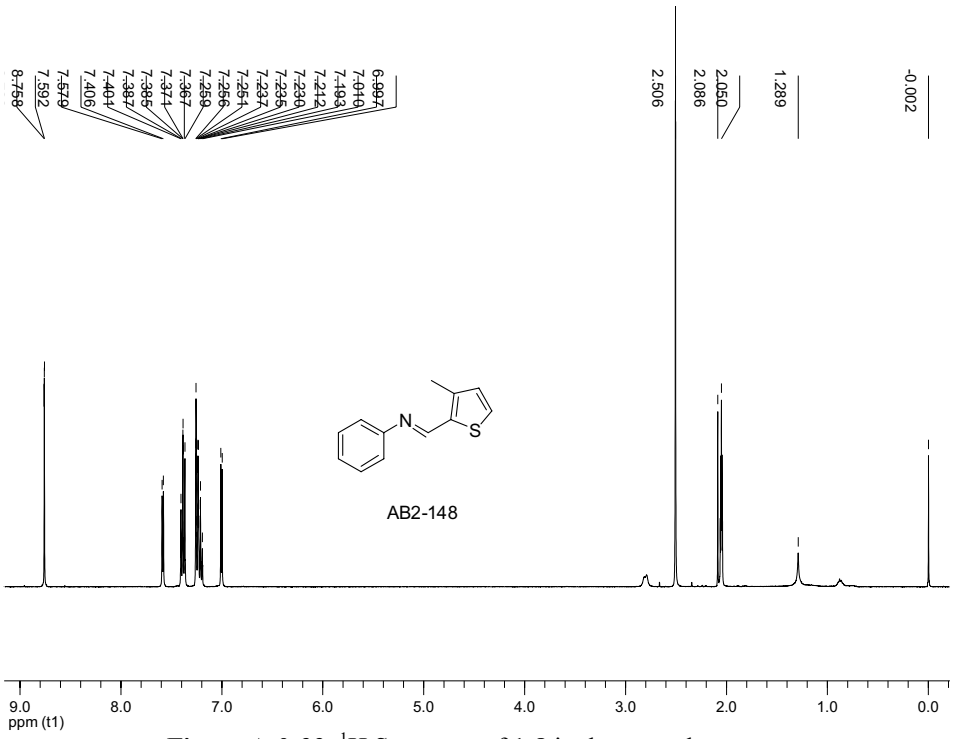

Figure A-0-33. ^{1}H Spectrum of **1-8** in deuterated acetone.

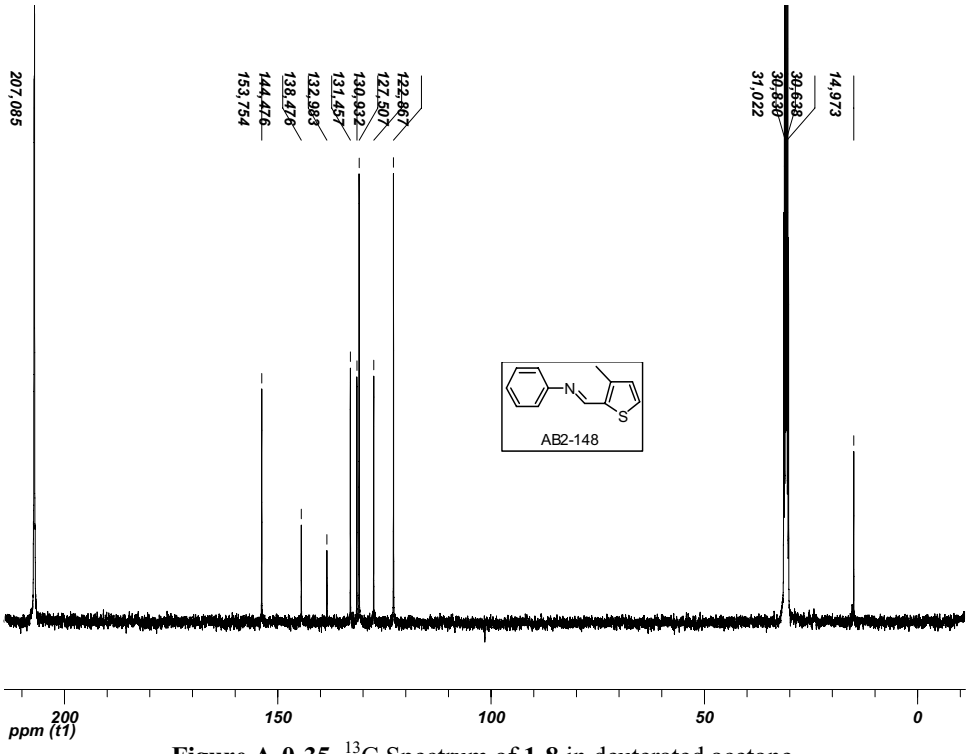

Figure A-0-35. ^{13}C Spectrum of **1-8** in deuterated acetone.

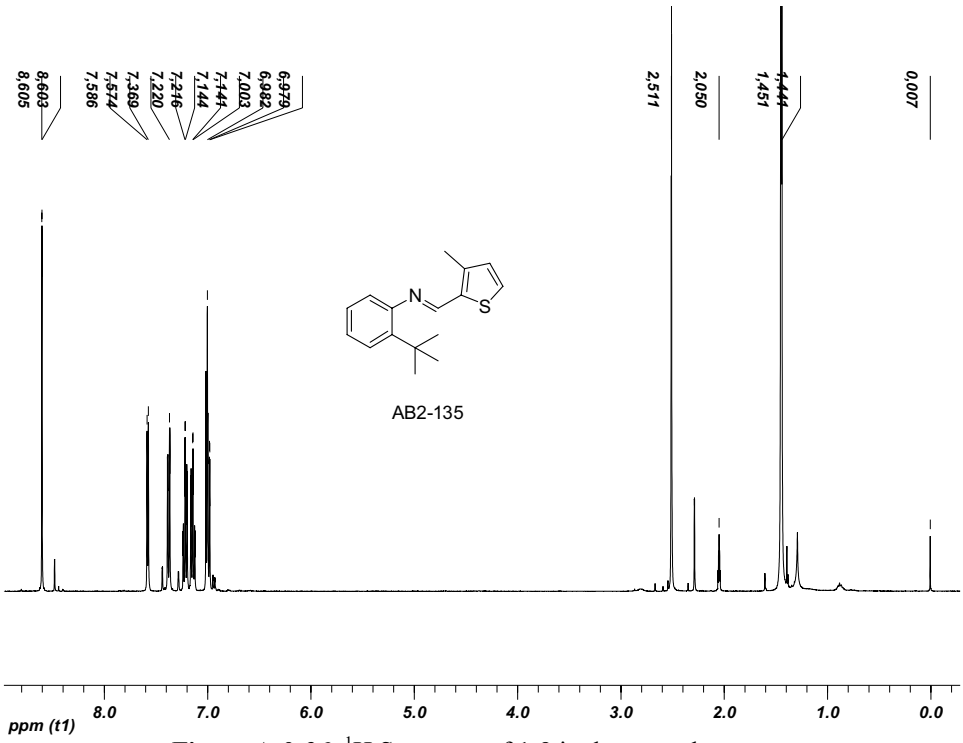

Figure A-0-36. ^{1}H Spectrum of **1-9** in deuterated acetone.

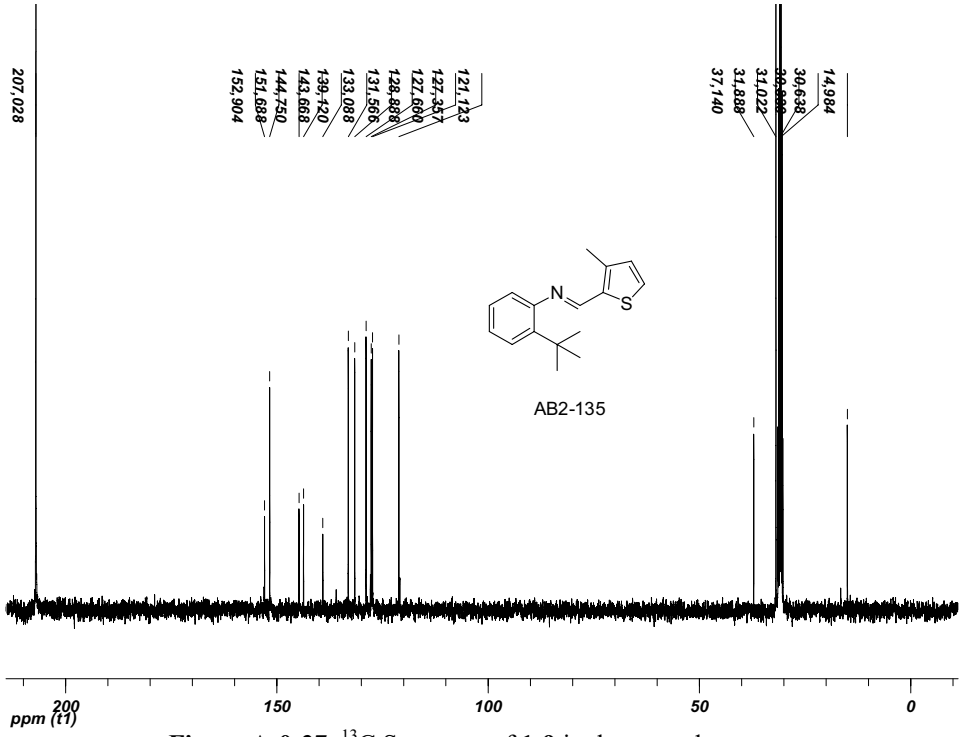

Figure A-0-37. ^{13}C Spectrum of **1-9** in deuterated acetone.

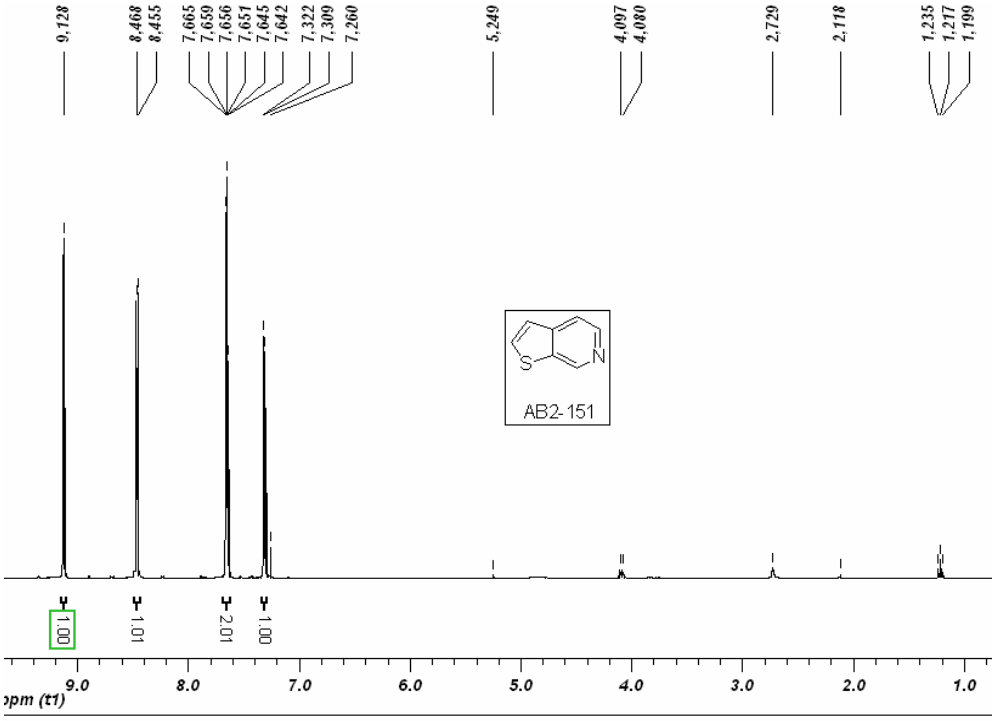

Figure A-0-38. ^{1}H Spectrum of **1-10** in deuterated chloroform.

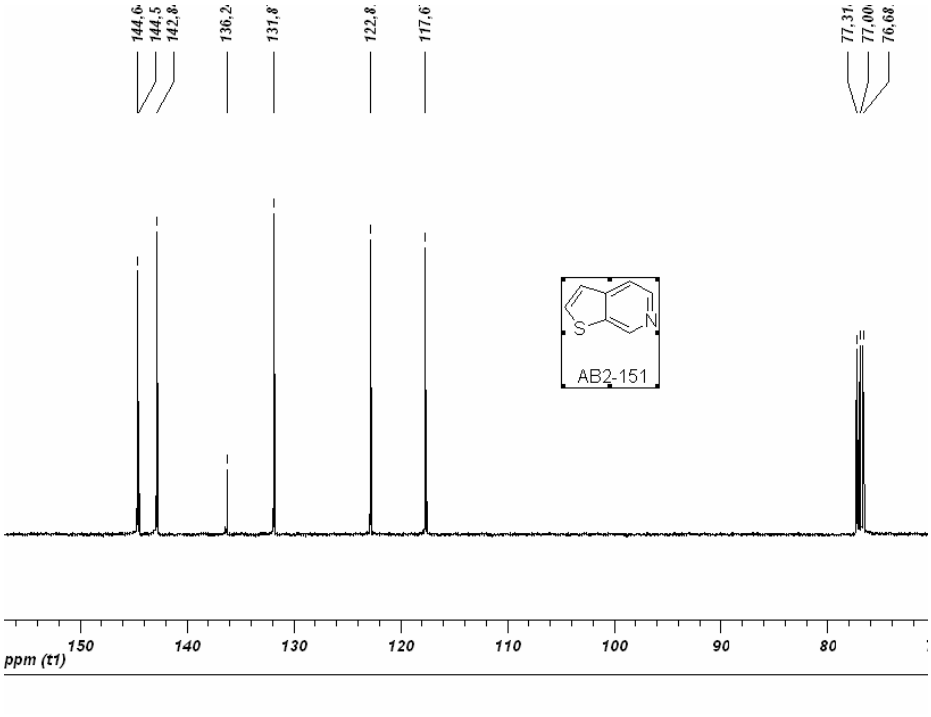

Figure A-0-39. ^{13}C Spectrum of **1-10** in deuterated chloroform

Appendix B

Chapter 2: Synthesis and Characterization of Thiophene Azomethine Metal Complexes

Supporting Information

Table of Figures

Figure B-1. ^{1}H NMR of **2-1** in deuterated acetone. XXIV
Figure B-2. ^{13}C NMR of **2-1** in deuterated acetone. XXIV
Figure B-3. ^{1}H NMR of **2-2** in deuterated methanol.....XXV
Figure B-4. ^{13}C NMR of **2-2** in deuterated methanol. XXV
Figure B-5. ^{1}H NMR of ligand $\mathbf{L_1}$ in deuterated acetone..... XXVI
Figure B-6. ^{1}H NMR of ligand $\mathbf{L_2}$ in deuterated acetone..... XXVI
Figure B-7. ^{1}H NMR of ligand $\mathbf{L_3}$ in deuterated acetone.....XXVII
Figure B-8. ^{1}H NMR of ligand $\mathbf{L_4}$ in deuterated acetone.....XXVII
Figure B-9. ^{13}C NMR of $\mathbf{L_4}$ in deuterated acetone. XXVIII
Figure B-10. ^{1}H NMR of ligand $\mathbf{L_5}$ in deuterated acetone.....XXVIII
Figure B-11. ^{13}C NMR of $\mathbf{L_5}$ in deuterated acetone. XXIX
Figure B-12. Cyclic voltammograms of the ligand L_4 (bottom) and 8-hydroxyquinoline (top) demonstrating the change in oxidation and reduction potential upon the addition of the thiophene azomethine moiety. Measurements were recorded in acetonitrile solution containing 0.1 M $N(Bu)_4PF_6$ as supporting electrolyte at a scan rate of 100 mV/s.....XXX
Figure B-13. Normalized absorbance (●) and emission spectra (■) of $\mathbf{L_5}$ as measured in deaerated acetonitrile. XXXI
Figure B-14. Cyclic voltammogram of $\mathbf{L_5}$ in deaereated acetonitrile solution of 0.1 M of TBA-PF_6 using Ag/AgCl as reference and Pt as working electrodes. XXXI

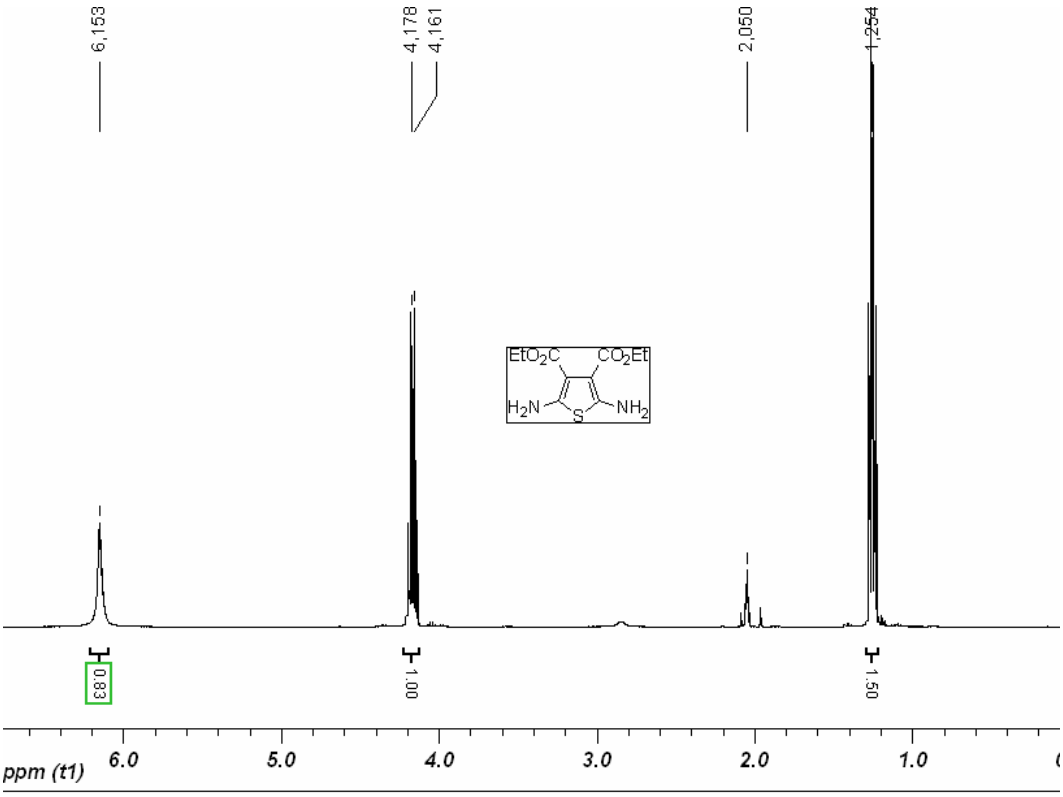

Figure B-1. ^{1}H NMR of **2-1** in deuterated acetone.

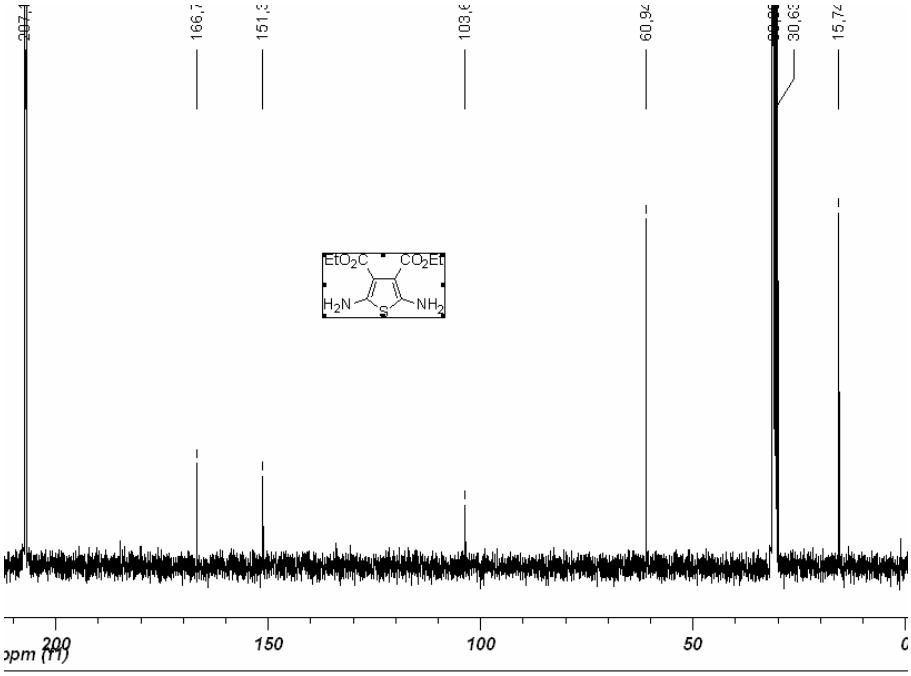

Figure B-2. ^{13}C NMR of **2-1** in deuterated acetone.

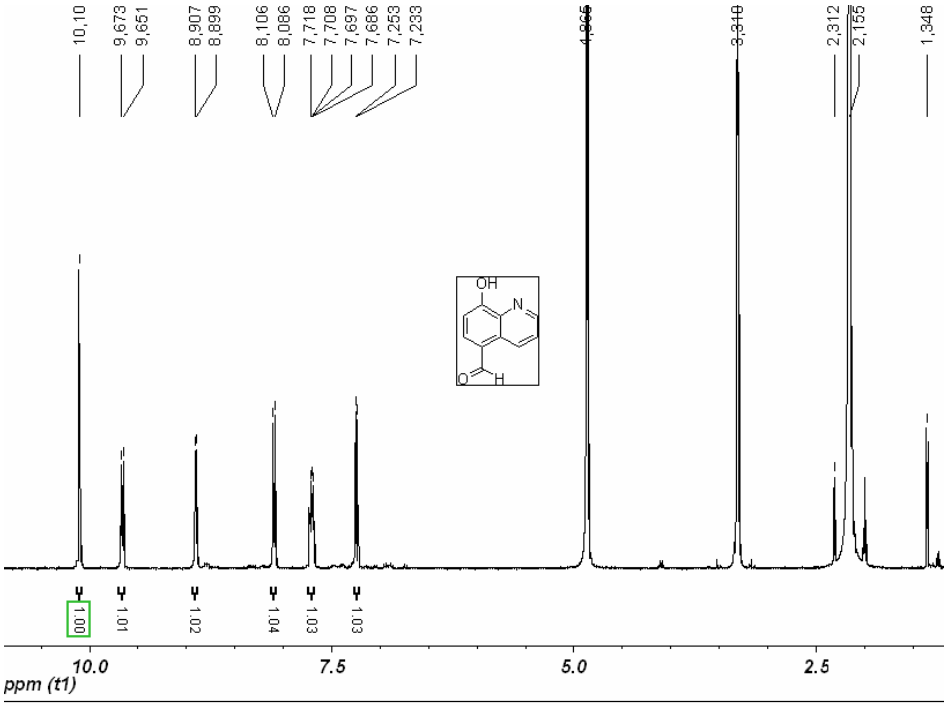

Figure B-3. ^{1}H NMR of **2-2** in deuterated methanol.

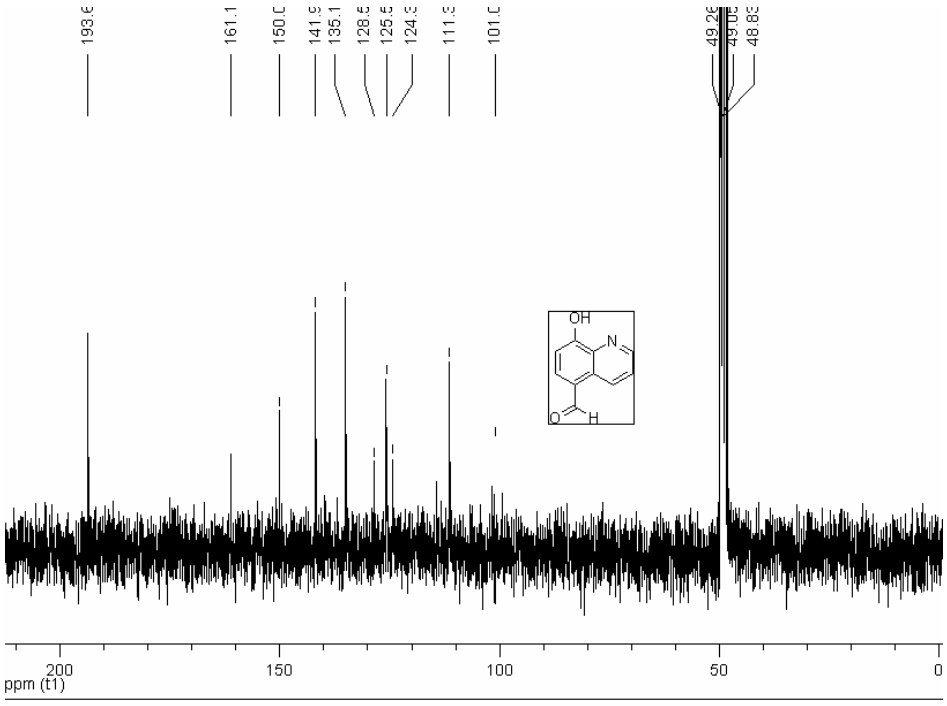

Figure B-4. ^{13}C NMR of **2-2** in deuterated methanol.

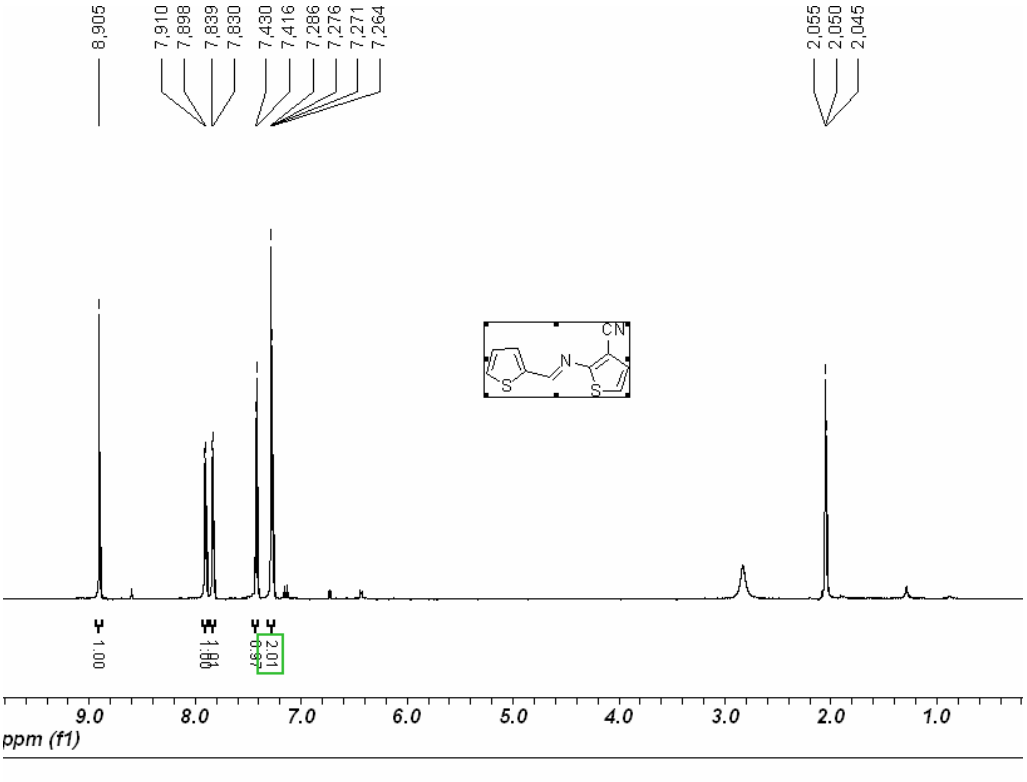

Figure B-5. ^{1}H NMR of ligand $\mathbf{L_1}$ in deuterated acetone.

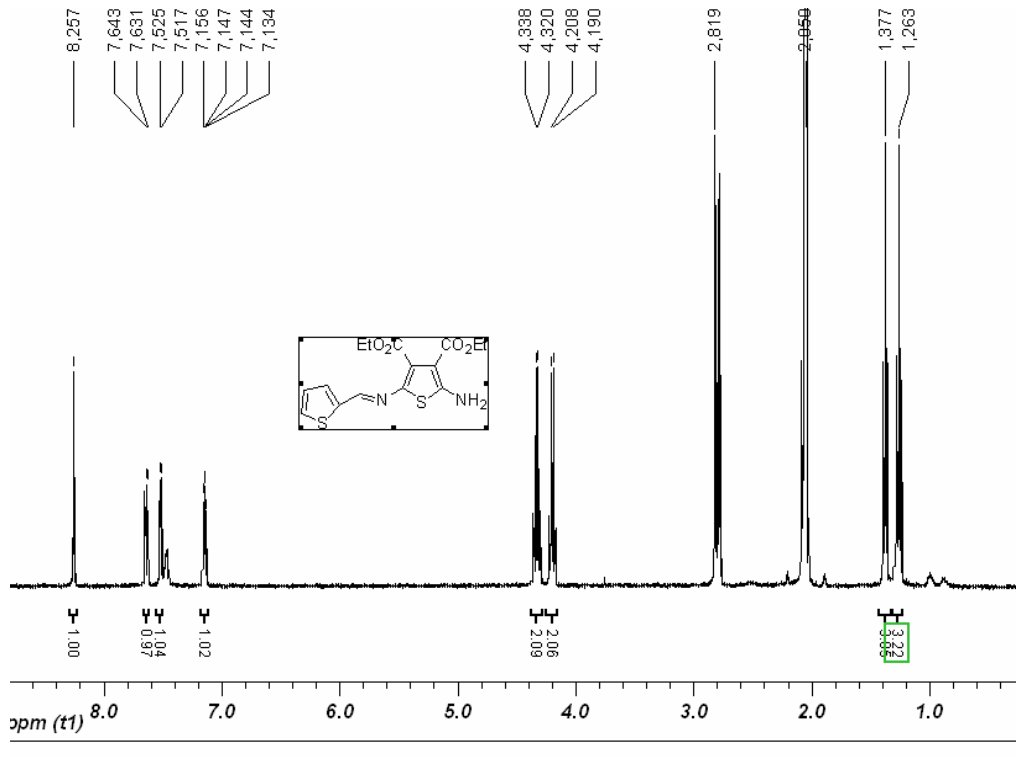

Figure B-6. ^{1}H NMR of ligand $\mathbf{L_2}$ in deuterated acetone.

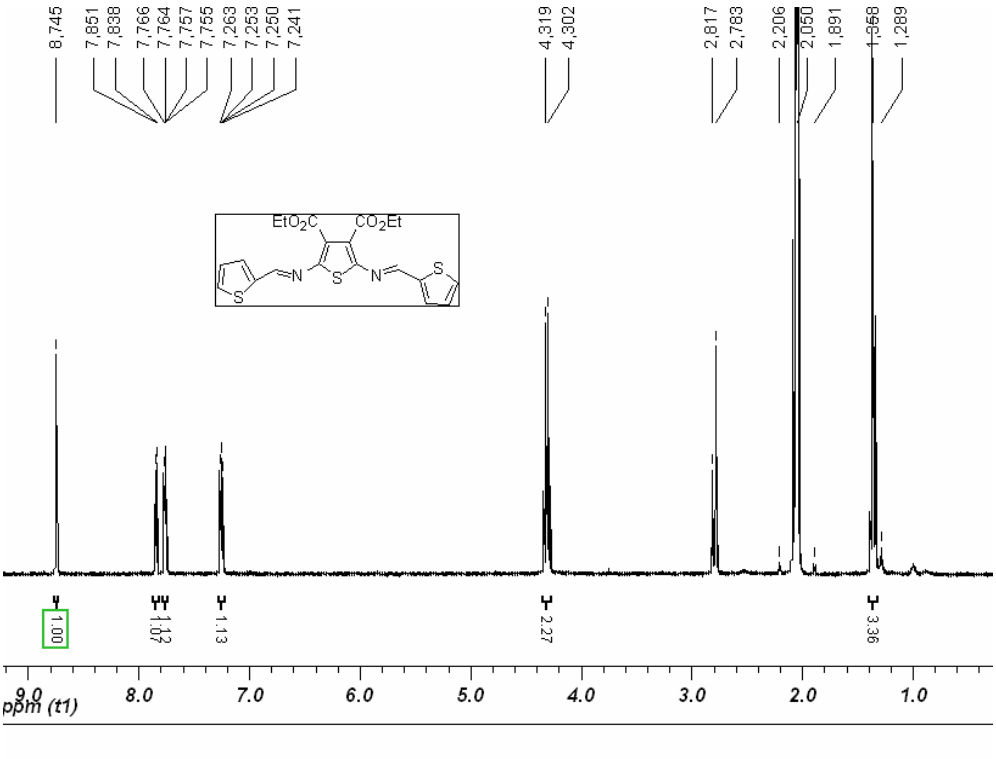

Figure B-7. ^{1}H NMR of ligand $\mathbf{L_3}$ in deuterated acetone.

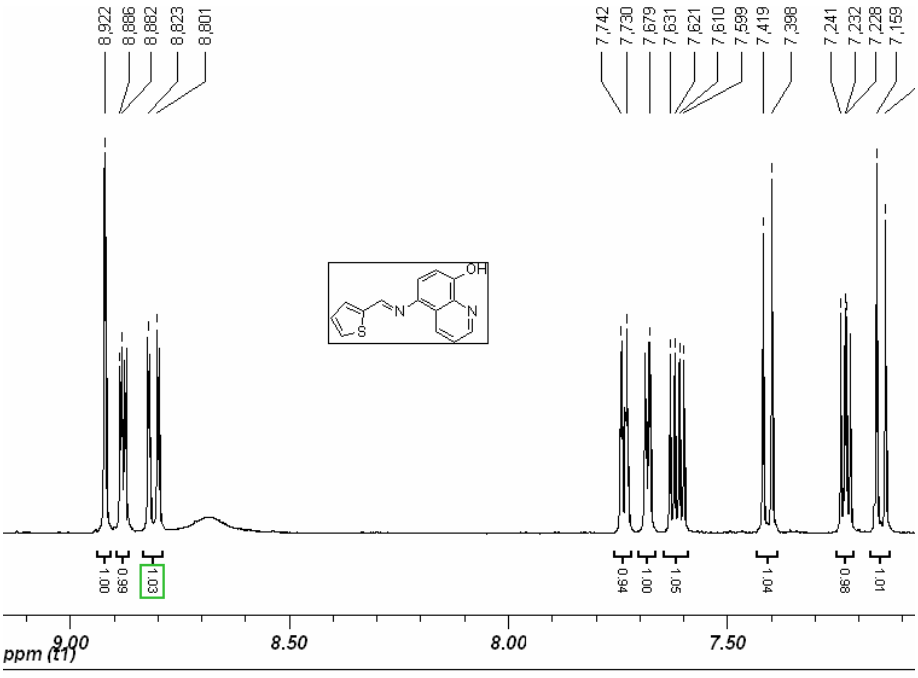

Figure B-8. ^{1}H NMR of ligand $\mathbf{L_4}$ in deuterated acetone.

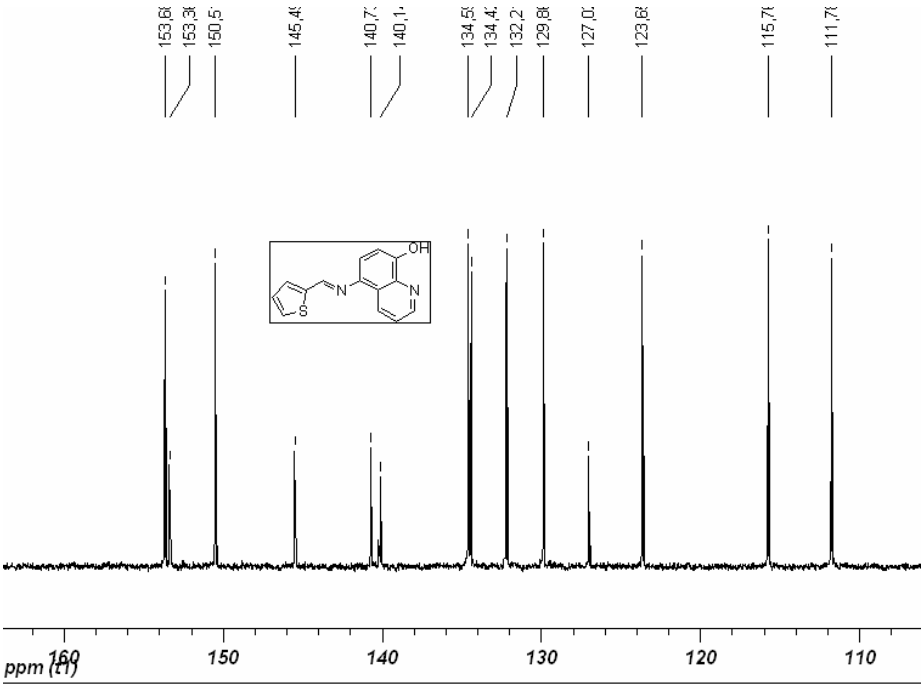

Figure B-9. ^{13}C NMR of $\mathbf{L_4}$ in deuterated acetone.

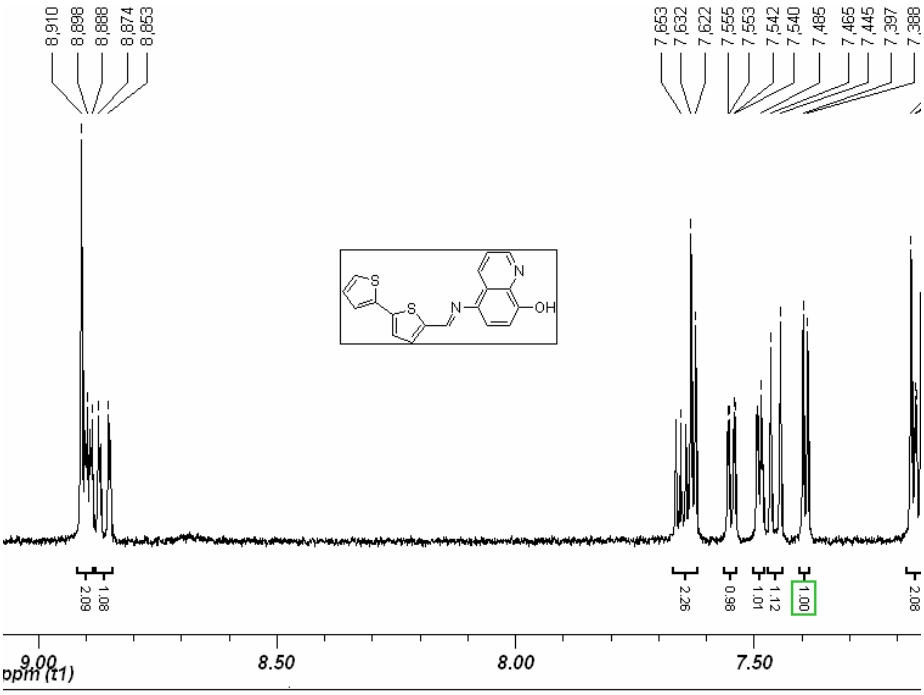

Figure B-10. ^{1}H NMR of ligand $\mathbf{L_5}$ in deuterated acetone.

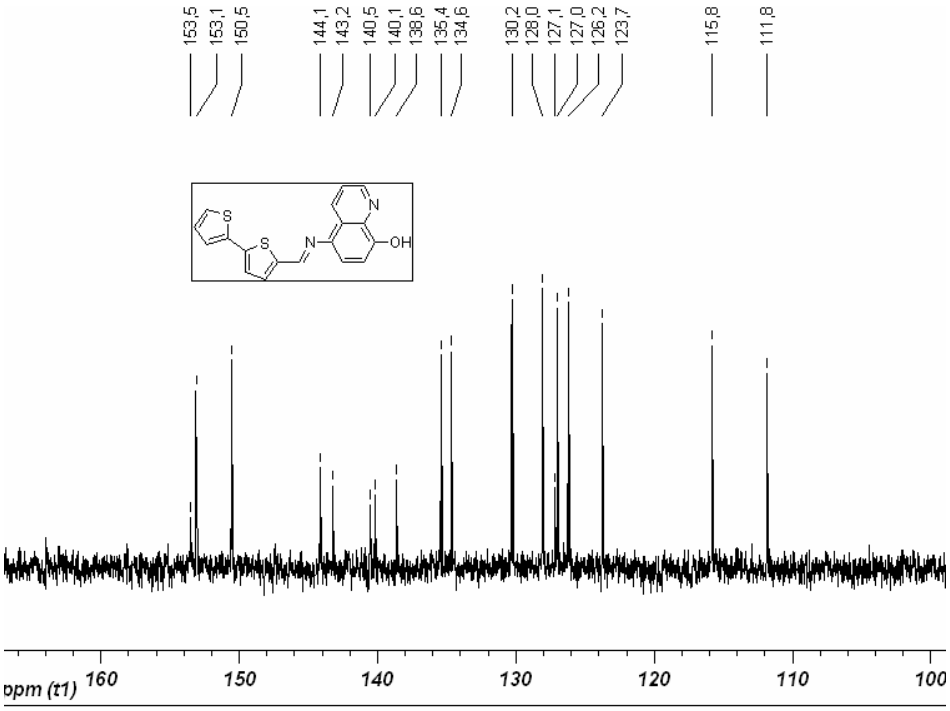

Figure B-11. ^{13}C NMR of $\mathbf{L_5}$ in deuterated acetone.

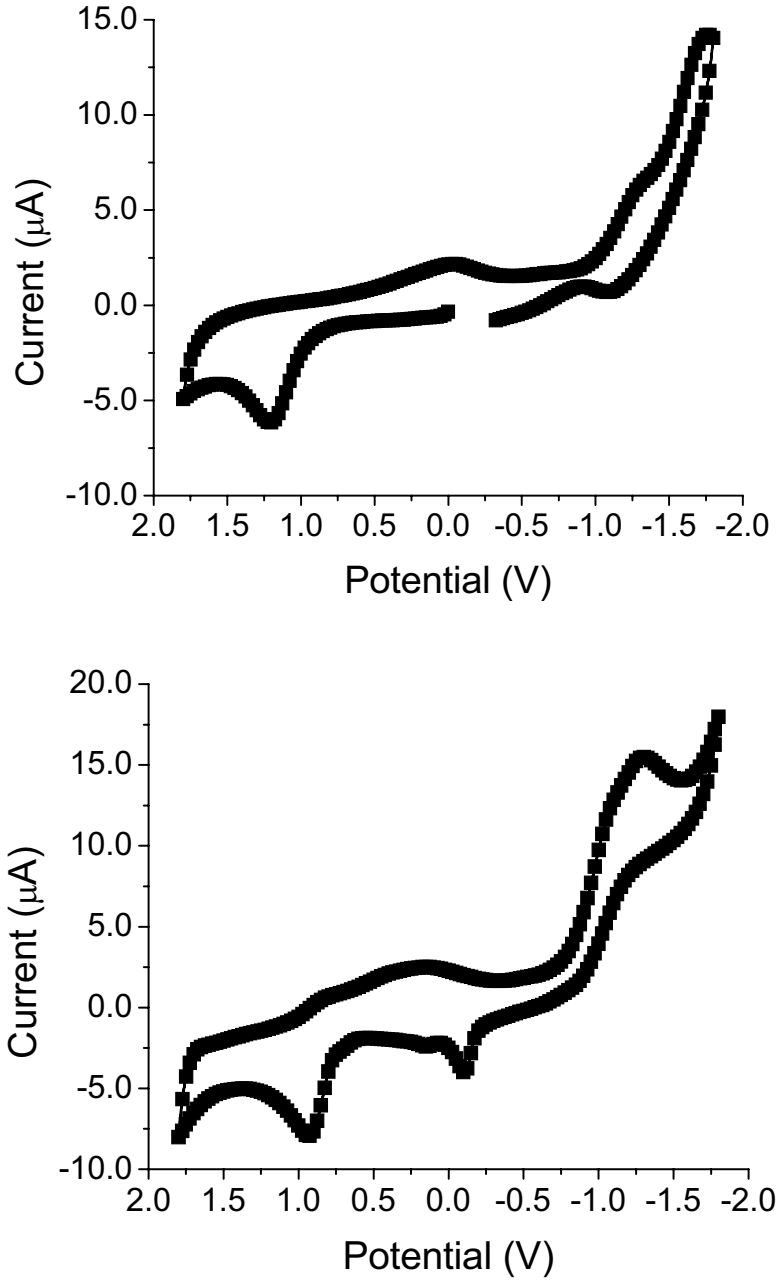

Figure B-12. Cyclic voltammograms of the ligand $\mathbf{L_4}$ (bottom) and 8-hydroxyquinoline (top) demonstrating the change in oxidation and reduction potential upon the addition of the thiophene azomethine moiety. Measurements were recorded in acetonitrile solution containing 0.1 M $N(Bu)_4PF_6$ as supporting electrolyte at a scan rate of 100 mV/s.

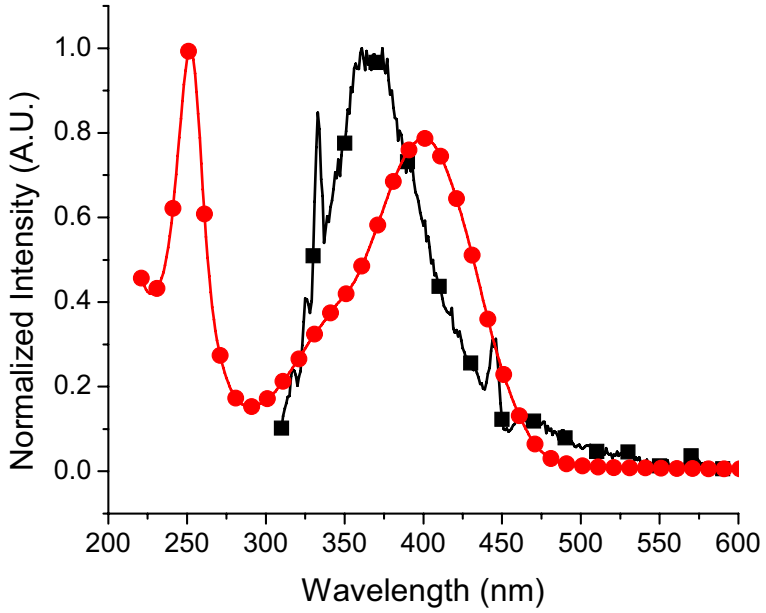

Figure B-13. Normalized absorbance (●) and emission spectra (■) of $\mathbf{L_5}$ as measured in deaerated acetonitrile.

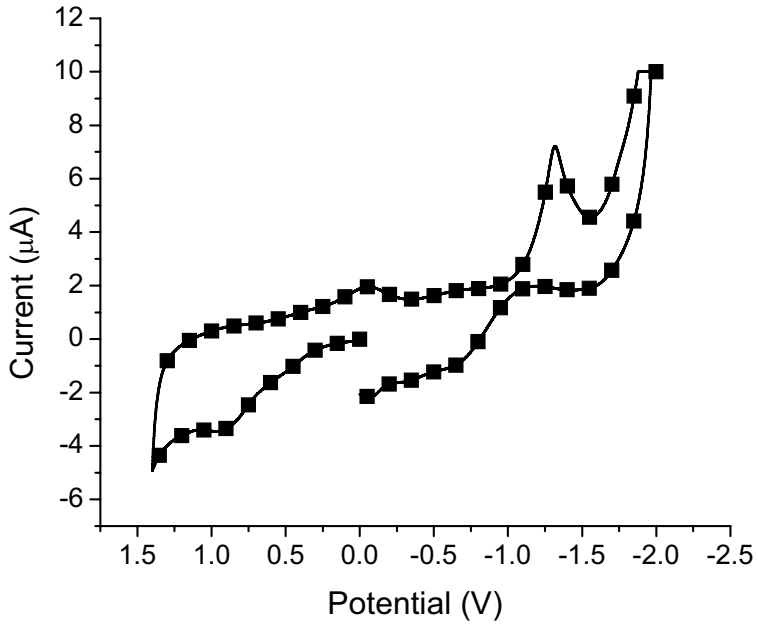

Figure B-14. Cyclic voltammogram of $\mathbf{L_5}$ in deaereated acetonitrile solution of 0.1 M of TBA-PF_6 using Ag/AgCl as reference and Pt as working electrodes.

Appendix C

Chapter 3: Unsuccessful Syntheses

Supporting Information

Table of Figures

Figure C-1. ^{1}H NMR spectrum of **B1** in deuterated chloroform. XXXIV
Figure C-2. ^{1}H NMR spectrum of **B2** in deuterated acetone. XXXIV
Figure C-3. ^{1}H NMR spectrum of the purified reaction mixture of the synthesis of **3-1** via bromination of pinacolone by **B2**.....XXXV
Figure C-4. ^{1}H NMR spectrum of the purified reaction mixture of the bromination of pinacolone with brominating agent **B3**. XXXV
Figure C-5. ^{1}H NMR spectrum of **3-2** in deuterated acetone. XXXVI
Figure C-6. ^{1}H NMR spectrum of the reaction mixture for the synthesis of **3-3** starting from the diketosulfide, **3-2**, using zinc powder and titanium (IV) chloride.. XXXVI
Figure C-7. ^{1}H NMR spectrum of the reaction mixture for the synthesis of **3-3** by the Grignard method utilizing *tert*-butylchloride as the Grignard reagent. The spectrum, recorded in deuterated acetone, shows the presence of the starting materials.....XXXVII
Figure C-8. ^{1}H NMR spectrum of **3-4** in deuterated acetone. XXXVII
Figure C-9. ^{1}H NMR spectrum of **3-5** in deuterated methanol.....XXXVIII
Figure C-10. ^{1}H NMR spectrum of the reaction mixture in the synthesis of **3-6** using the non-oxidative Grignard reaction, as recorded in deuterated chloroform. XXXVIII
Figure C-11. ^{1}H NMR spectrum of the reaction mixture in the synthesis of **3-6** using the oxidative Grignard reaction, as recorded in deuterated methanol. XXXIX

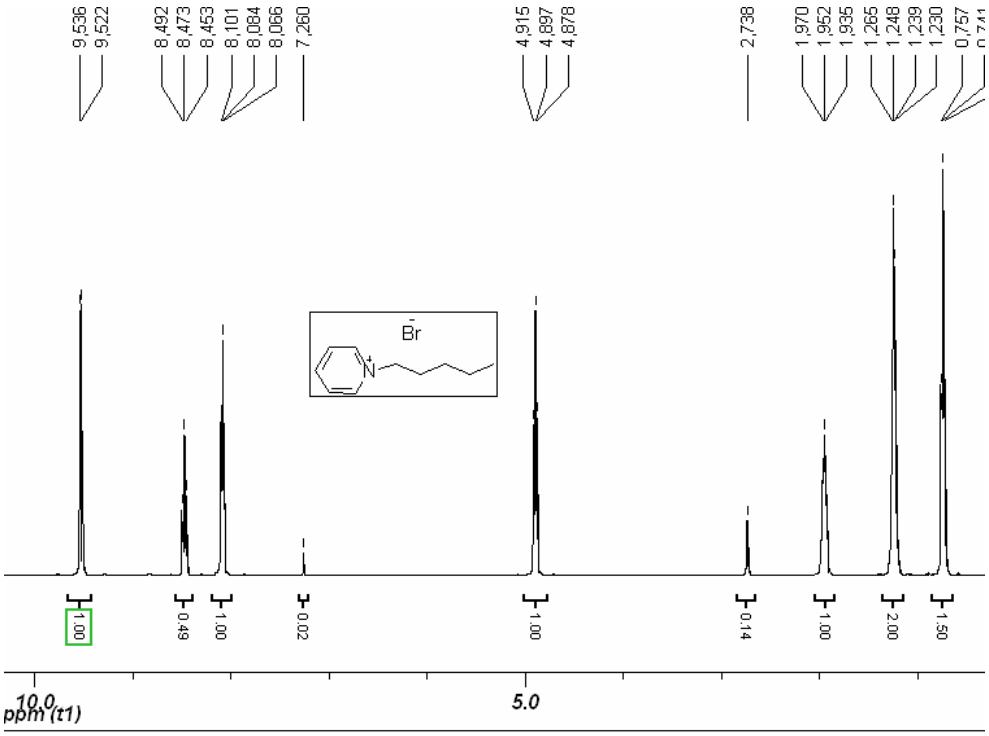

Figure C-1. ^{1}H NMR spectrum of **B1** in deuterated chloroform.

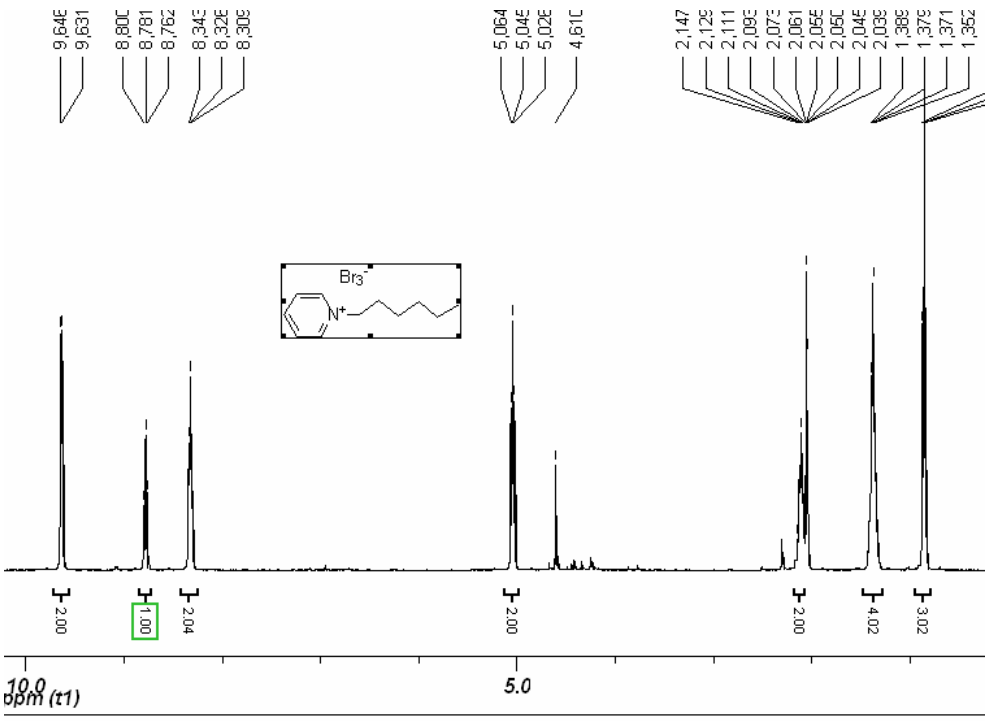

Figure C-2. ^{1}H NMR spectrum of **B2** in deuterated acetone.

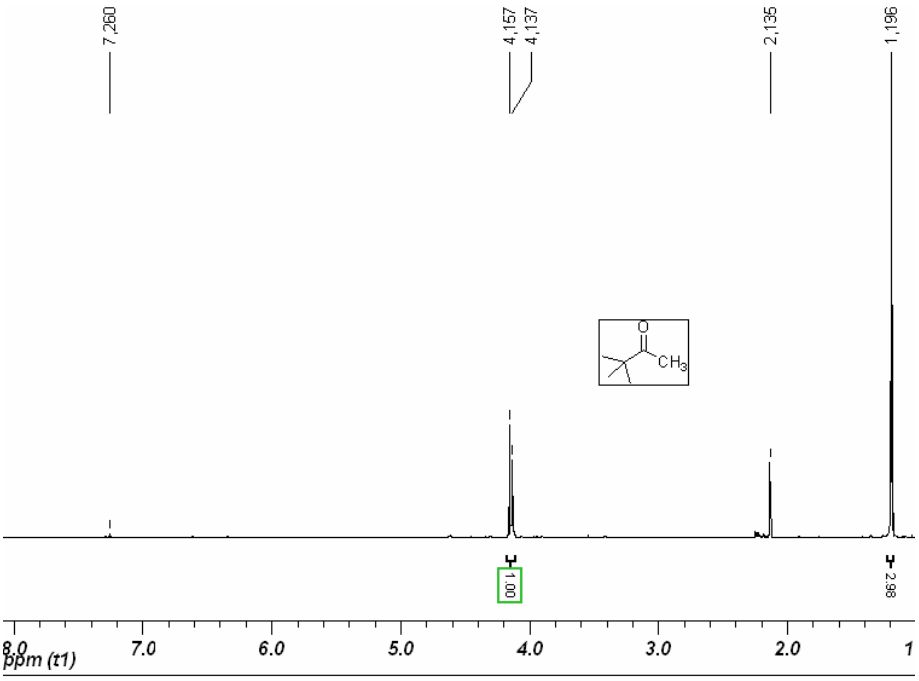

Figure C-3. ^{1}H NMR spectrum of the purified reaction mixture of the synthesis of **3-1** via bromination of pinacolone by **B2**.

The pure product observed is the starting material pinacolone. Spectrum recorded in deuterated chloroform.

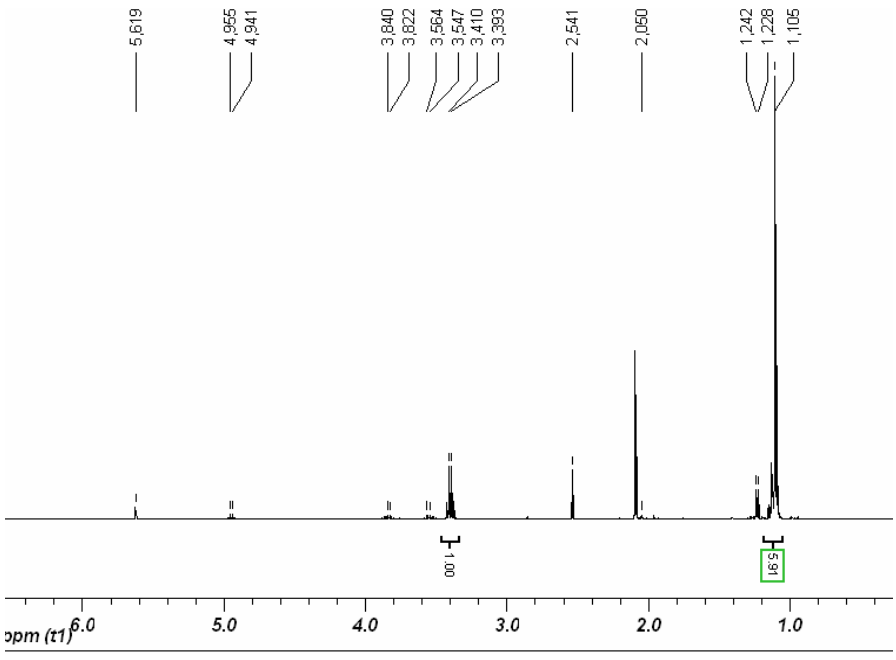

Figure C-4. ^{1}H NMR spectrum of the purified reaction mixture of the bromination of pinacolone with brominating agent **B3**.

The spectrum does not indicate the presence of the desired product, **3-1**, nor the starting material pinacolone. Recorded in deuterated acetone.

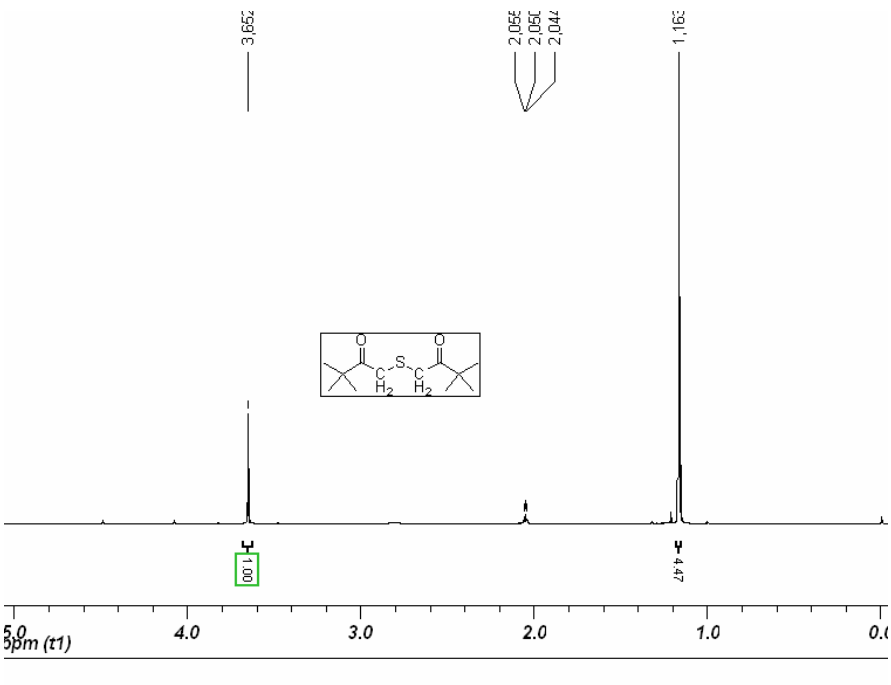

Figure C-5. [1]H NMR spectrum of **3-2** in deuterated acetone.

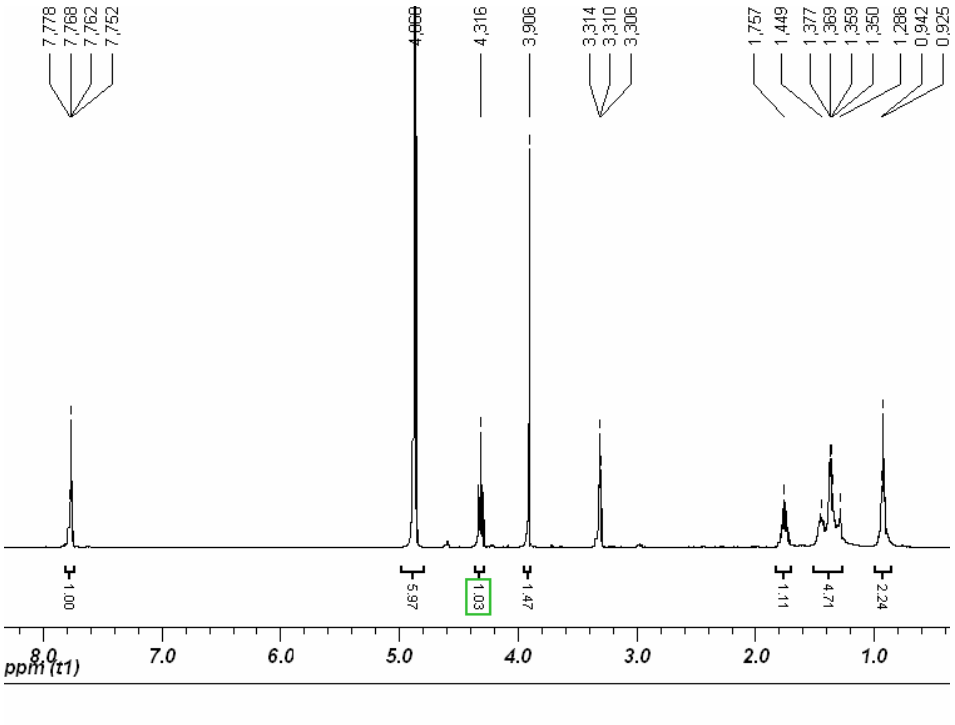

Figure C-6. [1]H NMR spectrum of the reaction mixture for the synthesis of **3-3** starting from the diketosulfide, **3-2**, using zinc powder and titanium (IV) chloride. The spectrum, recorded in deuterated methanol, does not show the presence of the desired product. The aromatic peak is a quartet which does not correspond with the desired product.

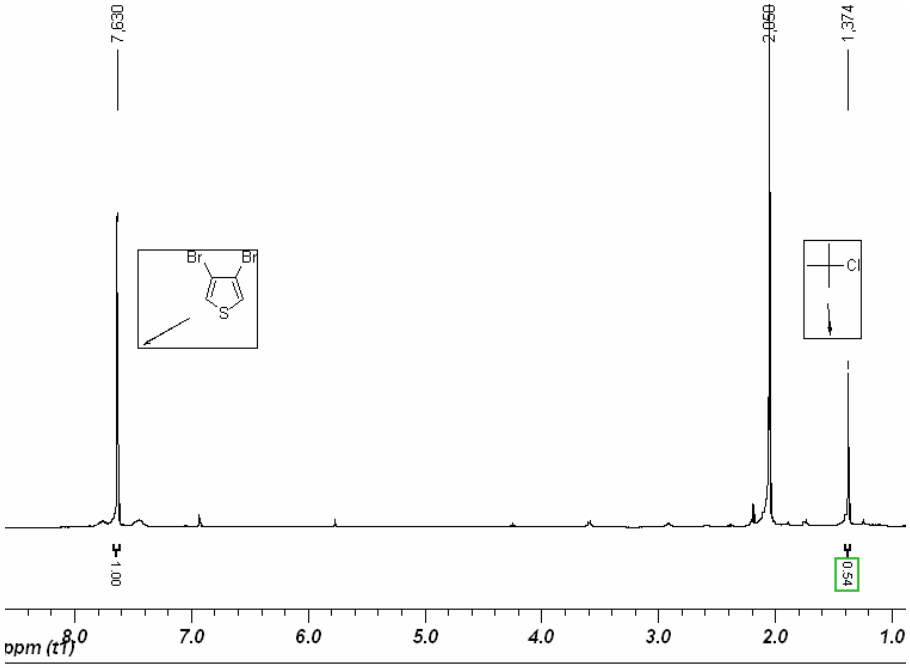

Figure C-7. [1]H NMR spectrum of the reaction mixture for the synthesis of **3-3** by the Grignard method utilizing *tert*-butylchloride as the Grignard reagent. The spectrum, recorded in deuterated acetone, shows the presence of the starting materials.

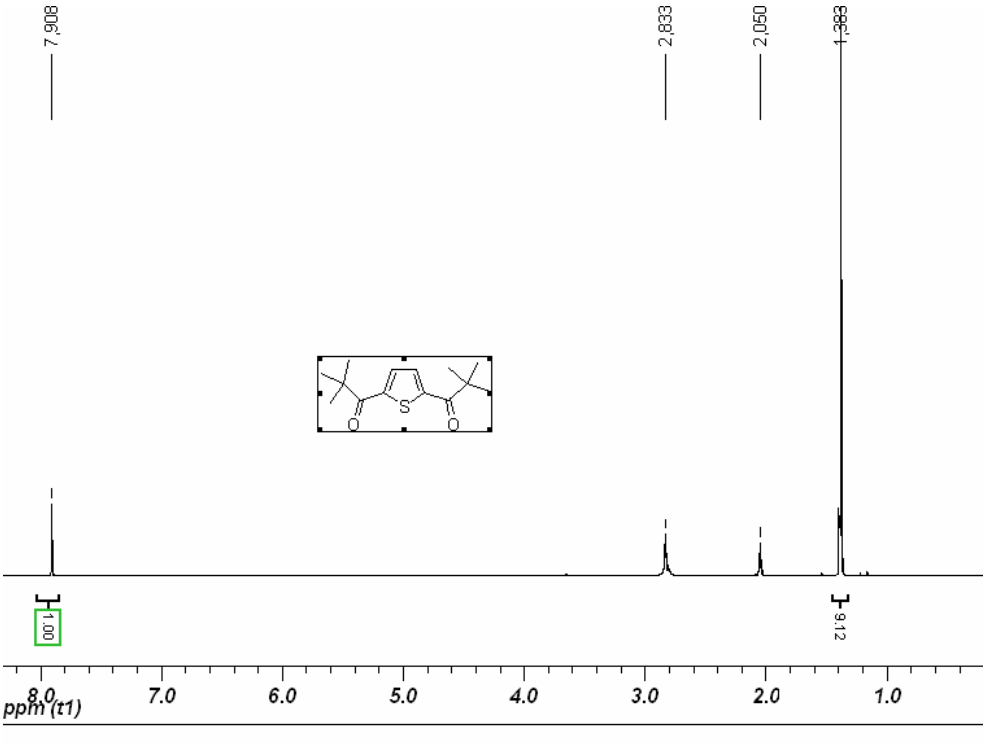

Figure C-8. [1]H NMR spectrum of **3-4** in deuterated acetone.

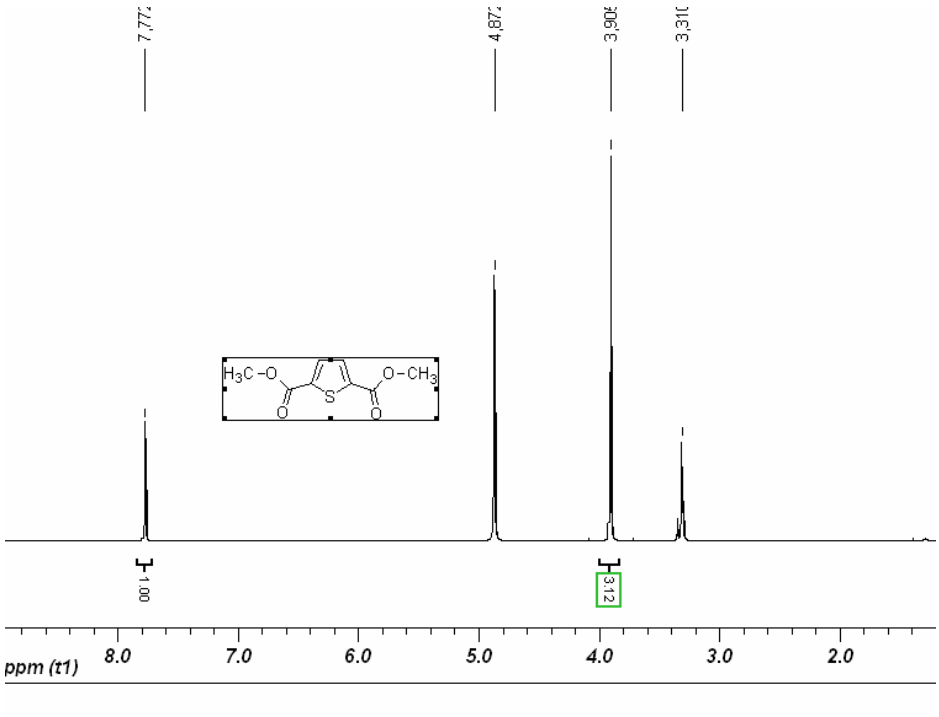

Figure C-9. [1]H NMR spectrum of **3-5** in deuterated methanol.

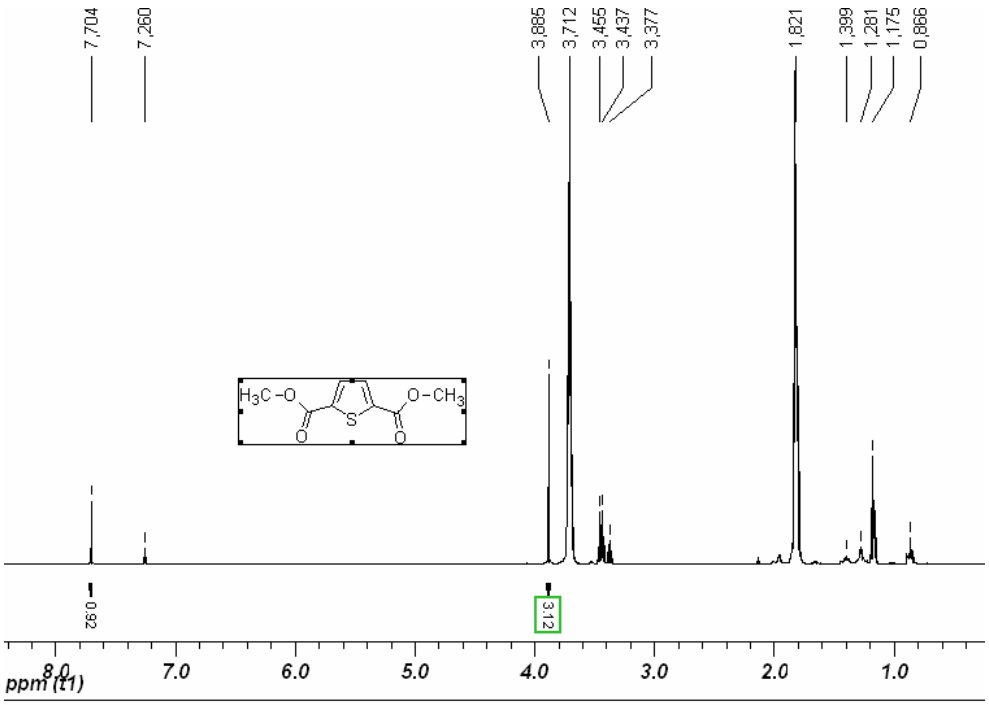

Figure C-10. [1]H NMR spectrum of the reaction mixture in the synthesis of **3-6** using the non-oxidative Grignard reaction, as recorded in deuterated chloroform. The only aromatic peak in the spectrum corresponds with the starting material, **3-5**.

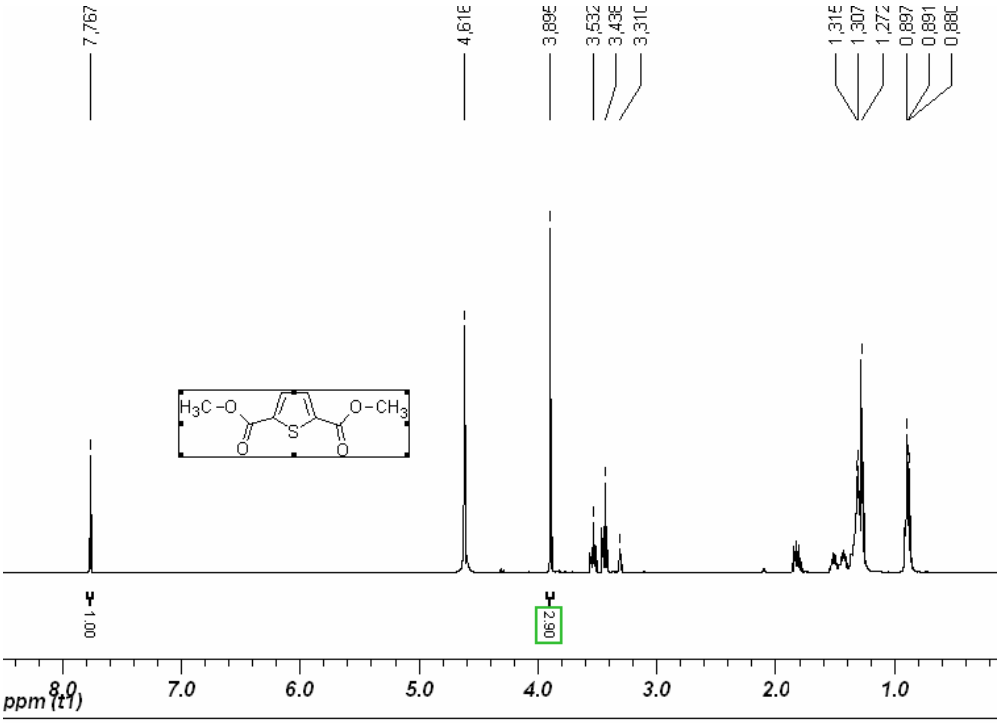

Figure C-11. [1]H NMR spectrum of the reaction mixture in the synthesis of **3-6** using the ox Grignard reaction, as recorded in deuterated methanol. The only aromatic peak in the spec corresponds with the starting material, **3-5**.